UC Berkeley
UC Berkeley Electronic Theses and Dissertations

Title
Director Based Finite Element Modeling of Rapidly Deforming Open-Celled Foams

Permalink
https://escholarship.org/uc/item/9fp246dg

Author
KURY, MATTHEW Wilson

Publication Date
2017

Peer reviewed|Thesis/dissertation

eScholarship.org Powered by the California Digital Library
University of California

Director Based Finite Element Modeling of Rapidly Deforming Open-Celled Foams

by

Matthew Wilson Kury

A dissertation submitted in partial satisfaction of the

requirements for the degree of

Doctor of Philosophy

in

Engineering - Mechanical Engineering

and the Designated Emphasis

in

Computational and Data Science and Engineering

in the

Graduate Division

of the

University of California, Berkeley

Committee in charge:

Professor Tarek Zohdi, Chair
Professor George Johnson
Professor Per-Olof Persson

Summer 2017

Director Based Finite Element Modeling of Rapidly Deforming Open-Celled Foams

Copyright 2017
by
Matthew Wilson Kury

Abstract

Director Based Finite Element Modeling of Rapidly Deforming Open-Celled Foams

by

Matthew Wilson Kury

Doctor of Philosophy in Engineering - Mechanical Engineering

with Designated Emphasis in Computational and Data Science and Engineering

University of California, Berkeley

Professor Tarek Zohdi, Chair

Traumatic brain injury (TBI) has become an serious concern for athletes and soldiers. Helmets used for preventing injury in athletics can borrow information gathered from automobile safety studies. In contrast, TBI threats for soldiers exist at different scales than studied in those works, thus requiring specialized studies to address these threats. Combat helmets consist of a stiff composite shell and a foam liner system. The liners serve to mitigate injuries caused by the impact of the shell upon the head. The aim of this work is to develop a numerical simulation that is capable of recreating the micro-mechanical behavior of the foam liners at deformation rates anticipated in a combat environment.

In this work a three dimensional nonlinear beam network model and foam geometry creation tool were developed to recreate the microstructure of open-celled foam pads. The model is designed to be stable under high rates of compression and to be able to undergo self-contact to recreate a stiffening response seen at large strains. The beam network model was used to perform rapid compression tests at various impact speeds. Shock wave speeds were calculated for each test. The sock speed data was mapped back to macro-scale parameters using the rigid-perfectly-plastic-locking (RPPL) model of cellular deformation. The model's prediction of the locking strain aligns with data studied at the macro-scale.

The work aims to demonstrate a tool that can be used to improve the protection provided foam liners at impact speeds that could be seen in combat.

To Claire Bianchi

You're awesome, it is that simple.

Contents

List of Figures

List of Tables

Acknowledgments

I would like to thank Prof. Tarek Zohdi for his years of mentorship and patience. Prof. Zohdi's mentorship when I was an undergraduate set me up for my graduate student career. He provided a work environment that allowed me and my fellow members of CMMRL to explore our engineering interests.

I would like to thank my committee members Prof. George Johnson and Prof. Per-Olof Persson for their advice and guidance. I would also like to thank Prof. Lisa Pruitt for all of her mentorship and help over my entire time at U.C. Berkeley.

I want to give special mention to past and present lab mates in CMMRL. I have learned as much if not more from you all than I have in the classes I have taken. The environment you all helped foster helped me get though the tough times in graduate school.

This work was supported by funding from the Army High Performance Computing Research Center and Army Research Lab.

Chapter 1

Introduction

This work will investigate the microstructure of foam liners used in ballistic helmets, with the methods of this work being applied to help improve the liners ability to lessen the damage done to the wearer as a result of the force transfer to the head. The work done in this investigation is the generation of a computational model capable of capturing the appropriate physics of the internal structure of the foams undergoing rapid deformation. The theory behind the model will be discussed as well as how this model may be able to be applied to help in improving the liners within ballistic helmets.

1.1 Motivation

In a wide range of applications, helmets serve as the primary protection against head injury. Helmets are present in sports, military, construction and other applications. Helmets range in design depending upon the needs of the wearer, however most helmets contain several similar features.

Of particular interest is the design of military ballistic helmets. In the history of ballistic helmets, the primary goal was in the deflection and mitigation of shrapnel, bullets and other types of projectiles. However, in more recent military conflicts bombs have become of greater threat to current military personnel[47]. During this time as well, traumatic brain injury(TBI) has become an increasing issue among injured soldiers.

Since World War Two, explosions have been the primary source of wounds to American soldiers. Explosions contain multiple means of injuring a person, as well as the tendency to cause multiple injuries to the same person[17]. With such threats to the warfighter, the likelihood of incurring a head injury is high. With helmets providing the primary means for head injury prevention it motivates one to investigate in what ways the helmet may be improved.

Two main systems provide means of mitigating impact damage to the wearer, the outer shell and the lining foam pads. Computational models used to predict the protective capabilities of a helmet require part scale models of the shell and liner. These models use

parameters obtained from average responses of the materials at the sub-scales. By changing the material properties and/or arrangements at the small scales, a different part scale response would be expected. With this in mind, this work aims to present a framework that can be used to simulate the details of the foam micro-structure that can respond to large deformations and high strain rates. This framework will then be used to inform parameters for part scale models. In the remainder of the chapter a brief overview of helmets will be covered followed by an overview of the mechanics of foams and then concluding with a discussion of mechanics of rapid deformation of materials.

1.2 Helmet Overview

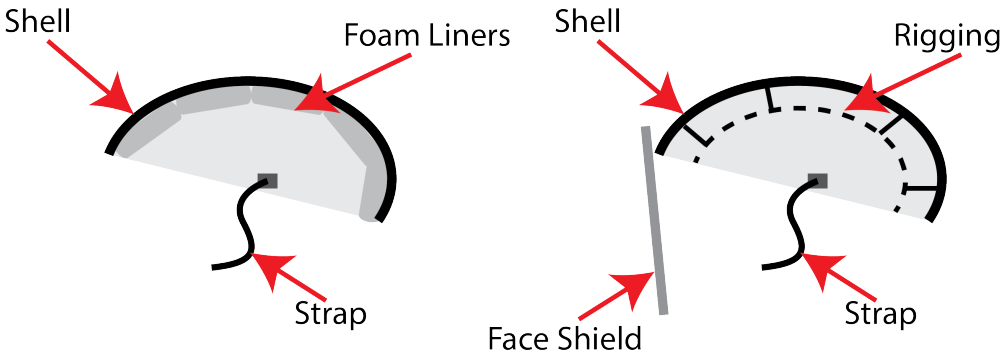

Figure 1.1: An Illustration of two common helmet arrangements. Both arrangements have a protective shell for initial blunting of impactors and prevention of penetration of objects into the head, and a strap to maintain the helmet in the correct position on the head. (Left) The helmet uses foam liners for additional impact mitigation. (Right) Helmet uses rigging to separate the wearer's head from the shell in order to provide distance from the impact event and the head. In addition a face shield is present to provide additional protection to the wearer's face.

As depicted it figure 1.1. A helmet consists of four common features; a hard exterior shell, an internal absorption liner, a chin strap, and a possible face guard. The face guard is present in some helmets because it provides the wearer's face protection from incoming projectiles. The guard can also be functionalized to provide sun protection, or to act as a heads up display(HUD) for communicating information to the wearer. The chinstrap serves a means to keep the helmet in place during the use of the helmet, allowing for the helmet to remain on the head during the normal course of actions taken by the wearer, and then to remain on the head in an effective orientation during an impact thus improving the protective capabilities of the helmet.

The outer shell and the internal liner serve as the means of impact mitigation. The deflection, plastic deformation, and/or delamination of these regions absorbs energy from the impact, and reduces the energy transfer to the brain.

Of particular interest is the design of military ballistic helmets. In the history of ballistic helmets, the primary goal was in the protection from shrapnel, bullets and other types of projectiles. However, in more recent military conflicts bombs have become of greater threat to current military personnel [47]. During this time as well, traumatic brain injury(TBI) has become an increasing issue among injured soldiers.

Ballistic Helmets and Traumatic Brain Injury

The modern form of ballistic helmets comes from the helmets worn by the French during World War One. The design of these helmets consisted of a one size fits all metal shell that is fitted to the wearer's head by internal straps. These designs would remain prevalent until the 1960's, where the metal shell would be replaced with a Kevlar composite. The modern ballistic helmet, the Advanced Combat Helmet (ACH) was introduced in the 2000's to the U.S. army. It improved upon the previous designs by reducing weight of the helmet and replacing the internal strap system with foam liners [47].

The main objective for the helmet is to protect the wearer from shrapnel and other projectiles. To measure its effectiveness the helmet is rated against several types of projectiles to discover what impact velocity the helmet is penetrated fifty precent of the time. These velocities are referred to as the ballistic limits of the helmets.

With the primary design goal of the ACH being to prevent penetration of projectiles, a new concern arises known as Behind Armor Blunt Trauma (BABT). These types of injuries are the non-penetrating injuries resulting from the deformation from the protecting armor [14]. In helmets, the BABT results from the shell's deformation. These injuries are thought to be caused by the motion of the protective equipment, and the pressure waves passed to the internal organs. For head injuries, concussions and other longterm neurological damage can occur. Even when the helmet is operating below its ballistic limit, it is still possible for BABT TBI to occur.

TBI occurs when a persons head is subject to an impact or rapid acceleration, often associated with a rotation about the neck (being rear ended in car is an example of this). These events induce mechanical waves that pass though the brain, and in cases where the event is severe enough to cause a concussion, the impact of the brain against the skull. Damage from the event can manifest in several forms. In more severe TBIs bruising, bleeding and swelling of the brain matter can occur, and can be fatal. These types of injuries are often easy to diagnose because of outward physical symptoms, and from medical imaging.

In milder incidents of TBI, it can be harder to detect the damage done. In mild TBI (mTBI) the damage often does not manifest in focused regions within the brain, instead the damage is generally scattered though out the brain. In mTBI the injuries are believed to be due to the perturbations of the neurons within the brain, leading to disruption of neural pathways, swelling of the neurons and potentially death of individual neurons. It is currently

believed that the cause of the neuron damage is due to the shearing and tensile stress waves that propagate though the brain during an incident. The stresses exerted upon the cells induces reactions from the cells themselves lead to the reduction in of the neuron's ability to send signals through the axon. This disruption is referred to as diffuse axonal injury. [56, 4, 58]

In terms of assessing what actually imparts damage in the brain during a non-penetrating impact event, is still the subject of debate, with most of the research centered around the types of impacts that would occur in athletics and during motor vehicle accidents. As detailed later, the athletic and vehicle accident studies focus on impacts of moving people against other people or objects. These impacts take place over a period of milliseconds, with speeds in the tens of meters per second. Thus, when dealing with impacts from blasts and ballistic projectiles the mechanics of injury incursion are not necessarily applicable from these studies [17].

TBI has been linked to a variety of cognitive issues, including headaches, confusion, amnesia, difficulty concentrating, anxiety, hyperarousal,and difficulty sleeping amongst other things [90, 14, 56]. Improvements in helmet protection for warfighters and civilians should aim to maintain their current levels of protection and improve the helmets capabilities for mitigating TBI. In this mission it is the objective to reduce the loadings and the loading rates the brain is subjected to [5].

Helmet Design Considerations

Impact Events

In the past few decades research in helmets has increased, with a large part of these studies focused on the helmets for american football players [17]. However these studies are not always applicable to improving the design of ballistic helmets. The impact types that athletes undergo are not necessarily applicable to that of a warfighter. Thus it is necessary to investigate helmets in situations that are applicable for the warfighter in order to make meaningful design choices.

Investigating helmet performance needs to be done in manners applicable to a combat theater. As per [17], there are three event-based sources of head injury it is necessary to consider:

1. Blunt impact
2. Ballistic impact
3. Blast Impact

Blunt impacts are the types of impacts most civilian helmets are designed to prevent injury against. These are injuries that occur from falls, vehicle crashes, falling objects, bicycle accidents and the like. For military personnel additional sources of blunt impacts include collisions due to parachute drops, impacts with the interior of accelerating vehicles,

and accelerations of the body due to explosions [17]. The impact velocity in these types of events is around $5m/s$ to $15m/s$, the time from the start of the impact to the moment of peak loading is on the order of 10 milliseconds. While there are still many unknowns regarding how blunt impacts induce damage to the brain, studies from automobile crash studies can be applied as guidelines and metrics for assessing the ability for a helmet to protect the wearer. The leading metric for measuring the severity of an impact in vehicles is the Head Injury Criterion (HIC) [40]. The HIC attempts to make a scalar metric for both the level and duration of the impact event. The HIC is defined as follows:

$$HIC = \left\{ \left[\frac{1}{t_2 - t_1} \int_{t_1}^{t_2} a(t)dt \right]^{2.5} (t_2 - t_1) \right\}_{max} \tag{1.1}$$

In the above t_2 and t_1 are the end and beginning times for and interval of the impact event, $a(t)$ is the instantaneous acceleration of the body measured in units of gravitational acceleration("$g's$"), thus giving a HIC score units of $gseconds$. The interval $(t_2 - t_1)$ according to guidelines should not exceed $15ms$. It is intended that the HIC be the largest measure of all the intervals within the impact event, not exceeding $15ms$. In practice, this typically means that the HIC will record some of the acceleration behavior prior and post the peak acceleration, but without other information away from the peak acceleration. There are criticisms of the HIC, including that it does not take rotational effects into account and there is no accountability for local changes in the head during impact [17] [81].However, because of its longevity as a metric, there is some correlation with it and likelihoods of injury, see table 1.1 for an approximation to the scale of HIC.

Injury at 50% likelihood	HIC $(g \cdot s)$
1:Minor	200
2:Moderate	500
3:Serious	900
4:Severe	1300
5:Critical	1700
6:Maximum	2200

Table 1.1: Summary of HIC and level injury at that approximate HIC score, as measured by the abbreviated injury score [54]. Ratings of a 6 are classified as fatal, and scores of 5 are like penetrating head injuries, with scores of 2 being an internal skull fracture[16].

While HIC may be sufficient for athletic helmets, and can help in the analysis for some blunt impact incidents, it is not applicable to the other two types of events which ballistic helmets need to be rated against, ballistic and blast events. These events, unlike blunt events, are much shorter in time scale, typically on the order of 200 μs and $10\mu s$, respectively. Ballistic impacts involve the collision with small projectiles that themselves will deform significantly in the impact event, while in a blast impact, the helmet is subject to a pressure

shockwave. With these events being so dissimilar to that of an auto accident the HIC can not be reliably applied.

Ballistic impactors come from two main sources, bullets from from guns, and fragments from explosive devices such as artillery shells and improvised explosive devices(IED). For bullets, velocities typically range from $350_{m/s}$ to $1000_{m/s}$ for small caliber hand guns to rifles, with masses of about 10 grams. However, for the fragments from an explosion, the velocities and masses are not well characterized [17]. There are currently no standardized tests for helmets to deal with fragments from IEDs. In ballistic incidents, there is a distinct locality of the impact. The area of initial contact is much smaller than that of the blunt impacts or event the blast impacts.

With the lack of HIC, as a valid measure of damage due to an incident for ballistic impact events, other forms of measurement are necessary to approximate the amount of protection provided by the helmet. Simulations of helmets undergoing ballistic impacts, and measurements of forces on the skull provide a means of evaluating protection provided [68, 45, 50]. According to DoD test protocols, experimental metrics for assessing protection are the ballistic velocity limit and the amount of back face deformation (BFD)[17].

Ballistic limit serves as a measure of the helmet's capability of preventing projectiles from penetrating the helmet and by proxy the head of its wearer, where higher ballistic limits for a a given mass of impactor indicate a higher level of protection.

BFD arises because one of the main energy absorbing mechanisms of the helmet is the deformation of its shell, this deformation can impact the head itself, causing injury. BFD attempts to measure the risks of these deformations. BFD is measured by using a clay simulacra of an adult head, where the helmet is placed on top if it and then the helmet is shot with the appropriate projectile. After the event, the helmet is removed, and if the helmet prevented the penetration of the projectile into the clay, the deformation of the clay is recorded and the largest surface displacement is then labeled as the BFD. More studies need to be done in order to determine if BFD is the most appropriate measurement to do with this type of test, where volume of deformation and area of deformation may also pay roles in determining the risk factors of brain injury.

In a blast loading event, waves of pressure and heat impact the helmet and head of a person caught near the blast. While the nuanced details regarding the damage from the blast is an open research topic. It is known that peak overpressure, pressure above atmospheric pressure, carries with it characteristic damage trends exists as seen in table 1.2. Less is known about how to measure the effectiveness of helmets in mitigating the shockwaves. Computer simulations have been employed to explore various helmet configurations and there effectiveness at mitigating blast loading. Like in the ballistic impact studies, direct measurements from the simulation are used as guides to assessing helmet performance. Rodriguez and Millan [70] demonstrated that helmets with face shields and additional mandible guards were able to reduce the peak pressures in the brain by a factor of five. Several studies, such as [89, 38, 88], have shown that the arrangement of the helmet and the effect of the propagation of the blast wave around and through the helmet can lead to an increase of pressure between the helmet and the skull, this increase is known as the underwash effect[38]. Use of face

shields and more area coverage by pads have been shown to reduce the underwash's loading effects [89, 70].

Blast Overpressure (psi)	Physiological Effect
.2	Minor Ear Damage
1.	Knock a Person Over
5.	Eardrum Damage
15.	Lung Damage
35.	Fatalities Possible
65	Fatality Almost Certain

Table 1.2: Characteristic injuries from blast events without protection.[11].

Mechanics of Ballistic Helmets

In the course of an impact event, the helmet will disperse the stresses over a larger area of the head, absorb energy in the impact and to dampen the peak loadings. How the head is loaded is determined by the behaviors of the composite shell, the foam liners, the arrangement of the liners within the helmet. What follows is a description of the mechanisms that govern the general response of the shell and liners.

The Composite Shell The outside shell of the ACH is made from shaping layered sheets of Kevlar 129 fibers within a thermoset matrix material [47]. To absorb energy from the impactor, the composite undergoes a variety changes as summarized in table 1.3 and figure 1.2. With the fibers serving as the main means of energy absorption and the matrix serving to assist in recruitment of additional fibers and prevent separation of yarns.

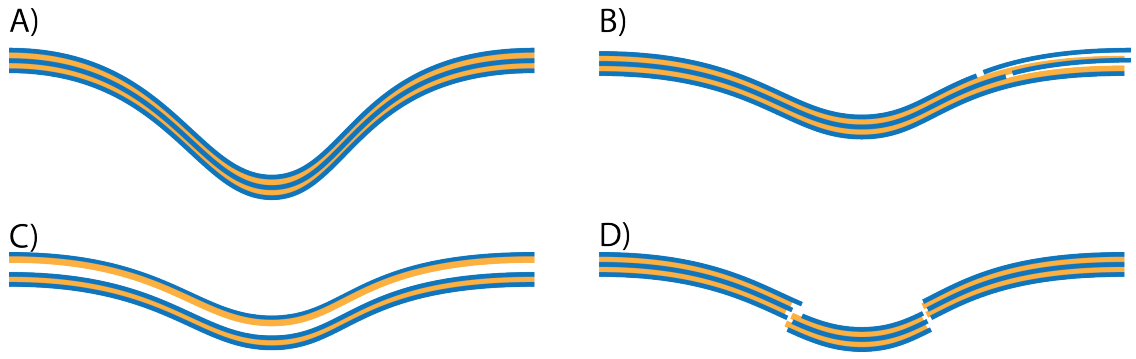

Figure 1.2: Different mechanisms of energy absorption within the composite layer of a fiber composite. A) Cone Formation B) Tensile Failure C) Delamination D) Shear Plugging

Mechanism	Details
Cone Formation	In a perpendicular impact with a composite, some of the fibers will be directly under the impactor. These fibers are referred to as primary fibers. In the impact the primary fibers will be the primary deformed strands, and will form a triangular deformation pattern. Here energy is stored in the elastic and plastic deformation of the strands and the local matrix material.
Stretching of Secondary Yarns	As the primary fibers deform, they will recruit the fibers that they are interwoven with. This fiber recruitment causes these indirect fibers to stretch and store some of the energy elastically.
Tensile Failure of Primary Yarns	The large deformation, and high loads experienced by the primary fibers can cause the fibers to fracture or experience pull out from the matrix material around them. The efforts of fracturing the yarns and/or separating it from its surrounding material causes a permanent loss of kinetic energy from the system.
Delamination	The Composite shell is comprised of several layers of Kevlar sheets. The sheets are bound together to act as one solid, however this layering induces weaknesses between the sheets, and as the composite is impacted, the layers may separate, cracking the matrix material and extracting kinetic energy from the system permanently.
Matrix Cracking	Associated with the act of delamination, the loadings on the matrix cause the formation for cracks which can propagate, creating new surfaces.
Shear Plugging	High levels of shear stress near the impactor cause though thickness fracturing of the composite. The breaking of fibers and matrix material removes energy from the impactor.

Table 1.3: Key energy absorption mechanisms present within a composite undergoing impact. [47, 61, 30]

Foam Liners The lining structure of the helmet is the second form of the helmet's damage mitigation. Prior to the 2000's a rigging, similar to what is found in construction helmets, was used to fit the helmet shell to the warfighter's head. This form of lining was discontinued for using foam pad liners[47]. Foam liners within the helmet serve in a protective role as well as a method to adapt the shell of the helmet to fit the different sized heads of its wearers. The foam liners used in the ACH are manufactured by Team Wendy, referred to as Zorbium Action Pads (ZAPs). The pads consist of two foam sheets covered in an air tight thin plastic shell, and then surrounded with a fabric cover. The outer sheet of foam is stiffer than that of the layer closer to the head, the comfort layer[60]. While it may just be that the choice for Team Wendy to use the term comfort layer for the softer layer is solely marketing, it is noted in [47] that for adoption of any equipment to be successful comfort is an important

factor, for if the warfighter does not wear the equipment, no matter how good it is they will not be protected.

Figure 1.3: Left: Image of a set of Zorbium Action Pads (ZAPs) produced by Team Wendy. Right: ZAPs installed into a ballistic helmet[96].

In their protective role foams serve two major purposes: by compressing they lower the impact forces on the skull and absorb energy, and they provide resistance and dampening against the deformation of the shell layer in order to prevent direct contact of the shell with the head [50].

The ZAPs use a polyurethane based foam, so the deformation of the foam itself is a viscoelastic deformation. The deformation itself will store energy from the impact and then release the energy at a later time. A characteristic loading and unloading curve is shown in figure 1.4.

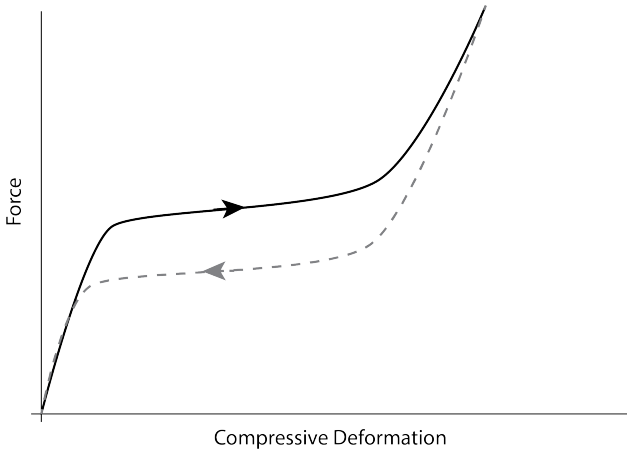

Figure 1.4: Cartoon of the force exerted by the foam as a function of its level of compressive deformation. The black solid curve is the path followed in the loading of the foam, while the grey dashed curve is the unloading behavior of the foam. The area between the two curves represents the energy lost in the loading and unloading process.

When subjected to forces, foams absorb most of their energy in a flat plateau region. This allows for a large amount of energy to be stored in the foam at a lower applied force than if the material had been fully linear or monotonically stiffening. In a dynamic loading event, a foam will change the shape of the instantaneous load applied to the head such that the impulse occurs over a longer time at a lower magnitude. In addition the viscoelastic nature of the foams cause the unloading loads to be less than the applied loads, thus reducing the forces on the head in the unloading of the foam[50, 43]. Typical amounts of energy lost in the loading-unloading cycle is on the order of one percent for polymeric foams around room temperature [48].

The effectiveness of a foam can be measured design selection for a foam liner is to plot the total work done in loading against the peak stress. In there plots they are characterized in having two distinct regions, see figure 1.5. Early in the curve the average slope is steep, the gains in energy storage are great as the peak loading increases. Then at a specific point the curve elbows to have a very shallow slope, thus there are poorer gains in energy storage as the peak loading increases. If the peak loading is known for given impact, one can select an ideal foam for a purpose in terms of energy storage by having the elbow be at the peak loading level. If the loading is less than the transition level then there will be more energy passed on that could have been absorbed, while if the peak loading is greater than the transition point the energy absorption is less efficient [28].

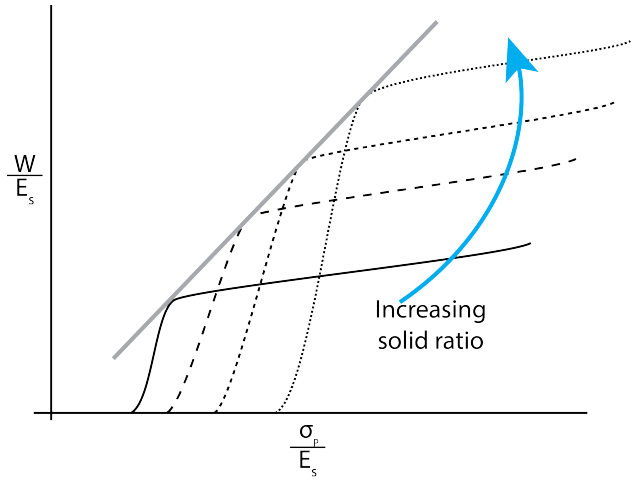

Figure 1.5: Illustration of the energy absorbed by an elastic foam compared to the peak stress within the foam, normalized by the the sold elastic modulus for the material. In these plots there is a elbow where there is a noticeable reduction in the rate of energy absorption of the material. Solid ratio of the foam increased the curve translates to the left and stretches upward, the line formed by connecting all of the elbows of these curves allows for the appropriate solid ratio when designing for a specific peak loading[28] .

In the curves illustrated above (1.4, 1.5) all measurements are done at a specific loading rate. If the material is polymeric in nature then changes in loading rate will lead to different stiffness responses of the base material, potentially moving the curves. With a rate dependence on the mechanical responses, complications arise when attempting to design a protective device that may undergo different rates of loading.(At higher rates of loading the mode of deformation resistance changes see section 5.1 for an exploration of this topic.) In addition to these complications, an addition wrinkle is thrown in for combat helmets because of the need to prevent the collision of the helmet shell with the head, if the velocity of impact is great enough the local deformation in the shell will push through the foam and impact a small region on the head. This localized impact will cause high local stresses on the head, potentially leading to fractures of the skull, and other more characteristic localized injuries; bleeding, contusions, etc.

In previous studies [50, 47, 75, 18], it has been shown that the desired stiffness for a foam, all other things being equal, is that at higher velocities a stiffer foam should be used, while at lower velocities a softer foam should be used. Layering and gradating foam is used to take advantage of both behavior ranges. This means that the optimal foam type for a ballistic impact is different that that of one for protecting the head from a blunt injury. With these competing demands for performance in the foam current deign philosophy for combat helmets is to optimize them for slower bulk type impacts, such as would be experienced in an automobile collision [55].

1.3 Cellular Materials and Open Celled Foams

It is then the responsibility for the lining system of the helmet to mitigate the motion of the shell relative to he head, such that damage to the head/skull/brain is minimized or eliminated. Thus the focus of this work will be on studying the foam liners of combat helmets, with the aim of using micro-scale simulations of the foam network to inform material parameters for macro-scale models.

Description of Cellular Materials

In section 1.2 details of helmet foam liners were discussed and much of the response arises from the open-celled nature of the foam used. Open-celled foams are one of the two characteristic forms of foam, the other being a closed-celled foam. Closed-celled foams have a microstructure that looks like a collection packed balloons, and under large deformation will undergo permanent change. An open-celled foam microstructure contains rod like structures that surround voids, and do not necessarily undergo permanent change when deforming. What type of foam is formed is determined by the manufacturing processes used, as detailed below.

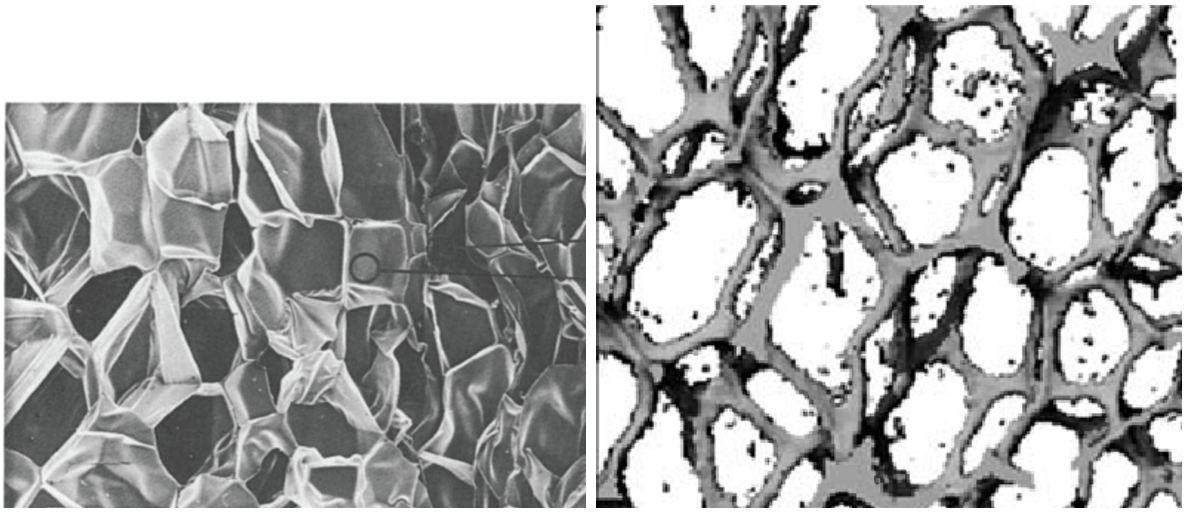

Figure 1.6: (Left) A scan of a closed-cell foam [27]. (Right) A scan of an open-cell foam [41]

Production of Foams

In the production process of both open- and closed-cell foam, a polymeric solution is either mechanically or chemically aerated, introducing bubbles into the solution. The bubbles will attempt to rearrange themselves such that they form area minimizing formations. The bubbles in the froth will be more ellipsoidal than spherical because of compression experienced during the forming process[33]. The more eccentric features will tend to be aligned and

pointed in the overall rise direction of the foam. The rise direction is the general direction the foam froth expands during its production. the features in the 'rise' direction are longer by a factor of 1.1 to 1.5 larger [28, 93]. This elongation can cause some variation of the macro scale parameters in the rise direction versus the in plane directions.

In this form the structure of the froth can be broken into three main features. The first feature is the the volume of the bubble, there is is no polymer in the volume of the bubble however there is trapped gas. The second feature is the surfaces of bubbles that are the main interfaces between bubbles. In the surfaces there is a thin layer of polymer solution. Lastly there are the edges of bubbles that are at the intersections of the different faces separating the different bubbles. In the edges, there is a larger amount of solution as compared to the faces of the bubbles. These features are illustrated in figure 1.7.

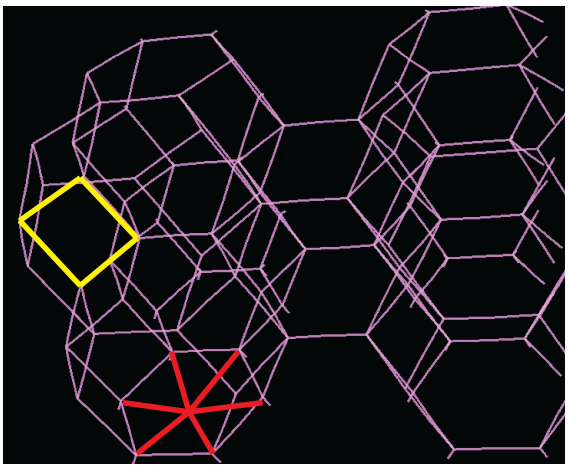

Figure 1.7: Illustration of a regular foam geometry. The geometry is comprised of a volumes separated by faces (red star region) and edges (yellow lines).

In the solidification process, depending upon the various effects of surface energies and related energetics, the polymer on the faces of the bubbles will either solidify and form solid walls, or they will collapse and the fluid in the face will recede to the edges of the structure. In the former case a closed-celled foam is formed, and the latter an open-celled foam is formed, creating the structures seen in figure 1.6.

In a closed-cell structure the faces, edges and the trapped fluid volume within each cell have a response to the deformation of the structure, and if loaded to an extreme the faces may rupture thus no longer trapping the fluid and allowing flow of the fluid from cell to cell. In the open-celled structure, the primary from of solid that remains are the edges of the cells, in some contexts these edges are referred to as ligaments. In this form the dominant structural response is driven by the ligaments. The open-celled nature of the structure allows for fluid flow though the entire structure, thus for chemical and thermal responses in the foam the sold structure and the flow of the fluid through it play significant roles. Control over the shape of the bubbles and the state of the foam can be exerted by altering the amount of

catalysts to assist in the solidification process, surfactants to assist in the mixing of material in the liquid state and by sending mechanical waves though the solidifying solution [31].

Depending on the level of control during the the production process, the bubbles will have varying distributions in their size and shape. The variation of the bubbles will cause the microstructure to be irregular, such that the structure can not be reduced completely to a unit type cell, as may be possible for other cellular structures[77]. Gibson et al. introduces unit cells in her study of general foams. In their work they use the unit cell as a simple structure to apply classical strength of materials equations in order to derive general trends. Their work predicts the elastic modulus and bucking plateau well for general foams, however a scaling parameter is necessary in order for the data to align correctly. This parameter can be thought of, in part, as a correction to their idealization of regularity.

Mechanics of Open-Celled Foams

In order to obtain the response of an open-celled foam under mechanical loading conditions it is necessary to understand how the mechanical response of the foam arises from the microstructure. Only open-celled foams will be discussed, because they are the structure of interest, however the general trends of behavior apply to closed-celled foams as well[28]. The author believes that open-celled foams were chosen over closed-celled foams because of two reasons: The first is that as closed-cell foams deform their walls my rupture, this causes the foam to become weaker over repeated uses. The flexible open-celled foams currently used do not experience this permanent softening. When a helmet is expected to potentially endure many small impacts and still provide protection the consistency of open-celled foams is an advantage. The second reason is that the foam liners serve to adapt standard shells to fit a soldiers head, the more flexible nature of open-celled foams allows them to be installed without damaging the foam more easily.

As illustrated in figure 1.8 there are three main regions of compressive behavior in a bulk open-celled foams. At small strains, there will be a nearly classic linear elastic response, in the second region there is a shallow plateau region where the the stresses remain relatively constant over a large range of strains, and then lastly at large strains there is a rapid increase in stress.

In the linear elastic region, the macro behavior arises from the the small rearrangement of the ligaments, where each ligament it self only under goes a small deformation.

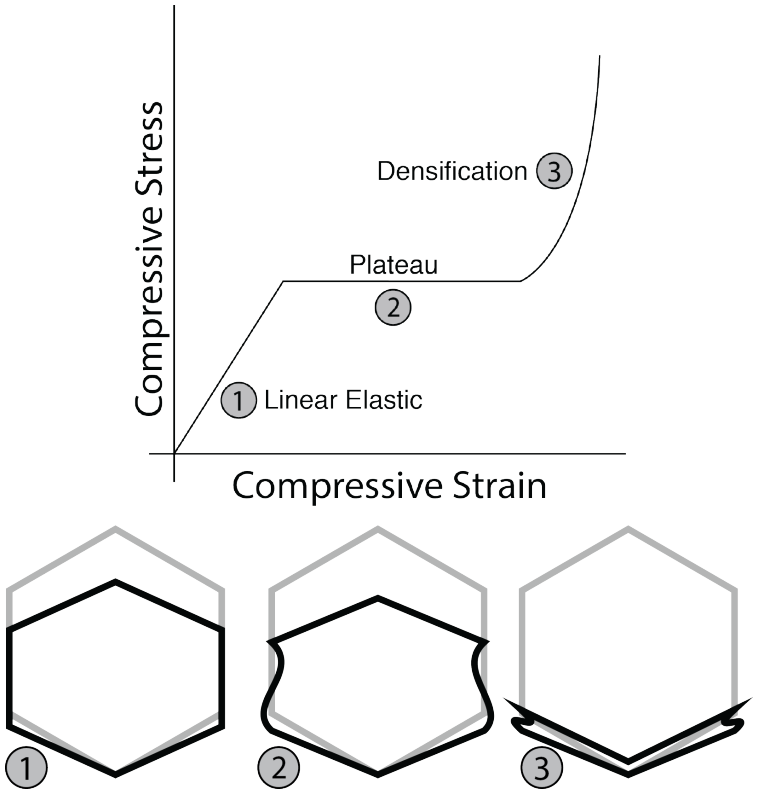

Figure 1.8: The three major load response regions illustrated with their characteristic micro-mechanical response. The shaded figure represents the stress free configuration of the unit cell, with the darkened figure representing the current configuration.

In the second, the plateau, region the material has deformed enough such that the internal loadings within the structure exceed the buckling limits of some of the ligaments. Thus, while the ligaments are in a buckled state they can only exert forces that are around their buckling loads, because of the slender nature of the ligaments themselves there is a large amount of deformation that can occur until the nature of the response changes. On the macro-scale there is a large region of nearly constant stress. In a real material, the onset of buckling does not happen uniformly though out the material. Areas of local weakness will buckle first leading to a partially collapsed region. As the deformation continues the collapsed region will grow, and other areas of weakness will begin to collapse as well, thus there may be a non-smooth transition in the buckling region [7].

In the final compressive loading region, the extent of the deformation has led to bucking to such an extent that ligaments begin to come in contact with one another. With such a degree of compression the cellular and porous character of the material declines, and becoming more of a solid material type response. Where the effect of ligament bending ad axial compression is lessened and the compression from contact between the the different ligaments dominates the stress response. As the deformation continues more and more

ligaments come into contact, thus creating more contact forces producing an increase in the stress seen in the last stage of the loading curve.

If the cellular solid were to be loaded in the tension, there are two characteristic regions of note: an initial linear elastic region similar to that seen in the compressive response and due to similar reasons, and a stiffening region past the linear region due to the alignment of ligaments (figure 1.9).

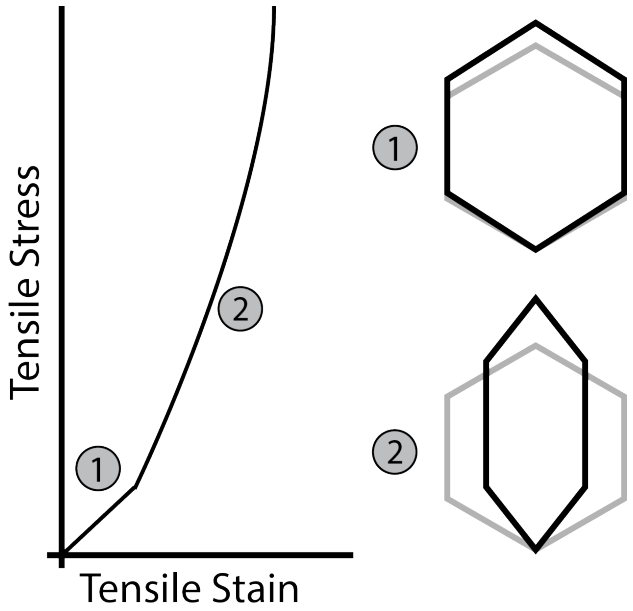

Figure 1.9: Illustration of foam's tensile load response. An initial linear elastic region is followed by a stiffening stress response due to alignment of ligaments in the microstructure.

It is worth noting that events such as plastic deformation may occur in foams and are not restricted to one of these domains. Plastic response will begin once the conditions are met on the micro-scale, thus under the right configurations of material and structure it is possible to see the effects of plastic deformation in all loading regions, and that these regions may see variations in response due to the plastic response.

The response of many open-celled polymeric foams will be primarily elastic, but with some viscous dampening as illustrated in figure 1.4.

For many part-scale applications, an understanding of how the microstructure drives the response to the material is not necessary. One is just seeking an appropriate material model and parameters are necessary. Foams on the macro-scale are modeled primarily as a hyper elastic material with a strain rate correction multiplicatively applied to them [53]. Where in equation 1.2 the potential is defines at some loading rate, and then scaled to fit the strain rate.

$$\sigma = \frac{\partial \phi(\epsilon)}{\partial \epsilon} f(\dot{\epsilon}) \tag{1.2}$$

In using a macro-scale material law parameters need to be supplied to fit the behavior of the model to the material response. However, in terms of the design information they can provide for the foam the application is limited to the shape and macro-scale properties of the foam. With the improvements to 3D printing techniques, it is possible to design custom foam geometries [65]. The information needed for optimal choices of material on the macro scale involve combinations of the properties of the different aspects of the material on the micro-scale. With the detail that 3D printing can provide, it is necessary to be able to measure how the changes at the micro-scale impact the performance of the material at the macro-scale. With this desire to be able to improve the performance of foam liners, the investigation will take place using beam network models to represent the micro-structure of the foam. More details about this are covered in section 2.1.

Shocks In Cellular Materials

The material responses discussed in section 1.3, deal with continuous deformation of a cellular material. When the rates of deformation are fast enough then there is not enough time for the material to even react at the part scale, the response will be isolated to the ligaments and cells near the deformation. In these cases the loading resistance is provided by a series of impact events of the foam microstructure against itself and/or the loading surface [28]. It is in these types of loading events that a lot of bullet and blast impact can take place. Thus it is of interest to be able to determine the expected macro-scale behavior from the microstructure.

In an impact event at high enough velocity, the dominant material response is not the static or quasi-static response of the material, but rather the deformation waves that propagate though the body. The types of changes that propagate through the material are dependent on the material's properties and the loading rate of the material [1]. For a linear elastic material, an elastic wave will propagate though the material from the place of impact to the rest of the material. In a collision several types of waves will be generated, using pressure waves as an example, the speed the elastic deformation will propagate is given by:

$$c_s = \sqrt{\left.\frac{\partial p}{\partial \rho}\right|_{\eta}} \tag{1.3}$$

which for can be rewritten in terms of elastic material constants as:

$$c_s = \sqrt{\frac{K}{\rho}} \tag{1.4}$$

Where p is the pressue, ρ is the density, K is the bulk modulus and $\frac{\partial}{\partial \cdot}|_{\eta}$ is the derivative at constant entropy. As illustrated in figure 1.10 this type of material will advect the local deformation though the material at a constant velocity c_s. Even if the form of the deformation is not smooth, the propagation of discontinuity will still propagate forward with speed c_s (ignoring dispersive type effects)[34].

If the material instead had been strain hardening, like a foam material, the larger deformations have wave speed higher than the smaller deformations, as illustrated in figure 1.10. Thus, they travel faster and induce a jump in the state of the material at the front of the wave. Traditional conservation laws will be insufficient for modeling this behavior because those laws often require the existence of a derivative. In the case of a shock, a set of jump conditions need to be established in order to describe the local behavior at the shock front correctly.

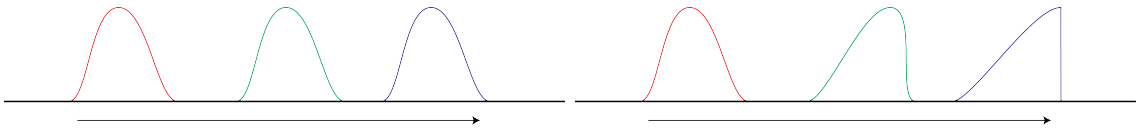

Figure 1.10: Wave Propagation through a (Left) linear elastic material and (Right) a strain hardening elastic material. It can be observed that where the linear material has its deformations move at the same speeds, and the change in deformation is smooth, while in the hardening case all of the deformation occurs at once.

One approach for describing the shock behavior of for cellular materials was proposed by Reid [69]. Reid's approach was to assume that during the compression of cellular materials the material response can be modeled as a rigid, perfectly-plastic, locking (RPPL) material, see figure 1.11 for an illustration of the model. The model asserts if the model deforms it will do so at a constant stress, σ_c, until the the material reaches its locking strain, ϵ_L. When the material reaches ϵ_L deformation is halted and the stress in the material will have and additional 'enhancement' stress added to maintain the current state of strain. The critical stress is set to the plateau stress and the locking strain is chosen to be within the densification regime.

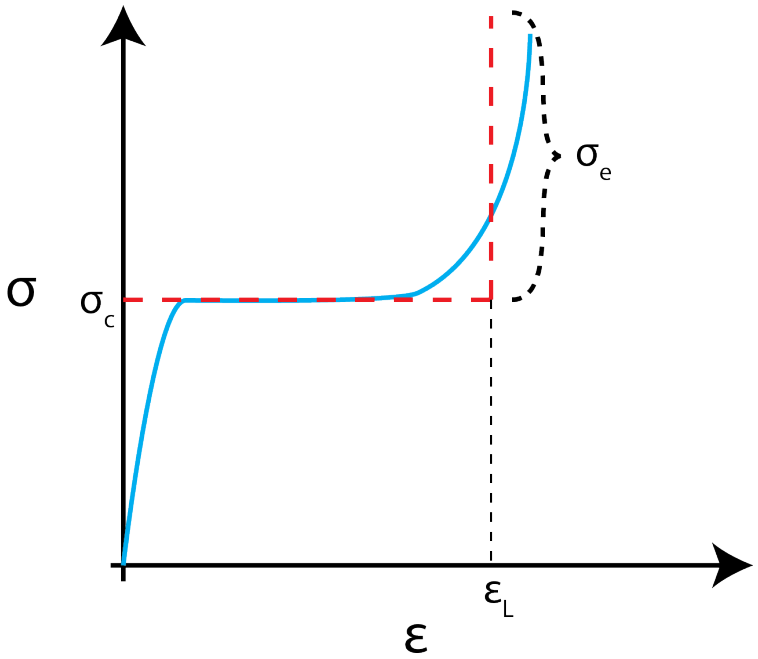

Figure 1.11: Illustration of the rigid,perfectly-plastic, locking approximation(dashed red) on top of the ideal compressive loading curve of a foam model(solid blue).

The relevant equations from [69] are summarized below:
Ratio of density:

$$\gamma = \frac{\rho_0}{\rho_1} = 1 - \epsilon_L \tag{1.5}$$

Stress enhancement based on the impact velocity (U_{imp}), the critical stress (σ_c), and shock speed (C_s):

$$\sigma^* = \sigma_c + \sigma_e = \sigma_c + \frac{\rho_0 C_s U_{imp}}{\gamma} = \sigma_c + \frac{\rho_0 U_{imp}^2}{\epsilon_L} \tag{1.6}$$

Shock Speed Relation:

$$C_s = \frac{\gamma}{1-\gamma} U_{imp} = \frac{1-\epsilon_L}{\epsilon_L} U_{imp} \tag{1.7}$$

Equation 1.7 suggests that there is a linear relation relating the shock speed to the impacting velocity speed. Thus through experiments it should be possible to recover a relation of shock speed to impact velocity in the following form:

$$C_s = c_1 U_{imp} \tag{1.8}$$

In Reid's work the shock speed C_s is described relative to the impacting velocity if the shock speed is reported in the lab frame then equations 1.8 and 1.7 can be combined to obtain:

$$\epsilon_L = \frac{1}{c_1} \tag{1.9}$$

With equation 1.9 it is then possible to supplement the critical stress obtained from static testing of foams with the locking strain to define a one dimensional model.

1.4 Outline

The mission for this work is to develop and implement an appropriate finite element model that is capable of replicating the mechanics of a flexible open-celled polyurethane foam, demonstrate its use in modeling the rapid compression of foams and use the mode to obtain locking stains to supply the RPPL model.

The rest of the document is organized as follows: In chapter 2, the beam network model will be introduced and the beam model used in the work will be discussed. In chapter 3, the implementation of be beam model into finite element frame work will be discussed and challenges relevant to the rapid dynamic crushing of foams will be discussed. In chapter 4, the process of generating regular and irregular geometries for the model will be detailed. In Chapter 5, results for crushing experiments will be shown and discussed. Lastly, in chapter 6, a summary of the work done will be presented along with ideas and for future work.

Chapter 2

Beam Model

2.1 Foam Model Overview

In any model, approximations about the physics must be made in order to allow for a solution to be found with the tools available. In many models this requires use of average/effective properties of smaller scale physics [66]. At a basic level all models consist of two parts; a from, which are the equations that are assumed describe the system of interest, and parameters. The parameters take the general form and make it specific to the details of the system. For example in systems with growth an exponential may be used to model the system, $p = p_0 e^{\frac{t}{\tau}}$. Then when one wants to model bacterial growth p_0 become the initial population and τ become the characteristic growth time.

Like in the example, effective models average the different aspects of the small scale physics, incorporating into them the form the the model and the parameters prescribed. Because of the averaging of aspects at the smaller scale, a form and values at the larger scale can not necessarily be translated to the corresponding configuration (material/geometry/etc.) at the smaller scale. Thus, while optimal values for parameters at larger scale can be found, the problem of mapping these values to the arrangement on the smaller scale is often not direct. To find the corresponding configurations of the small scale, the small scale itself must be modeled and then tested to see if it matches. If a match is not found the configuration will be altered and tested again, this process is repeated until the desired results are found.

When modeling a helmet's protective performance it is necessary to use full scale models of the helmet. This is at a size scale too large to model the microstructure of the foam liners (10's mm versus .1mm). In these full scale tests effective models need to be used, like described in equation 1.2. If a particular macro-scale parameter is sought from the foam microstructure, a microstructural model is needed. The microstructure model presented in this chapter can serve to in this translational roll between desired macro-scale parameters and the design of the micro-scale.

Open-celled foams are characterized by a series of ligaments that connect at nodes, as

shown in figure 1.6. These ligaments have one dominant spatial dimension with two smaller spatial dimensions. While studies of cellular microstructure have been done with traditional continuum mechanics, in which all points in the solid state are modeled [59, 76, 78] the cost of a full discretization is expensive, and limits the scale at which the simulation can be run.

Assuming that the exact detail of the deformation outside of the main axis of the ligament is not vitally important, the ligaments can be approximated as beams. The use of beams to model the structure reduces the cost of modeling a ligament by transforming a problem regarding a three dimensional object in three dimensional space to a one dimensional object in three dimensional space. This transformation now only requires solving the physics along the axial length of the beam and not at all points within the beam, thus allowing for simulations with greater numbers of ligaments than in the fully discretized case.

Networks of beams have been used by a variety of researchers, with a large amount of work done in two dimensional simulations of both open- and closed- cell foams. Zheng [91, 92] has conducted studies of the crushing of two dimensional honeycombs, with regards to plasticity effects and characterizing the modes of collapse based on the visual pattern that appears into "X","V" and "I". Zheng's work builds on the studies conducted by Ruan [71] who studied the rate dependent nature of the different collapsing modes. Liang et. al [51] expanded upon the work of Zheng by observing crushing behaviors of foams with gradients in their cell size and density. Nguyen [62] explored two dimensional homogenization of irregular honeycomb-like networks, and implemented an adaptive polynomial fit boundary constraint, in order to enforce periodic boundary conditions. This is particularly significant because unlike structured grids which are common for homogenization problems, the irregular presence of solid members on the boundary creates difficulties imposing boundary conditions.

In the three dimensional space the most notable work has been done by Kyriakides, Gong and Gaitanaros [25, 7, 24, 31, 32]. In their work macro-scale linear elastic material constants were derived using from a three dimensional analysis using a Kelvin cell model along with detailed descriptions of the ligament geometry and response. Along side the linear elastic matching, the microstructural response to part scale buckling was studied using two dimensional models. Later, their work focused on the experimentation and numerical simulation of crushing of aluminum foams. In their work they perform some of the more detailed foam geometry generation through their use of soap froth simulations. The work focused on observing the crush behavior of the metal foam during a Hopkins bar experiment, from which shock based material properties were derived.

Work on the derivation of linear elastic material constants for Kelvin geometries,similar work has been done by Wallach and Gibson [83] ,and more extensively by Vigliotti [82]. Jang and Kyriakides [42] explored the differences in three dimensional geometries of Kelvin cells and cells generated using a randomized voronoi technique. Their results show that the randomized technique produces similar results to the regular cells, but with a higher stiffness and plateau. Gan [26] in the effort to efficiently ascertain effective linear elastic bulk properties from randomized foams, performed representative volume size studies concluding that for the determination of linear elastic properties a 5x5x5 cell is sufficient.

To the author's knowledge, there have not been studies of three-dimensional polymeric

foam microstructure under rapid impact simulations. This work will follow similarly to the work done by Kyriakides and Gaitanaros. In the author's work the speeds of impact are higher than those studied by Kyriakides and Gaitanaros In addition, Kyriakides and Gaitanaros studied aluminum,a metal. In this dissertation the material of interest is a flexible polymer. As metal ligaments deform and buckle, they will undergo plastic deformation which will extract energy from the mechanical system. This energy loss is useful in the stabilization of the material. In materials lacking plastic deformation, much of this energy will instead be stored as elastic potential energy. The release of the potential energy can be violent, leading to numerical stability issues. This issue will be discussed in more detail in section 3.3.

This chapter presents the mechanics behind the foam micro-structural model used, in chapter 4 details of how the mechanics are implemented using finite elements are discussed. The model proposed uses beams to represent the different ligaments present in an open-celled foam, with interactions between the ligaments being driven by shared corner points and contact between the ligaments. In the remainder of this chapter a brief review of continuum mechanics will be presented, followed by a description of Green- Naghdi beam/rod model, and how the beam ligaments are assembled into a network.

2.2 Mechanics

Following is a brief review of continuum mechanics, referencing [15] and [63], presented so that the formulation of the Green-Naghdi beam theory can be understood in the context of general continuum mechanics.

Kinematics

A body($\mathbb{B}$) can be considered a collection of material points $\mathbb{X}$:

$$\mathbb{X} \in \mathbb{B} \tag{2.1}$$

These points represent the individual "chunks" of material that comprise the body as a whole. We assume that all of these material points ($\mathbb{X}$) can be mapped into three dimensional space, by an operator χ. This mapping can be time dependent, such that at a time t we can map $\mathbb{X}$ to the three dimensional space vector $\vec{x}$ at time t by:

$$\vec{x}(t) = \chi(\mathbb{X}, t) \tag{2.2}$$

$$\vec{x}(t) = x_1\vec{E}_1 + x_2\vec{E}_2 + x_3\vec{E}_3 \tag{2.3}$$

Where x_i represents the coordinate values for the spacial position and $\vec{E}_i$ represents the basis vectors for a rectangular Cartesian coordinate system. At a time, t_0 we can take the body to be in a configuration that allows us to base other observations off of it. This configuration

is known as the reference configuration, where the material points occupy the positions $\vec{X}$, given by:

$$\vec{X} = \chi(\mathbb{X}, t_0) \tag{2.4}$$

$$\vec{X} = X_1\vec{E}_1 + X_2\vec{E}_2 + X_3\vec{E}_3 \tag{2.5}$$

The reference configuration is often taken to be a state without any internal or external loads, however this is not necessary. At other times we will say that we have some current configuration given by equation 2.2. Assuming a one-to-one mapping for χ holds, we can invert our mapping on the reference configuration to give:

$$\chi^{-1}(\vec{X}, t_0) = \mathbb{X} \tag{2.6}$$

Using equation 2.6 we can write the mapping of $\mathbb{X}$ into the current configuration.

$$\vec{x} = \chi(\chi^{-1}(\vec{X}, t_0), t) \tag{2.7}$$

where we can write rewrite χ into a form that maps the changw from the reference configuration to the current configuration.

$$\vec{x} = \hat{\chi}(\vec{X}, t; t_0) \tag{2.8}$$

With this new mapping($\hat{\chi}$) we have a one-to-one mapping of the positions in the reference configuration to the current configuration. Using this information, it is now permissible to assign a field that describes the change in position from the reference configuration to the current configuration. This field is known as the displacement field, $\vec{u}(X, t)$, where it additivly moves the refernce locations to the current locations as

$$\vec{x}(\vec{X}, t) = \vec{X} + \vec{u}(\vec{X}, t) \tag{2.9}$$

. The one-to-one mapping was necessary for us to write equation 2.9 because it ensures that one location in the reference configuration can not map to more than one location in the current configuration. If the preceding were not true, additional constraints or parameterizations would be necessary for describing a movement from the reference to the the current configuration.

This construction frames a method to measure the change in shape of a body. Using this frame changes in length can be measured. In the current configuration, we can have an infinitesimal section of the body $d\vec{x}$, which can be written as the product of a length, s, and a unit direction $\vec{m}$,

$$d\vec{x} = s\vec{m}. \tag{2.10}$$

Gaining a sense of the size of this piece of length we can calculate the square of its 2-norm,

$$\|\vec{v}\|_2 = \sqrt{\vec{v} \cdot \vec{v}} \tag{2.11}$$

$$\|d\vec{x}\|_2^2 = d\vec{x} \cdot d\vec{x} = s^2 m^T m = s^2 \tag{2.12}$$

Associating the sections of length in the reference configuration with lengths in the current configuration, is important for representing elastic materials. Taking the partial derivative in terms of the reference space of equation 2.9 we get the following:

$$\frac{\partial \vec{x}}{\partial \vec{X}} = \mathbb{I} + \frac{\partial \vec{u}}{\partial \vec{X}} \tag{2.13}$$

In component form:

$$\frac{\partial x_i}{\partial X_A} = \delta_{iA} + \frac{\partial u_i}{\partial X_A} \tag{2.14}$$

The left hand side of equation 2.13 is called the deformation gradient tensor F,

$$F = \frac{\partial \vec{x}}{\partial \vec{X}} = \mathbb{I} + \frac{\partial \vec{u}}{\partial \vec{X}} \qquad\qquad F_{iA} = \frac{\partial x_i}{\partial X_A} = \delta_{iA} + \frac{\partial u_i}{\partial X_A}. \tag{2.15}$$

The deformation gradient tensor can be used to associate aspects of the local shape in the reference configuration to the shape of the local area in the current configuration.

$$dx_i = F_{iA} dX_A \tag{2.16}$$

Using 2.16 and 2.12 to get:

$$d\vec{x} \cdot d\vec{x} = (Fd\vec{X})^T (Fd\vec{X}) = d\vec{X}^T F^T F d\vec{X} \tag{2.17}$$

Like in the current configuration, let the small segments in the reference configuration have the following decomposition, of a scalar length and a unit directional vector:

$$d\vec{X} = S\vec{M} \tag{2.18}$$

$$s^2 m^T m = S^2 M^T F^T F M \tag{2.19}$$

$$m^T m = 1 \tag{2.20}$$

$$\left(\frac{s}{S}\right)^2 = \vec{M}^T F^T F \vec{M} \tag{2.21}$$

In equation 2.21 there is now a description of how the length along a direction $\vec{M}$ in the reference configuration changes due to the deformation $\hat{\chi}$. The tensor $F^T F$ contains the information for this change, and is often assigned its own symbol, C.

$$C = F^T F \qquad\qquad C_{AB} = F_{iA} F_{iB} \tag{2.22}$$

C is commonly referred to as the right Cauchy-Green Stretch Tensor. While C contains all the information about the changes in length of the deformation, if there is no deformation the tensor is the identity. This is sometimes not desirable, because it can be nice to think of no deformation represented by zeros. To address this the Finite Lagrange Strain tensor is introduced:

$$\mathbb{E} = \frac{1}{2}(C - \mathbb{I}) \tag{2.23}$$

In addition to knowing the changes in length, knowing how the volume changes from the reference to the current configuration is useful. By taking the determinant of F, the Jacobian,J, is formed. J maps the volume of a point in the reference to its volume in the current confguration,

$$J \equiv det(F) \qquad\qquad dv = JdV. \tag{2.24}$$

Kinetics

With the ability to describe the changes in length of a body, these tools can be applied to describe how a body will respond to stresses. The conservation of linear momentum relates the stresses and body forces of the body to the positions rate of change at a point:

$$\nabla_x \cdot T + \rho\vec{b} = \rho\dot{\vec{v}} = \rho\ddot{\vec{u}} \tag{2.25}$$

Where ρ is the current volumetric density, $\dot{\vec{v}}$ is the total derivative of velocity with respect to time, $\vec{b}$ is the body force, T is the Cauchy stress tensor, and $\nabla_x \cdot$ denotes the divergence operator in the current configuration. T can be defined to be the force upon a given surface($\vec{t}$) that is described by a surface normal ($\vec{n}$),

$$T\vec{n} = \vec{t}. \tag{2.26}$$

It is advantageous to take advantage of the mapping of the reference configuration onto the current configuration, such that any calculations performed can be done on the static reference configuration, and not on the changing geometry of the current configuration. To do this the First Piola-Kirchhof is used. This operates on normals from the reference configuration, and supplies tractions in the current configuration.

$$d\vec{f} = \vec{t}da = T\vec{n}da = JTF^{-T}\vec{N}dA = P\vec{N}dA \tag{2.27}$$

Where Nanson's formula has been used to transform areas in the current configuration in the reference configuration. Explicitly, the First Piola-Kirchhof stress tensor is:

$$P = JTF^{-T} \tag{2.28}$$

The conservation of linear momentum can now be rewritten in the reference frame:

$$\nabla_X \cdot P + \rho_0\vec{b} = \rho_0\dot{\vec{v}} \tag{2.29}$$

To close the system it is necessary to associate the forces with the displacements and/or velocities. Elastic material laws associate the current strains a body is under to the current stresses the body is experiencing.

Thus representatively, we can write the first Piola-Kirchhof stress:

$$P = \hat{P}(F) \tag{2.30}$$

P is an asymmetric tensor, however elastic laws are often prescribed in a symmetric tensor in order to ensure the conservation of angular momentum. T is symmetric, and P is not. P can be transformed into a a symmetric form, known as the Second Piola-Kirchhof Stress tensor, S, and constitutive laws can be formed for it :

$$S = F^{-1}P = JF^{-1}TF^{-T} = \hat{S}(E) \tag{2.31}$$

Combining equation 2.31 and equation 2.29 :

$$\nabla_X \cdot (FS(E)) + \rho_0 \vec{b} = \rho_0 \dot{\vec{v}} \tag{2.32}$$

With equation 2.32 there is a general set up for solving a mechanical problem. The remaining components which need to be supplied are the geometry in the reference configuration, a specific constitutive law, and the boundary conditions along the surfaces of the body.

However equation 2.32 is a complicated, partial differential equation, that in general can be difficult to solve analytically. In many cases it is necessary to resort to numerical methods to obtain a solution to a given problem.

Convected Coordinates

In the previous section, the motion of a material point $\mathbb{B}$ was described as having a mapping to a spatial location, $\vec{X}$ in the reference and $\vec{x}$ in the current configuration. These points locations were described as being linear combinations of coordinate vectors. Often these vectors are set to be in the fixed Cartesian coordinate system. When a point changes its location in space, the coordinate vectors remain the same, but their scaling value changes.

Cartesian is useful because of how simple derivatives are to define, however in some cases it is useful to abandon the Cartesian system to use a coordinate system that convects with the motion of the body's points, in other words, every point maintains its scaling it applies to the coordinate vectors, and the coordinate vectors themselves change, as illustrated in figure 2.1. In this section a brief introduction to convected coordinates is given because it is an important tool in forming the Green-Naghdi beams, for a more detailed discussion of convected coordinates please see [46].

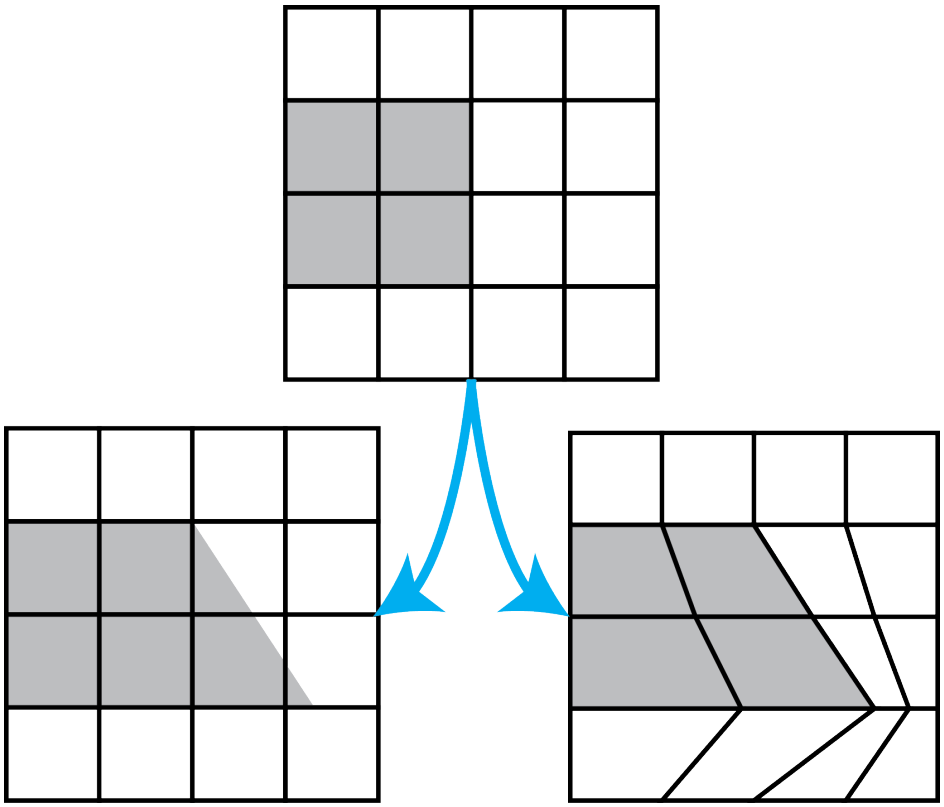

Figure 2.1: Left: Motion in unmoving coordinates. Right: The same motion, but in convected coordinates

lLet us define the current position of a point as follows:

$$\vec{x} = \vec{x}(\theta^1, \theta^2, \theta^3) \tag{2.33}$$

and the reference position of a point as:

$$\vec{X} = \vec{X}(\theta^1, \theta^2, \theta^3) \tag{2.34}$$

Where in equations 2.33 and 2.34, θ^i is a general coordinate. Where in the Cartesian form the coordinates values for a piece of material will change as it moves, in convected coordinates θ^i will remain the same for a piece of material. With these we can describe the local change in coordinate curves by writing the covariant bases vectors (equation 2.35). These vectors are tangent to the coordinate curves at the point of interest. These bases may not be orthogonal to one an other and may have magnitudes other than one. However the basis should be linearly independent, such that their box product is greater than zero (equation 2.36).

$$\vec{g}_i = \frac{\partial \vec{x}(\theta^1, \theta^2\theta^3)}{\partial \theta^i} \qquad \vec{G}_i = \frac{\partial \vec{X}(\theta^1, \theta^2\theta^3)}{\partial \theta^i} \tag{2.35}$$

$$\vec{g}_1 \times \vec{g}_2 \cdot \vec{g}_3 = \sqrt{g} > 0 \qquad \vec{G}_1 \times \vec{G}_2 \cdot \vec{G}_3 = \sqrt{G} > 0 \tag{2.36}$$

From the covariant basis is is possible to form the contravariant basis:

$$\vec{g}^1 = \frac{\vec{g}_2 \times \vec{g}_3}{\sqrt{g}} \qquad \vec{g}^2 = \frac{\vec{g}_3 \times \vec{g}_1}{\sqrt{g}} \qquad \vec{g}^3 = \frac{\vec{g}_1 \times \vec{g}_2}{\sqrt{g}} \tag{2.37}$$

Each contravariant base vector is perpendicular to the plane formed by two covariant basis vectors. The covariant and contravariant bases scale inversely from one an other and have the following property:

$$g^i g_j = \delta^i_j = \left\{ \begin{array}{ll} i = j & 1 \\ i \neq j & 0 \end{array} \right\} \tag{2.38}$$

These bases can be used to quantify the components of various tensors in a space. For a first order tensor (vector):

$$\vec{u} = u^i g_i = u_i g^i \tag{2.39}$$

For a second order tensor:

$$T = T^{ij} g_i \otimes g_j = T_{ij} g^i \otimes g^j = T^i_j g_i \otimes g^j = T^j_i g^i \otimes g_j \tag{2.40}$$

To transform the constants between co- and contra- variant bases the fundamental tensor may be used:

$$g_{ij} = g_i \cdot g_j \qquad g^{ij} = g^i \cdot g^j \tag{2.41}$$

Using the properties seen in 2.38, 2.39 and 2.40, the coefficients are transformed by:

$$u^i = g^{ij} u_j \qquad u_i = g_{ij} u^j$$

Using the covariant and contravariant bases, in the reference and current configuration it is possible to write the deformation tensor F.

$$F = g_i \otimes G^i \qquad F^{-1} = G_i \otimes g^i \tag{2.42}$$

$$F^{-T} = g^i \otimes G_i \qquad F^T = G^i \otimes g_i \tag{2.43}$$

Seeing this, it is possible to write the right stretch tensor:

$$C = F^T F = G^i \otimes g_i g_j \otimes G^j = g_{ij} G^i \otimes G^j \tag{2.44}$$

2.3 Green-Naghdi Beam Theory

Here the the theory for Green-Naghdi beam theory will be derived, in a similar manner as done in [74]. In the following $(\cdot)^*$ variables indicate the form of the variable before it has been acted upon by forms of the model, and α and other Greek sub/super-scripts will be used to index $\{1, 2\}$, while Latin sub/super-scripts will denote the set $\{1, 2, 3\}$.

Cosserat Theory

If it can be assumed that there exists a physical body that is thin in all dimensions except one, then the main spatial parameter of all physical fields in the body is the length along the one large dimension. Let $\vec{x}^*$ represent the general three dimensional space, then $\vec{x}$ can describe a curve in three dimensional space, at a particular time(t), by:

$$\vec{x} = \vec{x}^*(0, 0, \theta^3, t) \tag{2.45}$$

Where θ^3 is the arc length parameter, defined as the distance away from one end of the curve. The curve by itself in its current condition can only support tensile and compressive stresses along the tangent of the curve. Thus, without further enhancement only a string-like object could be described. To add the ability for the curve to resist bending and torsion, smaller dimensions of the body need to be incorporated. The cross-section of be body is represented by attaching two vectors to the curve known as directors. These directors describe the behavior away from the curve in less detail, but provide a framework to attach bending and torsional resistances. A third director, the tangent vector of the curve($\vec{d_3} \equiv \frac{\partial x_0}{\partial \theta^3}$), is also used.

Continuing to use θ^3 as the arc length coordinate, θ^1 and θ^2 are used to represent positions in the cross-section of a beam. Each of the cross-section coordinates are paired with a director to represent the cross-section of the beam as a plane. To describe any point in the beam, one can write it in terms of the curve and the directors, in both the current and reference configuration:

$$\vec{x}^* = \vec{x}(\theta^3) + \theta^\alpha \vec{d}_\alpha(\theta^3, t) \qquad \vec{X}^* = \vec{X}(\theta^3) + \theta^\alpha \vec{D}_\alpha(\theta^3, t) \tag{2.46}$$

$$\vec{d}_\alpha(\theta^3, t) = \vec{D}_\alpha(\theta^3, t) + \vec{\delta}_\alpha(\theta^3, t) \tag{2.47}$$

Where $\vec{d}_\alpha$ are the attached directors in the current configuration, $\vec{D}_\alpha$ are the attached directors in the reference configuration, and $\vec{\delta}_\alpha$ is the deformation of the attached vectors bringing the reference to the current. Velocity can likewise be defined as:

$$\vec{v}^* = \vec{v}(\theta^3) + \theta^\alpha \vec{w}_\alpha \qquad \vec{V}^* = \vec{V}(\theta^3) + \theta^\alpha \vec{W}_\alpha \tag{2.48}$$

$\vec{w}$ is the rate of change of the directors. In the form presented it is assigned that $absmax(\theta^\alpha) \approx 1$, with the directors scaling in magnitude to describe the size of the cross-section. In terms of what is 'small', in [74] the largest cross-sectional diameters presented were a twentieth the length of the beam. The covariant basis can be written in terms of the directors by:

$$\vec{g}_1 = \vec{d}_1 \qquad \vec{g}_2 = \vec{d}_2 \qquad \vec{g}_3 = \vec{d}_3 + \theta^\alpha \frac{\partial d_\alpha}{\partial \theta^3} \tag{2.49}$$

With the respective forms in the reference configuration. The deformation gradient will be assumed to be of the form:

$$F = \vec{d}_i \otimes \vec{D}^i \tag{2.50}$$

Thus equation 2.50 drops F's dependence on θ^α and $\frac{\partial d_\alpha}{\partial \theta}$. However $\frac{\partial d_\alpha}{\partial \theta}$ is important for describing the bending and torsion of the beam. To make up for this an other 'strain' like measure is defined; λ_α and Λ_α. λ_α and Λ_α will be used to introduce elastic stresses along with the assumed form of F. λ_α and Λ_α are defined by:

$$\lambda_\alpha = F^{-1}\left(\frac{\partial \vec{d}_\alpha}{\partial \theta^3} \otimes \vec{D}^3\right) \tag{2.51}$$

$$\Lambda_\alpha = \frac{\partial \vec{D}_\alpha}{\partial \theta^3} \otimes \vec{D}^3 \tag{2.52}$$

Including the assumption from equation 2.50 the fundamental tensor(metric tensor, C) for is:

$$g_{ij} \Rightarrow d_{ij} = \vec{d}_i \cdot \vec{d}_j \tag{2.53}$$

In this manner of describing the geometry of the beam the motions of all three directors are not constrained to one another. Unlike in linear beam theories, where the cross-section is assumed to remain perpendicular to the tangent of the center line, in this form the cross-section can rotate independently of the direction of the tangent. The cross-section also has the means to alter its shape as the first and second director move relative to each other.

Conservation Laws

Applying the kinematic assumptions about the ligaments to the conservation of mass and linear momentum allows for a simplified version of theses laws to be used when describing the motion of the ligament. By directly substituting the kinematic assumption into the conventional form of the conservation laws and integrating over the cross-section the equations governing the beam's response to forces can be captured within the displacement of the curve and the deformation of the directors.

In the following section, the transformations of the conservation of mass and linear momentum are presented. In addition, a new conservation law is added, the conservation of director momentum. The basic procedure for the derivation of the beam approximation will be presented explicitly for the conservation of mass, and then summarized for the other laws. In all of these derivations the integral form of the conservation laws are used, and different regions of the beam are treated differently. A reference for how these regions are defined is given in figure 2.2.

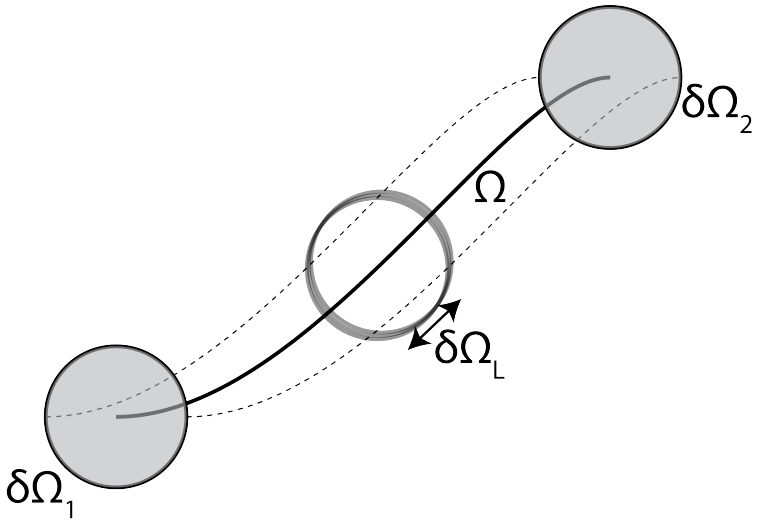

Figure 2.2: Illustration of a beam member. Circles were chosen to represent the shape for the beam's cross-section but the theory does not require this.Ω is the volume of the beam, $\partial\Omega_\alpha$ represent the ending surfaces of the beam, $\partial\Omega_L$ is the lateral surface of the beam, and the solid line is the 'center' curve of the beam.

Conservation of Mass In traditional continuum mechanics it is assumed that for a closed body there is no mass change over a subset of the body, and thus:

$$\frac{d}{dt}\int_{\Omega^*}\rho^* dv^* = 0 \tag{2.54}$$

where ρ^* is the mass per unit volume definition of density, and dv^* is the conventional differential volume. If equation 2.54 is taken and the volume integral is broken into an area integral across the cross-section(area, A^*) and an integral along a curve(arc length,s^*) the following is obtained:

$$\int_{\Omega^*}\rho^* dv^* = \int_{s_1}^{s_2}\int_{A^*}\rho^* da^* ds^* \tag{2.55}$$

Using curvilinear coordinates equation 2.55, can be transformed into an integral over a fixed set of values, yielding:

$$\int_{\Omega^*}\rho^* dv^* = \int_{\theta_1^3}^{\theta_2^3}\int_{A}\rho^*\sqrt{g}d\theta^1 d\theta^2 d\theta^3 \tag{2.56}$$

Assuming a density that is constant across the cross-section and integrating:

$$\int_{\Omega^*}\rho^* dv^* = \int_{\theta_1^3}^{\theta_2^3}\rho\sqrt{d_{33}}d\theta^3 \tag{2.57}$$

It is then possible to transform this new density, one with units of mass per unit length, back to the the current spatial system to obtain:

$$\int_{\Omega^*} \rho^* dv^* = \int_{s_1}^{s_2} \rho ds^* \tag{2.58}$$

If the procedure above is follow but the reference configuration is used the following is obtained:

$$\int_{\Omega^*} \rho^* dv^* = \int_{\theta_1^3}^{\theta_2^3} \rho_0 \sqrt{D_{33}} d\theta^3 \tag{2.59}$$

Equating equations 2.59 and 2.57 the relationship between the reference and current density can be obtained.

$$\int_{\theta_1^3}^{\theta_2^3} \rho \sqrt{d_{33}} d\theta^3 = \int_{\theta_1^3}^{\theta_2^3} \rho_0 \sqrt{D_{33}} d\theta^3 \Rightarrow \rho \sqrt{d_{33}} = \rho_0 \sqrt{D_{33}} \tag{2.60}$$

Below are some transformations of density which will make notation later in the section less cluttered.

$$m = \rho \sqrt{d_{33}} = \rho \left\| \frac{\partial \vec{x}}{\partial \theta^3} \right\| = \rho_0 \left\| \frac{\partial \vec{X}}{\partial \theta^3} \right\| \tag{2.61}$$

$$m^* = \rho^* \sqrt{g}$$

Conservation of Linear Momentum The conservation of linear momentum follows a similar pattern to the derivation of the conservation of mass, however additional complexity is added because of the need to integrate over θ^α. The conventional conservation of linear momentum in the integral form is:

$$\frac{d}{dt} \int_{\Omega^*} \rho^* \vec{v}^* dv^* = \int_{\Omega^*} \rho^* \vec{b}^* dv^* + \int_{\partial\Omega_1} \vec{t}^* da^* + \int_{\partial\Omega_2} \vec{t}^* da^* + \int_{\partial\Omega_l} \vec{t}^* da^* \tag{2.62}$$

Transforming the volume integrals into line and area integrals and then substituting 2.48:

$$\frac{d}{dt} \int_{\theta_1^3}^{\theta_2^3} \int_A m^* (\vec{v} + \theta^\alpha \vec{w}_\alpha) d\theta^1 d\theta^2 d\theta^3 = \int_{\theta_1^3}^{\theta_2^3} \int_A m^* \vec{b}^* d\theta^1 d\theta^2 d\theta^3 * + \int_{\partial\Omega_1} \vec{t}^* da^* + \int_{\partial\Omega_2} \vec{t}^* da^* + \int_{\partial\Omega_l} \vec{t}^* da^* \tag{2.63}$$

Performing the area integral the following form of the left hand side can be written as:

$$\int_A m^* (\vec{v} + \theta^\alpha \vec{w}_\alpha) d\theta^1 d\theta^2 = \vec{v} m + m y^\alpha \vec{w}_\alpha \tag{2.64}$$

With

$$my^{\alpha} = \int_A m^* \theta^{\alpha} d\theta^1 d\theta^2 \tag{2.65}$$

A similar procedure can be performed on the integral of the body force:

$$\int_A m^* \vec{b}^* d\theta^1 d\theta^2 d = m\vec{b}_b \tag{2.66}$$

The surface tractions on the beam undergo a more complicated set of manipulations, if one wishes to see more detail of this please read [74] or [63]. The surface traction of the beam can be rewritten in such a way that it effectively becomes another body type force. It is through this term that effects such as contact can be applied.

$$\int_{\partial\Omega_l} \vec{t}^* da^* = \int_{s_1}^{s_2} \rho \vec{b}_c ds \tag{2.67}$$

The tractions on the end of the beam are integrated over their areas. Then recognizing that the surface of the beam on both ends have opposite normal directions in terms of the arc length, the sum of the tractions integrals are rewritten as the difference of their end forces:

$$\int_{\partial\Omega_1} \vec{t}^* da^* + \int_{\partial\Omega_2} \vec{t}^* da^* = \left[\vec{t}^3\right]_1^2 \tag{2.68}$$

Putting all of the parts together and back into equation 2.63 gives:

$$\frac{d}{dt}\int_{s_1}^{s_2} (\rho\vec{v} + \rho y^{\alpha}\vec{w}_{\alpha}) ds = \int_{s_1}^{s_2} \rho\vec{b}_b + m\vec{b}_c ds + \left[\vec{t}^3\right]_1^2 \tag{2.69}$$

Locallizing:

$$m\frac{d\vec{v}}{dt} + my^{\alpha}\frac{d\vec{w}_{\alpha}}{dt} = m\vec{b}_b + m\vec{b}_c + \vec{t}^3_{,3} \tag{2.70}$$

Conservation of Director Momentum Conservation of director momentum is introduced to the classic conservation laws in order to provide additional equations to govern the deformation of the beam. These equations also arise if one takes appropriate variations of the energetic potential using equations 2.46 and 2.48. Without performing this calculation, the conservation of director momentum is presented, and proposed that one considers it the conservation of the weighted average of linear momentum along the area of the beam's cross-sections.

The weighted average of the conservation of linear momentum by a scalar ϕ is:

$$\frac{d}{dt}\int_{\Omega^*} \rho^*\phi\vec{v}^* dv^* = \int_{\Omega^*} \rho^*\phi\vec{b}^* dv^* - \int_{\Omega^*} \sqrt{g}\phi_{,j} T^* \vec{g}^j dv^* \tag{2.71}$$

$$+ \int_{\partial\Omega_1} \phi\vec{t}^* da^* + \int_{\partial\Omega_2} \phi\vec{t}^* da^* + \int_{\partial\Omega_l} \phi\vec{t}^* da^*$$

To obtain the conservation of director momentum ϕ is set to θ^α, this gives an additional set of equations because of the two possible values for α

$$\frac{d}{dt}\int_{\Omega^*}\rho^*\theta^\alpha\vec{v}^*dv^* = \int_{\Omega^*}\rho^*\theta^\alpha\vec{b}^*dv^* - \int_{\Omega^*}\sqrt{g}\theta^\alpha_{,j}T^*\vec{g}^j dv^* \tag{2.72}$$

$$+\int_{\partial\Omega_1}\theta^\alpha\vec{t}^*da^* + \int_{\partial\Omega_2}\theta^\alpha\vec{t}^*da^* + \int_{\partial\Omega_l}\theta^\alpha\vec{t}^*da^*$$

With the equtations from 2.72, equation 2.48 is substituted and the volume integrals are split.

$$\frac{d}{dt}\int_{\theta_1^3}^{\theta_2^3}\int_A m^*(\theta^\alpha\vec{v}+\theta^\alpha\theta^\beta\vec{w}_\beta)d\theta^1d\theta^2d\theta^3 = \int_{\theta_1^3}^{\theta_2^3}\int_A m^*\theta^\alpha\vec{b}^*d\theta^1d\theta^2d\theta^3 - \int_{\theta_1^3}^{\theta_2^3}\int_A \delta^\alpha_j\sqrt{g}T^*\vec{g}^j d\theta^1d\theta^2d\theta^3 \tag{2.73}$$

$$+\int_{\partial\Omega_1}\theta^\alpha\vec{t}^*da^* + \int_{\partial\Omega_2}\theta^\alpha\vec{t}^*da^* + \int_{\partial\Omega_l}\theta^\alpha\vec{t}^*da^*$$

Like in previous derivations the inertial terms are integrated over their area.

$$\int_A m^*(\theta^\alpha\vec{v}+\theta^\alpha\theta^\beta\vec{w}_\beta)d\theta^1d\theta^2d\theta^3 = my^\alpha\vec{v} + my^{\alpha\beta}\vec{w}_\beta \tag{2.74}$$

A new inertial term is introduced :

$$my^{\alpha\beta} = \int_A m^*\theta^\alpha\theta^\beta d\theta^1d\theta^2 \tag{2.75}$$

Note that equations 2.75 and 2.65 the left hand side should be thought of as one term unless it can be assumed that the density of the rod is homogeneous, in which case the terms can be separated freely.

The body forcing term is again integrated over its area, however now weighted by the coordinates of the director.

$$\int_A m^*\theta^\alpha\vec{b}^*d\theta^1d\theta^2d\theta^3 = m\vec{b}^\alpha_b \tag{2.76}$$

$\sqrt{g}T^*\vec{g}^i$ is the curvilinear analogy to the Cartesian statement $T\vec{n}$. With this the traction volume integral can be rewritten to a form that gives a single vector:

$$\int_A \delta^\alpha_j\sqrt{g}T^*\vec{g}^j d\theta^1d\theta^2 = \int_A \vec{t}^{*\alpha}d\theta^1d\theta^2 = \vec{t}^\alpha \tag{2.77}$$

The tractions along the sides of the beam are again transformed into body force like terms, but with the weighting of the coordinates:

$$\int_{\partial\Omega_l} \theta^\alpha \vec{t}^* da^* = \int_{\theta_1^3}^{\theta_2^3} m\vec{b}_c^\alpha d\theta_3 \tag{2.78}$$

The weighted averages of the terminal tractions do not have a convent transformation into other terms. These terms do however relate to the moment applied to the body, thus let:

$$\int_{\partial\Omega} \theta^\alpha \vec{t}^* da^* = \vec{m}^\alpha \tag{2.79}$$

$$\vec{\mathbf{m}} = \vec{d_\alpha} \times \vec{m}^\alpha \tag{2.80}$$

Where $\vec{\mathbf{m}}$ is the moment about a point. From there we can transform the sum of the terminal tractions to become:

$$\int_{\partial\Omega_1} \theta^\alpha \vec{t}^* da^* + \int_{\partial\Omega_2} \theta^\alpha \vec{t}^* da^* = -\vec{m}^\alpha_{\partial\Omega_1} + \vec{m}^\alpha_{\partial\Omega_2} = [\vec{m}^\alpha]_1^2 \tag{2.81}$$

Again the end provide us a term that has a jump in its nature. Taking all the parts and putting them together gives the integral from of the conservation of director momentum:

$$\frac{d}{dt}\int_{s_1}^{s_2} my^\alpha \vec{v} + my^{\alpha\beta}\vec{w}_\beta ds = \int_{s_1}^{s_2} m(\vec{b}_b^\alpha + \vec{b}_c^\alpha) - \vec{t}^\alpha ds + [\vec{m}^\alpha]_1^2 \tag{2.82}$$

Localizing:

$$my^\alpha \frac{d\vec{v}}{dt} + my^{\alpha\beta}\frac{d\vec{w}_\beta}{dt} = m(\vec{b}_b^\alpha + \vec{b}_c^\alpha) - \vec{t}^\alpha + \frac{\partial \vec{m}^\alpha}{\partial\theta^3} \tag{2.83}$$

2.4 Constitutive Properties

In summary we have the following balance laws to consider:

Mass:

$$m = \rho\sqrt{d_{33}} = \rho \left\| \frac{\partial \vec{x}}{\partial\theta^3} \right\| = \rho_0 \left\| \frac{\partial \vec{X}}{\partial\theta^3} \right\| \tag{2.84}$$

Linear Momentum:

$$m\frac{d\vec{v}}{dt} + my^\alpha \frac{d\vec{w}_\alpha}{dt} = m\vec{b}_b + m\vec{b}_c + \vec{t}^3_{,3} \tag{2.85}$$

Director Momentum:

$$my^\alpha \frac{d\vec{v}}{dt} + my^{\alpha\beta}\frac{d\vec{w}_\beta}{dt} = m(\vec{b}_b^\alpha + \vec{b}_c^\alpha) - \vec{t}^\alpha + \frac{\partial \vec{m}^\alpha}{\partial\theta^3} \tag{2.86}$$

In the above equations, the fields of interest are; displacement($\vec{u}$), velocity($\vec{v}$), director displacement ($\vec{\delta}_\alpha$), and director velocity ($\vec{w}_\alpha$). The other unprescribed fields ($\vec{t}^i$ and $\vec{m}^\alpha$) need to be determined by additional equations to close the system.

The Zorbium forma liners are a flexible polyurethane-based foam, thus the individual struts in the foam are polyurethane. It will be assumed that the individual ligaments will behave like beams comprised of a bulk polyurethane material. The material will be assumed to have an elastic and dissipative response such that:

$$\vec{t}^{\,i} = \vec{t}^{\,i}_e \left(C \left(\frac{\partial \vec{u}}{\partial \vec{x}}, \vec{\delta}^{\alpha} \right) \right) + \vec{t}^{\,i}_d \left(\frac{\partial \vec{v}}{\partial \vec{x}} \right) \tag{2.87}$$

and

$$\vec{m}^{\alpha} = \vec{m}^{\alpha}_e \left(\lambda \left(\frac{\partial \vec{\delta}^{\alpha}}{\partial \vec{x}} \right) \right) \tag{2.88}$$

Thus it is necessary to obtain three material response behaviors to close the system of equations. In the determination of the constitutive models, there are several proposed methods to due so. Green and Naghdi [35] took the approach of directly integrating the three dimensional laws to derive relations. M.B. Rubin [73, 72] uses a decomposition of the elastic potential into two potentials, one which is active in all forms of deformation and the second which only contributes during inhomogeneous deformations. He then uses analogy of director-based strain terms to traditional three dimensional strain terms to be able to directly write an elastic potential for the material and thus get the elastic material laws. O'Reilly [64] uses an additive decomposition, with one term obtained by using direct integration. The second potential is then defined to be nonzero when deformation gradient is not equal to the approximated deformation gradient used in the theory. O'Reilly also discusses in his paper about how the selection of these methods for deriving material laws are to some degree arbitrary, thus selecting a method and getting fitting the data correctly are the most important aspects of generating the material laws.

In this research the techniques used by Rubin in [73] will be followed for obtaining the constitutive mdoels.

Elastic Properties Not covered previously in the transformation of the classical conservation theories to their beam form was the conservation of angular momentum. In classical continuum mechanics the conservation of angular momentum is used to prove that the stress tensor is symmetric:

$$T = T^T$$

When the techniques of the previous section are applied to the conservation of angular momentum it is seen that an object similar to the stress tensor needs to be symmetric. This object is a combination of the force and moment like terms. With this Rubin defines the analogous stress tensor.

$$T = \sqrt{d_{33}}^{-1} \left(\vec{t}^{\,i} \otimes \vec{d}_i + \vec{m}^{\alpha} \otimes \vec{d}_{\alpha,3} \right) = T^T \tag{2.89}$$

Using the definition of the stress tensor given by equation 2.89, it is possible to derive a T from an elastic potential and then equation 2.89 provides one of the closure equations

needed. Let ϕ be the a hyper-elastic potential the Cauchy stress tensor can be written as:

$$T = 2\rho F \frac{\partial \phi}{\partial C} F^T = \frac{\sqrt{D_{33}}}{\sqrt{d_{33}}} F S F^T \tag{2.90}$$

With T defined, a form for $\vec{m}^\alpha$ chosen it is possible to solve for $\vec{t}^i$ by:

$$\vec{t}^i = 2mF \frac{\partial \phi}{\partial C} \vec{D}^i - \vec{m}^\alpha (\vec{d}_{\alpha,3} \cdot \vec{d}^i) \tag{2.91}$$

In this model it has been chosen that the elastic material response will be governed by Neo-Hookean model where the elastic potential is given as [9]:

$$\phi(C) = \frac{\lambda}{2} ln(J)^2 - \mu ln(J) + \frac{\mu}{2}(tr(C) - 3) \tag{2.92}$$

and its symmetric reference stress tensor is given by:

$$S = \lambda ln(J) C^{-1} + \mu(\mathbb{I} - C^{-1}) \tag{2.93}$$

Rubin's technique is for determining a form for the moment-like traction terms is involved and is summarized below. It is worth noting that while the determination of the stress tensor is rather direct and is similar to the conventional three dimensional mechanics, the form of the momentum traction equations are dependent on the shape of the beam and changes in shape of the beam along its arc length. Thus a beam of non-constant cross-section would require additional terms to be added on to the constant cross-section equation.

In the end Rubin proposes a form for the material response for $\vec{m}^\alpha$ for a rectangular nonlinear isotropic rod as:

$$\vec{m}^\alpha = \frac{1}{\sqrt{D_{33}}} A F^{-T} \mathbb{K}^{\alpha\beta} \vec{\gamma}_\beta \tag{2.94}$$

where A is the scalar area of the cross-section, $\mathbb{K}^{\alpha\beta}$ is a constant parameter tensor comprised of material values and geometric constants. and $\vec{\gamma}$ is a new strain-likemeasure defined by:

$$\kappa_\alpha = \lambda_\alpha - \Lambda_\alpha \qquad \vec{\gamma}_\alpha = \kappa_\alpha \vec{D}^3 \tag{2.95}$$

$$K^{12} = K^{21} = 0 \qquad \zeta = \frac{H}{W} \tag{2.96}$$

$$K^{11} = \frac{\mu^* H^2}{6} \left[\left(\frac{b^*(\zeta)}{\zeta} \right) \vec{M}_2 \otimes \vec{M}_2 + (1 + \nu^*) \vec{M}_3 \otimes \vec{M}_3 \right] \tag{2.97}$$

$$K^{22} = \frac{\mu^* W^2}{6} \left[\zeta b^*(\zeta) \vec{M}_1 \otimes \vec{M}_1 + (1 + \nu^*) \vec{M}_3 \otimes \vec{M}_3 \right] \tag{2.98}$$

$$b^*(\zeta) = \frac{1}{\zeta}\left[1 - \frac{192}{\pi^5\zeta}\sum_{n=1}^{\infty}\frac{1}{(2n-1)^5}tanh\left(\frac{\pi\zeta(2n-1)}{2}\right)\right] \tag{2.99}$$

H and W are the heights and widths of the cross section and $\vec{M}_i$ is the unit direction of the directors in the reference configuration. It can be seen that equation 2.94 is a linear material law, while equation 2.90 is not necessarily linear. Equation 2.94 arises form gradients in the displacement of directors, thus is most applicable when there are small gradients of the directors. Like in small strain elasticity theory, large deformations may still result as the integral of small strains.

Dissipative Effects Polyurethane is a viscoelastic material, and at room temperatures exhibits a small but non-trivial amount of dissipation [22]. There are a large range of methods for imposing viscoelastic material properties into a mechanical model. For this model we will choose to implement a Kelvin-Voigt model. The Kelvin-Voigt model is the simplest of all viscoelastic solid models, while it lacks some of the necessary oscillatory response behavior that is present in more complected models it should be sufficiently accurate to capture dissipative properties in this dynamic simulation.

Thus to implement the Kelvin-Voigt model the dissipative term in equation 2.87 becomes:

$$\vec{t}_d^{\,i} = \eta_1 Sym(L)\vec{d}^{\,i} \tag{2.100}$$

With η being the viscous dissipation parameters and L the velocity gradient defined by:

$$L = \dot{F}F^{-1} \tag{2.101}$$

2.5 Networking of Beams

To make a foam model, the individual beams described in section 2.3 need to be put into a structure together. In putting the beams together in a structure and then deforming the structure there are two main aspects which need to be added on top of the beam model; how are corners where different beams connect managed, and how to enforce that beams do not overlap one another in the structure as it deforms.

Corners Most of the ligaments in a foam structure join together at their ends. Where two or more ligaments join together will be referred to as a corner. When a corners is present the respective ligaments will be assumed to share the same endpoint. While there will be some overlap in the bodies of the ligaments outside of this point, the only interaction at this corner will be directly though the common endpoint. It is assumed that this point will only sustain one state of deformation, and thus each beam that connects into that point will have the same values for the values of interest (displacement, director displacement, velocity and director velocity).

Using this assumption all of the non-director values can be used directly in the computations for associated beams. However, in defining the current state of a director from its displacement a reference state of the director is required(equation 2.47). At the common point there is not a clear set of reference directors. Thus an approximation for the reference directors is made by assuming that the next set of directors along the beam of interest is the same as the corner node.

For example, referencing figure 2.3, the corner will have a current value of director $\vec{d}_1$ of $\vec{\delta}_1 + \vec{D}_1(Blue)$ when evaluating the blue beam, and a value of $\vec{\delta}_1 + \vec{D}_1(Green)$ when evaluating the green beam. While this approximation of the behavior at the corners is restrictive, it should be noted that the beams emerging from the corner will experience changes in the relative alignments of the cross-sections and the curve's tangent vectors. The tangent vectors will move relative to each other because it is defined with a set of nodes and those nodes are not restricted by the corner. The cross-section alignment will change because

$$\frac{\vec{a}\cdot\vec{b}}{|\vec{a}||\vec{b}|} \neq \frac{(\vec{a}+\vec{\delta})\cdot(\vec{b}+\vec{\delta})}{|\vec{a}+\vec{\delta}||\vec{b}+\vec{\delta}|}. \tag{2.102}$$

See appendix A for proof of statement 2.102.

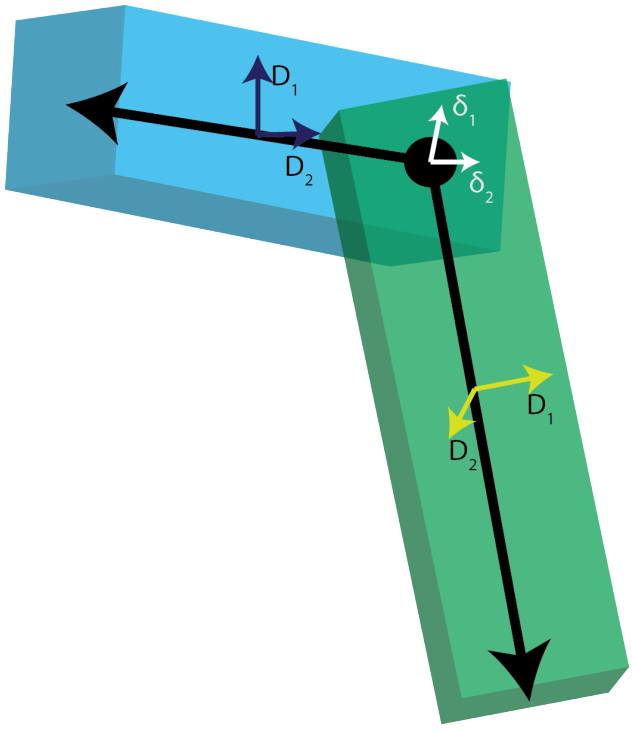

Figure 2.3: Illustration of two ligaments sharing a common corner.

Non-overlapping Beams With the current set of physical equations listed, and the corner linkages of beams defined, the system of beams has no way of knowing what position other beams are in (other than the information passed though the common corner points). Thus it is possible for two beams to overlap. In order to prevent this a non-overlapping constraint will be applied to the system. Thus if a beam detects that it is overlapping with another beam a corrective force will be applied to separate the beams. More details of this contact procedure are covered in section 3.2.

2.6 Summary of Model

In this chapter the key parts of the model used to represent the foam microstructure were presented. An open-celled foam microstructure can be seen as a network of solid ligaments. The model assumes the network of ligaments can be represented as a network of beams. Green-Naghdi beam theory was chosen to represent the non-linear beams. The beams are assembled in to a network by sharing endpoints. The shared endpoints tie the displacement and velocity values of associated beams together, thus providing a means for one beams motion to affect an other. When the beam network undergoes a large amount of deformation, the beams will be prevented from overlapping with one another by contact forces.

Chapter 3

Finite Element Implementation

In chapter 2, the equations describing the beam network were detailed. The result is a series of partial differential equations that need to solved. The finite element method provides a means to translate partial differential equations that exist on moving physical body into a form that can be systematically evaluated and solved by a computer.

The governing equations have derivatives in both space and time. What will be done in the following section is to apply the standard Galerkin finite element techniques to transform the partial differential equations to a series of ordinary differential equations with respect to time, and then integrate these equations forward in time.

This chapter will go over the transformation of the conservation of linear momentum and director momentum into their weak forms, then discuss the choices of shape function to use because at different speeds of deformation different shape functions become more attractive than others. Then the method by which the finite element problem is integrated in time is discussed, followed by how contact/the non-overlapping constraint is applied. Then the chapter finishes with a discussion of issues encountered with the rapid compression problem and their proposed solutions.

The presented methods were implemented using the C programming language and the Portable, Extensible Toolkit for Scientific Computation(PETSc)[3, 2]. C is a complied language which allows for efficient execution of large scale problems where a significant number of loops are required. PETSc was chosen to help in the development of the code because of the framework it has to access sparse linear algebra solvers, control and manage unstructured geometries, and has a framework for developing MPI parallel codes. The code used in this research was written for a serial computer, but could be readily adapted for parallel execution, this was out of the scope for this work.

3.1 Finite Element Formulation

The finite element method consists of transforming a differential equation into the solution of a potential equation. In solving this problem one obtains the parameters to a series of

functions that they can evaluate to obtain an approximate solution to their problem. This involves five general steps [95].

1. Multiplication by a test function
2. Converting the strong from of the differential equation into the weak form.
3. Selection of shape functions for function approximation
4. Application of boundary conditions
5. Solving the system.

Multiplication by a Test Function

The first step of the finite element process is to take an inner product of the differential equation with a generic test function to transform a three dimensional problem into a scalar one. The balances of linear momentum and director momentum are both vector valued functions, therefore each equation needs to have its inner product taken with with its own test function. A general test function is defined as a function with the same domain as the governing equation, is of zero value on fixed boundaries, and is capable of being an arbitrary value everywhere else.

The balances of linear and director momentum will now be multiplied by their appropriate test functions, $\vec{\nu}$ and $\vec{\omega}^{\alpha}$ respectively. It is taken that $y^{\alpha} = 0$,because it is assumed that the 'center' of the cross-section is set at the centroid. This can be done without loss of generality [63]. This assumption is also very important because it allows for the changes in the curves velocity to become separated from the changes in the director velocity.

Linear Momentum

The balance of linear momentum from chapter 2:

$$m\frac{d\vec{v}}{dt} + my^{\alpha}\frac{d\vec{w}_{\alpha}}{dt} = m\vec{b}_b + m\vec{b}_c + \vec{t}^{3}_{,3} \tag{3.1}$$

Applying the cross-sectional origin at the centroid to equation 3.1 gives:

$$m\frac{d\vec{v}}{dt} = m\vec{b}_b + m\vec{b}_c + \vec{t}^{3}_{,3} \tag{3.2}$$

Taking the inner product of the vector differential equation with the test function.

$$m\frac{d\vec{v}}{dt} \cdot \vec{\nu} = m(\vec{b}_b + \vec{b}_c) \cdot \vec{\nu} + \vec{t}^{3}_{,3} \cdot \vec{\nu} \tag{3.3}$$

Director Momentum

The balance of director momentum from chapter 2:

$$my^{\alpha}\frac{d\vec{v}}{dt} + my^{\alpha\beta}\frac{d\vec{w}_{\beta}}{dt} = m(\vec{b}_b^{\alpha} + \vec{b}_c^{\alpha}) - \vec{t}^{\alpha} + \frac{\partial \vec{m}^{\alpha}}{\partial \theta^3} \tag{3.4}$$

Applying the cross-sectional origin at the centroid to equation 3.4 gives:

$$my^{\alpha\beta}\frac{d\vec{w}_{\beta}}{dt} = m(\vec{b}_b^{\alpha} + \vec{b}_c^{\alpha}) - \vec{t}^{\alpha} + \frac{\partial \vec{m}^{\alpha}}{\partial \theta^3} \tag{3.5}$$

Taking the inner product of the vector differential equation with the test function.

$$my^{\alpha\beta}\frac{d\vec{w}_{\beta}}{dt}\cdot\omega^{\alpha} = m(\vec{b}_b^{\alpha} + \vec{b}_c^{\alpha})\cdot\omega^{\alpha} - \vec{t}^{\alpha}\cdot\omega^{\alpha} + \frac{\partial \vec{m}^{\alpha}}{\partial \theta^3}\cdot\omega^{\alpha} \tag{3.6}$$

Transformation to the Weak Form

The goal of transforming equations 3.3 and 3.6 in to the weak from is to allow for the enforcement of the differential equation to be carried out as an integral effect over the domain of the problem, and to reduce the differentiability requirements for the proposed test and approximate functions.

To transform the problems in to the weak form equations 3.3 and 3.6 are integrated over the domain of the problem(the body), and then divergence theorem is used. The result of the divergence theorem reduces the level of differentiation required in the problem and to provides a term in which surface tractions can be introduced into the problem directly. The following is this process applied to the equations of interest.

Linear Momentum

Integrate equation 3.3 over the body:

$$\int_L \rho\frac{d\vec{v}}{dt}\cdot\vec{\nu}ds = \int_L m(\vec{b}_b + \vec{b}_c)\cdot\vec{\nu}ds + \int_L \vec{t}^{\,3}_{,3}\cdot\vec{\nu}ds \tag{3.7}$$

Use the divergence theorem (or in one dimension integrate-by-parts) to lessen the differentiability requirements:

$$\int_L \rho\frac{d\vec{v}}{dt}\cdot\vec{\nu}ds = \int_L m(\vec{b}_b + \vec{b}_c)\cdot\vec{\nu}ds + \int_L (\vec{t}^{\,3}\cdot\vec{\nu})_{,3} - \vec{t}^{\,3}\cdot\vec{\nu}_{,3}ds \tag{3.8}$$

$$\int_L \rho\frac{d\vec{v}}{dt}\cdot\vec{\nu}ds = \int_L m(\vec{b}_b + \vec{b}_c)\cdot\vec{\nu}ds - \int_L \vec{t}^{\,3}\cdot\vec{\nu}_{,3}ds + \left[\vec{t}^{\,3}\cdot\vec{\nu}\right]_1^2 \tag{3.9}$$

Director Momentum

Integrate equation 3.6 over the body:

$$\int_L \rho y^{\alpha\beta} \frac{d\vec{w}_\beta}{dt} \cdot \vec{\omega}_\alpha ds = \int_L \rho(\vec{b}_b^\alpha + \vec{b}_c^\alpha) \cdot \vec{\omega}_\alpha - \vec{t}^\alpha \cdot \vec{\omega}_\alpha ds + \int_L \frac{\partial \vec{m}^\alpha}{\partial \theta^3} \cdot \vec{\omega}_\alpha ds \tag{3.10}$$

Use the divergence theorem (or in one dimension integrate-by-parts) to lessen the differentiability requirements:

$$\int_L \rho y^{\alpha\beta} \frac{d\vec{w}_\beta}{dt} \cdot \vec{\omega}_\alpha ds = \int_L \rho(\vec{b}_b^\alpha + \vec{b}_c^\alpha) \cdot \vec{\omega}_\alpha - \vec{t}^\alpha \cdot \vec{\omega}_\alpha ds + \int_L (\vec{m}^\alpha \cdot \vec{\omega}_\alpha)_{,3} - \vec{m}^\alpha \cdot \vec{\omega}_{\alpha,3} ds \tag{3.11}$$

$$\int_L \rho y^{\alpha\beta} \frac{d\vec{w}_\beta}{dt} \cdot \vec{\omega}_\alpha ds = \int_L \rho(\vec{b}_b^\alpha + \vec{b}_c^\alpha) \cdot \vec{\omega}_\alpha - \vec{t}^\alpha \cdot \vec{\omega}_\alpha ds - \int_L \vec{m}^\alpha \cdot \vec{\omega}_{\alpha,3} ds + [\vec{m}^\alpha \cdot \vec{\omega}_\alpha]_1^2 \tag{3.12}$$

Shape Functions Selection

Currently in the governing equations that have just been transformed, no approximations to the form of the solution have been made. The current form of the problem requires solving the equations at all points in space. This is an intractable problem. To lessen this requirement, approximations to the form of the fields of interest. It will be assumed that the fields can be additively decomposed in to a series of prescribed scalar functions that are scaled by unknown factor. With this assumption the form of the problem shifts from solving for a function to solving for a set of constants. These prescribed functions are called shape functions. If there are N shape functions the form of the values of interest and the test functions take the from of:

$$\vec{u}(x;t) = \sum_{i=1}^{N} \phi_i(\vec{x}) \vec{u}_{it} \qquad \vec{v}(x;t) = \sum_{i=1}^{N} \phi_i(\vec{x}) \vec{v}it \tag{3.13}$$

$$\vec{\nu}(x;t) = \sum_{j=1}^{N} \psi_j(\vec{x}) \vec{\nu}_{jt} \tag{3.14}$$

The same representation applies for the director based terms. $\vec{u}_{it}$, $\vec{v}_{jt}$ are the scaling values of the curve displacement and velocity for the i'th shape function at time t. ϕ_i and ψ_j are the respective scalar shape functions. As a conventional practice the shape functions are chosen to be one at a single point in space and to be zero at other points in space. These designated points in space are referred to as nodes. Thus when this convention is used $\vec{u}_{it}$ and $\vec{v}_{jt}$ have the interpretation of being the displacement/velocity at their node in space. ϕ and ψ do not need to be different functions and in the approach used in this work, the

Galerkin form is used where $\phi_i(x) \equiv \psi_i(x)$. In equations 3.9 and 3.12 substituting in the shape function approximation yields a product in the form of:

$$\sum_{i=1}^{N} \dot{\vec{v}}_{it}\phi_i(\vec{x}) \sum_{j=1}^{N} \vec{\nu}_{jt}\phi_j(\vec{x}) \tag{3.15}$$

The $\vec{\nu}_{jt}$ term can be factored out of equation 3.15 because of the linearity, and then the term can be dropped because it can be factored out of all the terms in equations 3.9 and 3.12. Factoring out $\dot{\vec{v}}$ from equation 3.15 gives:

$$\left[\sum_{i=1}^{N} \phi_i(\vec{x}) \sum_{j=1}^{N} \phi_j(\vec{x})\right] \dot{\vec{v}}_{it} \tag{3.16}$$

In equation 3.16 all the shape functions need to be multiplied by all the other shape functions. This term, and other terms like it, couple all of the shape functions together. This coupling would require a large amount of computational effort. To reduce this effort the shape functions are defined to be non-zero only between a small set of nodes. This definition eliminates the direct coupling between distant shape functions/nodes.

While Green-Naghdi beams are three dimensional objects, their governing equations are parameterized in one dimension, the beam's arc length. Nodes are then defined along the arc length of each beam with beams forming corners sharing a node. Then one dimensional shape functions connect a set of nearby nodes along the length of each beam. A particular set of nodes connected by shape functions is referred to as an element. Between elements it will be formulated such that within the domain there is C^0 continuity, in that the values of the function will be continuous within and between elements, however the derivatives between the elements will not be continuous. Formulations of finite elements exist with lower and higher degrees of continuity, but require special treatments. In figure 3.1 a linear element and a quadratic element are plotted.

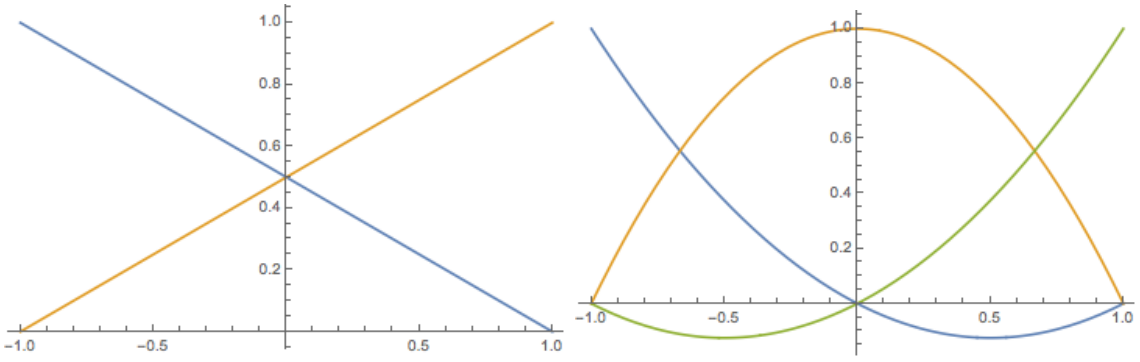

Figure 3.1: Plots of one parameter shape functions in an ideal configuration.(Left) Linear shape functions used to connect adjacent nodes. (Right) Quadratic shape functions used to connect a series of three nodes at -1,0, and 1. While the nodes at the edge of these plots will connect to other nodes, the node in the center will only connect with the pictured nodes.

The selection of which shape function to use is a case by case decision. In general, more complicated shape functions, such as higher order polynomials, can be more accurate and can avoid being overly restrictive as more simple shape functions may be. Gong et al. in their studies used quadratic shape functions [32]. The quadratic shape function is attractive for use in beams because of the added flexibility in the element and that some of the solutions to the linear beam bending equations are quadratic in nature. Thus using quadratic shape functions could capture the bending behavior better and allow one to be more computationally efficient.

However, in the rapid crushing of a beam it may be possible for some nodes to deform greatly while other nodes in the same element are not perturbed. This disparity of deformation,when using quadratic shape functions, can lead to difficulties because it will produce unphysical results in the governing equations. For example, the case where a beam is being axially compressed and the nodes have deformed in such a manner to mimic the case presented in figure 3.2, the element could invert its volume. To demonstrate this inversion, assume a linear elastic material to calculate the integral of $\vec{t}^3 \cdot \vec{\nu}_{,3}$ from equation 3.9 with the shape function approximation can be written as:

$$\int J_c^{-1}(\zeta)\phi_1(\zeta)'\mathbb{E}\sum_{i=1}^{3}\phi_i(\zeta)'u_i d\zeta \tag{3.17}$$

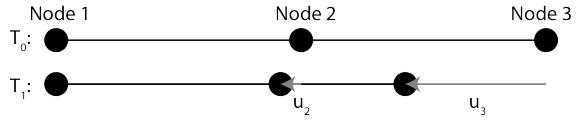

Figure 3.2: Set up for rapid quadratic element crushing, Where at some time T_1 node 3 has deformed a large amount and node 2 has deformed to a lesser amount, with respective displacements u_3 and u_2, while node 1 has not deformed at all.

In this integral there is a a Jacobian, J_c, which maps the change in volume from the computational configuration to the spatial configuration. Physically $J > 0$, thus if the value of the Jacobian leaves the admissible range then any values derived form it are erroneous. A test was set up with the nodes, in ascending order, located at points -1,0, and 1, then the J_c was calculated for various combinations of u_2 and u_3, these results were plotted in figure 3.3. From figure 3.3 it can be seen that this inversion can occur for many values of u_2 and u_3.

With this in mind for rapid compression tests, where there is the change for dramatic variation in the displacements of nodes within an element, it is necessary to use shape functions that are more robust than quadratics. The same test of inversion we preformed using linear shape functions. A Linear element only contains two nodes, thus node 1 was held fixed at -1 and node 2 was given a compressive displacement u_2 away from its starting position 1. Looking the results in figure 3.4, it can be observed that the Jacobian can only

invert if the nodes pass though each other. Thus the linear shape function can withstand a larger amount of nodal deformation variation than the quadratic elements. This advantage of linear element makes them a better choice at high rates of deformation, while quadratic shape functions are more desirable at lower rates of deformation because they can be more accurate and the difficulties opposing them are minimized.

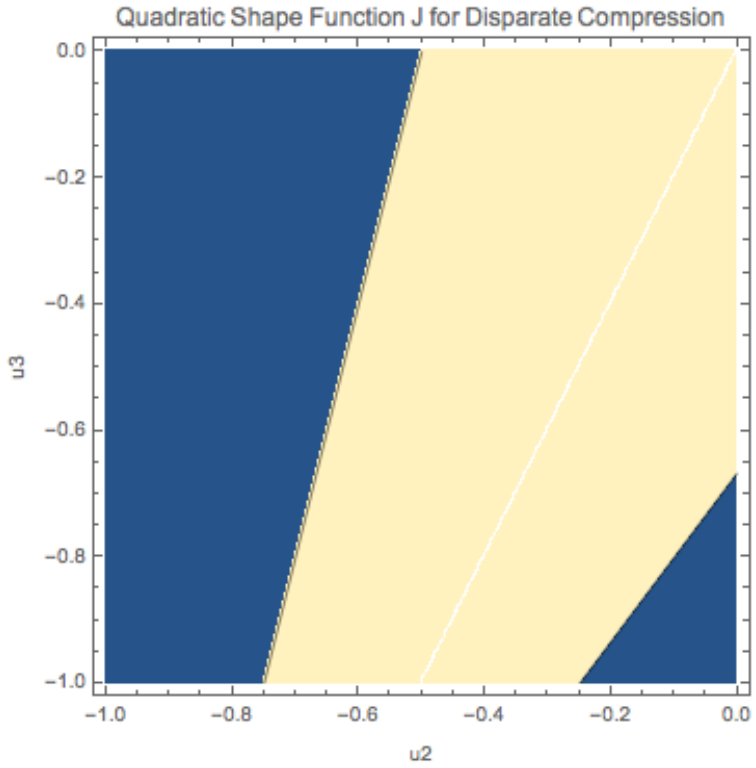

Figure 3.3: Plot of the minimum J_c for the uneven deformation problem using quadratic shape functions. Dark regions indicate J_c values of zero or less. $J_c = \sum_{i=1}^{3}(X_i + u_i)\phi'(\zeta)$

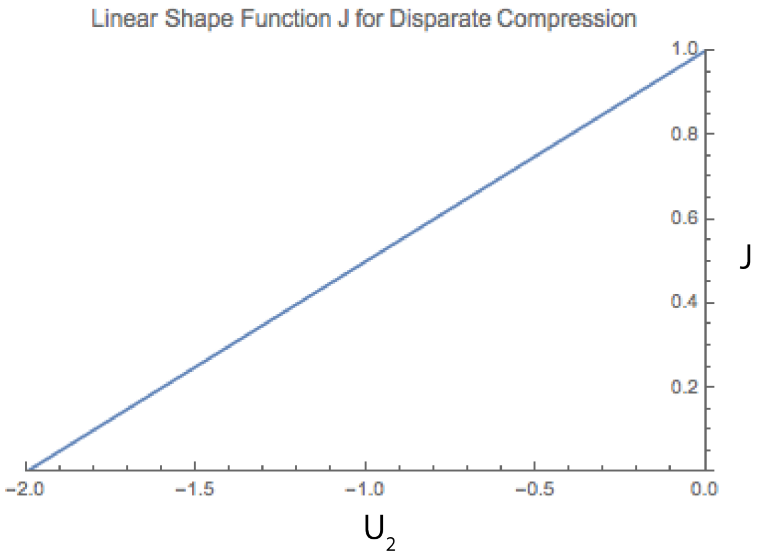

Figure 3.4: Plot of the minimum J_c for the uneven deformation problem using linear elements. The J_c only reaches a value of zero when the two nodes pass each other. $J_c = \sum_{i=1}^{2}(X_i + u_i)\phi'(\zeta)$

In the authors experience, quadratic elements begin to become a problem when the driving deformation speed within the beam approach the compressive wave speed within the beam, typically when the driving speed is greater than a tenth of the compressive wave speed.

Boundary Conditions & Time Integration

By applying the choice of shape functions to the weak form of the governing equations (quadratic for slow and linear for fast), the weak from can now be rewritten into the following from:

$$\mathbb{M}\dot{\vec{a}}(t) = \mathbb{F}(\vec{a}(t), t) \tag{3.18}$$

where $\vec{a}$ is the concatenation of all of the desired unknowns $(\vec{u}, \vec{v}, \vec{\delta}_\alpha, \vec{w}_\alpha)$, $\mathbb{M}$ is an inertial matrix, and $\mathbb{F}$ is a vector that describes the general forces that act to change $\vec{a}$. The partial differential equation is now an ordinary differential equation in terns of time. To solve this problem, boundary conditions need to be applied and then the equation needs to be integrated in time.

Fixed or Dirichlet type boundary conditions are enforced by directly altering the inertial matrix by replacing a row with all zeros except with a one in the diagonal location, and then replacing the respective terms with the forcing function with the fixed value. Traction or Neumann type boundary conditions are applied by directly applying the traction into the forcing function. Wall type boundaries will be applied to many of the beam network simulations, these are treated like a special case of the contact condition, and will resemble

a mixed boundary condition, where a traction is specified based off the values of the fields of interest. More detail about this is provided in section 3.2.

Time Integration

To see the response of the structure as it proceeds to deform, an initial state for $\vec{a}$ is prescribed and then solving equation 3.18 for $\dot{\vec{a}}$, $\vec{a}$ can be updated to a new state at a later time. Explicit time integration was chosen as the preferred method for evolving equation 3.18 in time. Explicit time integration was chosen because of the short time scales of the physical events involved and because of the presence of contact. Explicit methods only require knowledge of the current and/or previous time steps, as opposed to implicit methods that require the solution of a (typically) non-linear problem to find the values of a problem at a future time step.

Implicit methods offer greater numerical stability but more work is required to solve for an individual step. To solve an implicit problem, a method similar to Newton-Raphson is employed. In these types of solvers a tangent matrix is required. A tangent matrix will relate all nodes that have any form of interaction with one another to a value in a matrix. This means that in addition to the fixed set of interactions that are present from the internal beam relations, beam elements that come in contact with one another will also need to be represented in the tangent matrix. This means that as elements come in and out of contact with one another there is changing sparsity in the structure of the tangent matrix. Managing this change can be costly. In addition, the calculating the entries for and solving the tangent matrix may make every time-step very costly, outside of the data management.

The issues with the tangent matrix due to contact are avoided by using explicit integration. However, smaller time steps must be taken due to the reduction in stability of explicit methods [49], and more strict conditions required to meet the Courant-Friedrichs-Lewy(CFL) condition. This makes explicit methods only suitable for simulations over short time scales, which is appropriate for the rapid crush experiments of interest in this research.

The choice of explicit integration scheme used is Runge-Kutta Four (RK4). For each time step, four sub-time steps are taken. With the results of each sub-time step combined to give the position at the new time step. Each sub-step has the form:

$$\vec{a}(t + c_i\Delta t) = \vec{a}(t) + k_{ij}\Delta t\dot{\vec{a}}(t + c_j\Delta t) \tag{3.19}$$

where k_{ij} is a lower triangular matrix of constants,and c_i is the different positions of the sub-time steps. With the combination of the sub-time steps given by:

$$\vec{a}(t + \Delta t) = \vec{a}(t) + b_i\Delta t\dot{\vec{a}}(t + c_j\Delta t) \tag{3.20}$$

where the new term b_i represents the component of a constant vector when summing the effects of the different changes in values $\dot{\vec{a}}(t + c_j\Delta t)$. This method is desirable because of the increase in the stability region that the method provides over cheaper methods such as forward Euler. In particular, RK4 provides stability for oscillatory motions, which is

a common feature in solid dynamics [49]. In addition, for implementation RK4 does not require explicitly storing all interim results making the method less memory costly.

Lumped Mass Matrix In each time step of RK4 it is necessary to obtain $\dot{\vec{a}}$. This is done by the solving a linear system of equations:

$$\dot{\vec{a}} = \mathbb{M}^{-1}\mathbb{F} \tag{3.21}$$

The matrix, $\mathbb{M}$, is sparse and the most significant values are along the diagonal of the matrix, and because of the need to solve equation 3.21 so very often it is beneficial to use a lumped mass matrix instead of the full matrix. Lumped mass matrices are discussed in Zienkiewicz and Taylor [94] as a means to reduce the computational cost for inverting the mass matrix, as well as improving some of the results for wave propagation though a material. A lumped mass matrix $\mathbb{M}_L$ collapses the full mass matrix to a diagonal matrix (essentially a vector).Using $\mathbb{M}_L$ in equation 3.21 reduces the solve to a series of scalar divisions. This dramatically reduces the complexity and cost of the solve, guaranteeing a linear increase in the cost of a solve with the number of nodes in the problem, which is better than the scaling of any solution technique for a non-diagonal matrix can guarantee[19].

There are various methods to condense a matrix into its lumped form: use of piecewise constant shape functions in the mass integral, summing the row entries, dropping all non-diagonal terms and scaling the remaining terms to preserve mass, and use of numerical integration centered at the nodes, amongst other methods. In this work, the lumped mass matrix is formed using the row sum method:

$$\mathbb{M}_{Lik} = \left\{ \begin{array}{ll} i = k & \sum_{j=1}^{N} \mathbb{M}_{ij} \\ i \neq k & 0 \end{array} \right\} \tag{3.22}$$

The row sum method was chosen because in its formulation it meets the integration requirements discussed by [37], and its performance has been noted not to degrade the accuracy of the solution by a substantial degree [20].

3.2 Contact

Overview

Introducing contact into a simulation adds great computational cost and complexity to the simulation. Contact, in the context of this work, is a physical event that enforces the non-overlapping constraint. Thus at times in the simulation contact may play no roll (when all surfaces are spread away from one another), or be the fundamental physical phenomena driving behavior, as in a particle packing simulation.

In terms computational cost, contact is expensive. Non-contact finite element simulations have fixed local interactions and therefore have fixed computations and dependencies on

variables. When contact is involved, the computations and dependencies of an element are tied to other elements, and the dependencies may change as the elements move relative to one another. In other words in non-contact finite element codes, an element only needs to know the values of fields contained within the nodes it is defined on. Thus, very little information (relative to all of the information in the problem) needs to be processed to perform a calculation. However, Once contact is introduced, elements that can experience contact may depend upon field information of all other surfaces, thus necessitating the processing of more information within an element.

In conventional three dimensional finite elements, the only elements that can experience contact are those that share a surface with the boundary of a body. For rod and beam elements, the surface and interior of the beam is abstracted into a singular structure, thus the rod itself is both an interior and surface element. Therefore, when contact is introduced all rod elements need to process non-local information in order to determine their behavior[87, 84].

Aspects of Contact

The contact problem can be broken into three main sections:

1. Spatial Sorting: Organizing the data such that it is known which pieces of data are close enough to possibly interact.

2. Contact Search: Looking in detail at the local clusters to see if there are any points which need to have contact enforced upon them.

3. Contact Physics: Applying the physics chosen in a model to enforce the desired contact condition

Spatial Sorting

The computational complexity of checking for the contact between N different objects is of the order $O(N^2)$, meaning that if one doubles the size of the problem, they in turn quadruple the work requirements in order to check to see if contact occurs among the objects. Contact can be thought of as a short-range limit to a more general class of pairwise interactions between objects. There are many techniques developed to improve the complexity scaling. Of note is the Fast Multipole Method (FMM) developed by Greengard and Rokhlin, where by sorting the objects in space and lumping the behavior of far away objects into a collective interaction reduces the order of complexity to $O(N)$ [36].

Because contact has a very short domain of interaction in comparison to the types of problems handled by Greengard and Rokhlin, FMM is not an appropriate sorting method. Like FMM We will sort the objects in space, and then limit our interaction checks to a local region thus improving the scaling performance. For contact applications a variety of sorting methods exist as discussed in [84]. One of the most common sorting methods is binning. In a

binning sort, the global space of the problem is divided into smaller sections of subspace(the bins) and the different objects are placed in those bins. The adjacency of all the bins is known. Thus, when a contact search needs to occur the search only occurs over the particles in the bin and the neighboring bins. The bins can be static or change in size and location though the course of the simulation, like the octree method[57].

A static regular bin sorting method was chosen. As the problem evolves elements can become sparse in regions and clustered in others, thereby reducing the effectiveness of the sort, as illustrated in figure 3.5. In the simulations performed with this work, the clustering of elements in a few bins will occur, however the worst of this should only occur at the end of the simulation, allowing most the simulation to run efficiently.

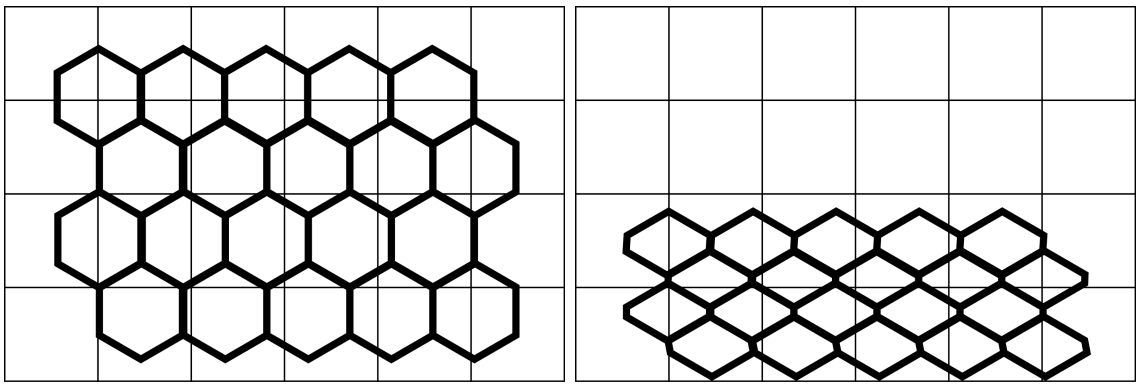

Figure 3.5: (Left) Evenly distributed objects though out the domain lead to the best scaling performance. (Right) A later stage in a simulation where the objects have congregated in a subset of the bins, reducing the efficiency of the calculations.

When binning, it is advantageous to use the smallest sized bins possible because the total amount of work done in the contact search is on the order of $N_b n^2$, where N_b is the number of bins, and n is the largest number of objects in one bin sub-cluster. With smaller bins the squared scaling will play less of a role which is desirable, but if the bins are made too small contact may be missed. To ensure that all relevant contact is found the smallest dimension for the bin must be larger than the largest dimension of a beam element, either the length or radius of the element. For a given ligament the number of elements present is between five and ten. In using this number of elements per ligament, this limits the size of the bin to at least one-tenth the length of the longest ligament.

Binning of a Elements Binning needs to occur at the beginning of the simulation and then again once enough time has passed in the simulation such that an object may have moved the length of one bin in order to not miss any potential contact checks. A beam element may exist within multiple bins, thus it is necessary to identify a single location to characterize the element's position in space. To characterize the element's position the

centroid of the element's nodes was chosen.

$$\vec{x}_c = \frac{1}{N}\sum_{e=1}^{N}\sum_{i=1}^{3}(X^{ei} + u^{ei})\vec{E}_i \tag{3.23}$$

The centroid is fast to calculate and with the restrictions on minimum bin size missed contact checks from it are not possible.

Contact Search

In the determination of the forces applied to an object through contact, it is necessary to do an $O(n^2)$ search though all of the objects in the bin the object is in and the objects in the surrounding bins, where n is the count of objects in the subset of bins. If the bin sizes are selected correctly $n << N$ the squared scaling should have minimal impact. The contact check for beam and rod elements is like a hybrid of contact checks used in particle codes and fully dimensional finite elements codes. For particles, the objects are chosen typically represented as spheres, hyper ellipsoids or compositions of the two[63]. Spheres and compositions of spheres are particularly popular because of the ease of the contact check:

$$l^2 = (\vec{x_2} - \vec{x_1}) \cdot (\vec{x_2} - \vec{x_1})$$

$$g = \left\{ \begin{array}{cc} 0 & l^2 \geq (R_1 + R_2)^2 \\ (R_1 + R_2)^2 - l^2 & l^2 < (R_1 + R_2)^2 \end{array} \right\}$$

where l is the square of the distance between the centers of two spheres, and g the overlap measure, known as the gap function. If g is less than zero then the contact constraint is applied to the objects.

In a finite element application, contact detection is typically done by doing a penetration check for each of the nodes against the surface of the opposing face[86]. For linear elements, the problem involves determining the plane of the surface elements and then determining which side of the plane the nodes are. If the node does penetrate the surface, the penetration distance is determined to be the normal depth of penetration. An illustration of both of these methods is given in figure 3.6.

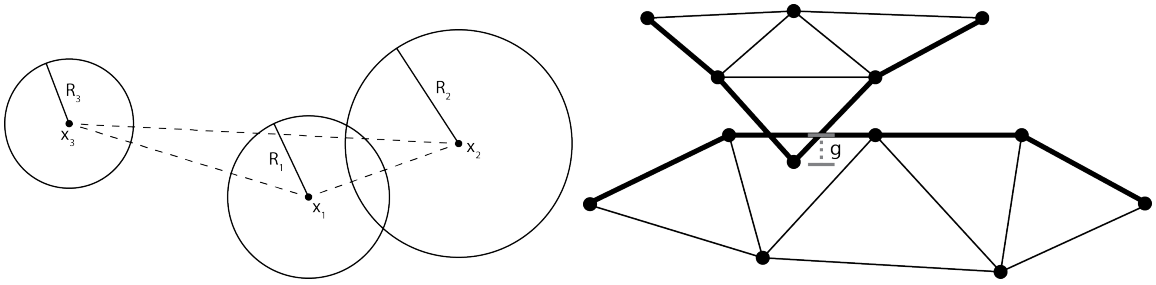

Figure 3.6: (Left) The contact check between two spheres. (Right) The penetration check used in linear two dimensional finite elements

$$\vec{d} = \vec{x} - \vec{x}_0$$

$$g = \left\{ \begin{array}{cc} 0 & \vec{d} \cdot \vec{n} \geq 0 \\ -\vec{d} \cdot \vec{n} & \vec{d} \cdot \vec{n} < 0 \end{array} \right\}$$

Where $\vec{x}_0$ is the anchor point of the plane and n is the normal for the plane, going out of the body.

The proposal to determine all points of contact between two ligament structures is not a trivial one, especially if one does not have a circular cross-section, see [52] for more details for handling non-circular cross-sections. Approximating the cross-section of the beams to be circular for contact purposes can allow the use of a method similar to that of the particle methods discussed before as opposed to the more computationally complex methods.

Finding The Gap Function for Ligaments When ligaments are near each other, it is possible for the ligaments to be in contact throughout their whole lengths, or for only subsections to be in contact. In both of these cases it is necessary to determine what parts of each ligament are in contact. As proposed in [67] it is assumed that the points in contact between two beam elements are the points that minimize the distance between them. This creates a mapping of closest points from one element to the other. This mapping will be used to determine the amount of contact force applied, and where the force is applied in the ligament. When searching for the nearest point on an opposing element one is minimizing the distance between them, as illustrated in figure 3.7.

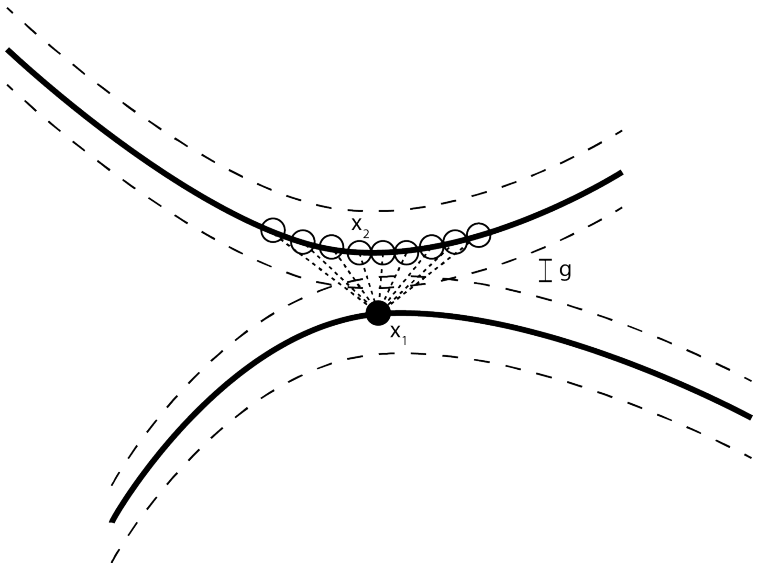

Figure 3.7: Contact check for beam finite elements

$$l^2 = \min_{x_2} \{(\vec{x_2} - \vec{x_1}) \cdot (\vec{x_2} - \vec{x_1})\} \tag{3.24}$$

In equation 3.24 it states that the corresponding potential contact point for point x_1 within ligament 1 is the point x_2 within ligament 2 that minimized the square of the 2-norm of their distance. (This will yield the same results if just the 2-norm were used). Finding the minimum distance from a three dimensional curve to an arbitrary point in space is in general a nonlinear minimization problem. In the application to finite elements, the problem can be simplified greatly, because the ligaments are comprised of individual elements. Each element is represented by a polynomial shape functions. Thus reducing the general problem, to one of minimizing the distance between a point and a polynomial curve.

To find the true distance minimizer, the following form exists to measure the square of the 2-norm.

$$\sum_{i=1}^{p} \vec{x^i}\phi^i(s) - \vec{x_1} = \vec{d} \tag{3.25}$$

$$l^2 = \vec{d} \cdot \vec{d} = \sum_{j=1}^{p}\sum_{i=1}^{p} \vec{x^j} \cdot \vec{x^i}\phi^i(s)\phi^j(s) - 2\sum_{i=1}^{p} \vec{x^i} \cdot \vec{x_1}\phi^i(s) + \vec{x_1} \cdot \vec{x_1}$$

A minimum will exist at the extremes of of the arc length of the element, s, or where there is a zero derivative of l^2. Thus to find this point, the following zeros must be found:

$$\frac{\partial(l^2)}{\partial s} = 2\sum_{j=1}^{p}\sum_{i=1}^{p} \vec{x^j} \cdot \vec{x^i}\frac{\partial\phi^i(s)}{\partial s}\phi^j(s) - 2\sum_{i=1}^{p} \vec{x^i} \cdot \vec{x_1}\frac{\partial\phi^i(s)}{\partial s} = 0 \tag{3.26}$$

While it is possible to search the space for these points and find the solutions using Newtons method, for computational efficacy such a calculation can be costly because of how often these values need to be found, and the need to keep recalculating shape function derivatives. As an alternative an approximate method is used by minimizing over a limited set of points. In the interests in using data that is easily available and relevant, the Gauss points and nodal points are the points chosen to determine if contact occurs.

By using the gauss points and nodal values, there is no need to compute additional shape function values outside of the values determined for the initial element already. This recycling of data is due to the fact that the values of the shape function do not change as the shape of the element changes, only the derivatives do. In this discreet case it needs to be ensured that the investigation points are close enough together as such to not allow a gap to form where contacting beams may pass though one another. An approximation for the minimum number of elements required for a ligament and its aspect ratio can be found in the appendix, with equation B.7. The number of elements required changes for the number of gauss points used and the aspect ratio of the beams.

In figures 3.8, and 3.9 the number of elements required for at most a one percent error to occur in contact detection with various numbers of Gauss points and aspect ratios are plotted. The results are plotted on a log scale.

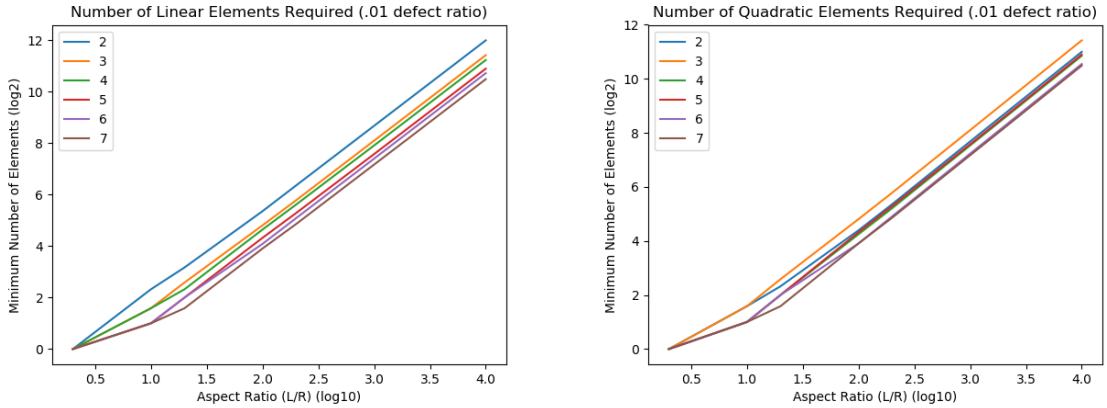

Figure 3.8: The number of elements needed per ligament if there is going to only be a one percent error in the contact detection. The different lines represent the different number of gauss points used. It can be seen that as the aspect ratios increase the higher gauss points methods require less elements.

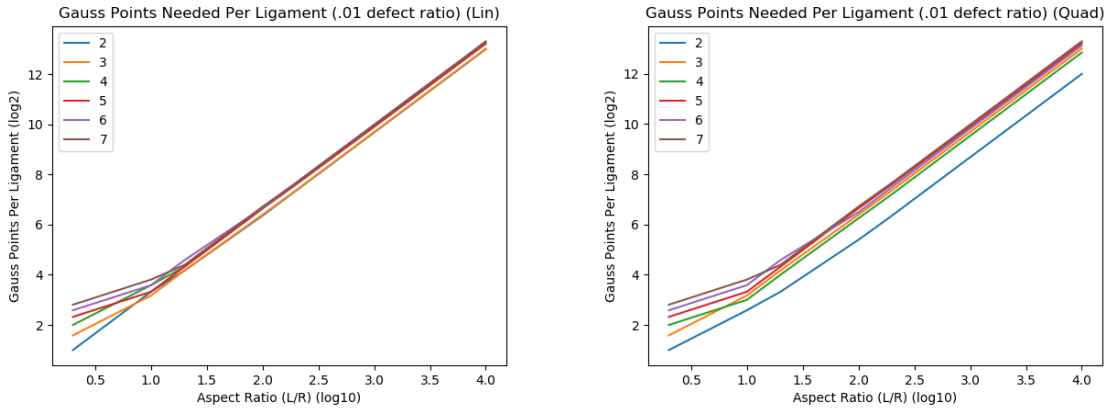

Figure 3.9: Plot of the total number of gauss points used to ensure at most a one percent error in contact detection. Other then the lowest of aspect ratios the total number of Gauss points needed for a numerical integration scheme is virtually the same, with one noticeable exception being the two point integration in the quadratic element. However this scheme can not fully integrate the quadratic shape functions.

From figures 3.8, and 3.9 it can be seen that at lower aspect ratios less low Gauss point schemes can be used and still impose the contact condition. This is important because using more gauss points only serves to enforce the contact detection, and does not improve the accuracy of the integrations in the element. Thus, keeping the total number of gauss points to a minimum is important for performance. It is also worth noting that the most noticeable differences are in the lower number of gauss points and lower aspect ratios.

Using the scans of the Zorbium form used in the Team Wendy pads. it appears that there is a mean aspect ratio of around 10, but there appears to be a wide amount of variation. Thus it can be seen that low numbers of gauss points and lower numbers of elements (less than 10) can be used in each ligament without concern for loss of contact.

This formulation works well when the ligaments have a one-to-one correspondence of the mapping of closest points. For every point investigated there will only ever be at most one contact point from another ligament. In general this is not a physical restriction, but rather a restriction imposed by the model. It is possible that if one ligament were to be draped over the other ligament in a "U" like shape, there would be several points from the "U" ligament in contact with a single point along the supporting ligament. In these cases there may be stability issues as the various points that should be in contact take turns in different time steps being the closest point.

The overall flow of the contact detection goes as follows:

1. Within the internal forces calculations for an element, identify the bin the element currently resides in.
2. Identify which ligaments may come into contact with the element, by looking as the lists of ligaments in the current and adjacent bins.
3. Loop though all elements on all relevant ligaments
4. Within each element find the point which minimized the distance from the gauss point/node of the initial element
5. If the distance is less than the sum of the radii, then contact occurs.

Contact Physics

In the application of contact, two aspects need to be modeled; The contact force enforcing the contact constraint, and how friction is modeled at the contact point.

Contact is the application of a constraint to a model. Thus the traditional techniques to apply constraints to a model, the penalty and Lagrangian multiplier methods, will work in enforcing the contact constraint[86].The finite element method can be reformulated into finding the zeros of the gradient of a potential.

$$\min_{a} \left(\Pi(a)\right) \tag{3.27}$$

Where in equation 3.27 a are the variables of interest and Π is the potential formed from the system. In a purely linear-elastic system:

$$\Pi = \int_{\Omega} \frac{1}{2} \epsilon \cdot \mathbb{E} \epsilon dv \tag{3.28}$$

With ϵ being the linear strains and $\mathbb{E}$ being the tensor of elastic constants. When constraints are applied to the problem the minimization changes such that equation 3.27 is now minimized over the unconstrained potential and another potential applying the constraint.

$$\min_{a,b} \left(\Pi(a) + \Pi_c(a, b) \right) \tag{3.29}$$

Where Π_c is the constraining potential, and b is additional variables required to enforce the desired constraint. The penalty and Lagrangian multiplier methods are specializations of this generalization. For contact the condition what is to be enforced is the non-penetration condition, represented by zeroing the gap function:

$$g = 0$$

The Lagrangian multiplier method applies this by applying an indeterminate constant, the Lagrange multiplier, by the constraint function, and then finding the stationary point of the desired variables and the multipliers. Transforming equation 3.29 into:

$$\underset{a, \lambda_i}{\overset{stat}{}} \left(\Pi(a) + \sum_i \lambda_i g_i(a) \right) \tag{3.30}$$

The minimization transforms into finding the stationary point because the addition of the multiplier turns a convex function into a function that has a saddle point, requiring the use of more complicated solution techniques. Use of the Lagrangian multiplier will enforce the constraint exactly, and the multiplier itself can be interpreted as being the contact force. However, in this formulation there are additional variables added to the problem. These additional variables make the problem larger, and thus more costly to solve. In addition, because the contact constraint can change through the evolution of the problem, how many and where the multipliers need to be applied will change. These additional considerations require the changing of computational data structures, which can be costly.

To avoid the difficulties of the Lagrangian multiplier method, the penalty method is a desirable alternative. The penalty method relaxes the constraint, thus not ensuring that the gap function is zero, but attempting to make the gap function as small as possible. The form of the constraint system potential is:

$$\min_{a} \left(\Pi(a) + \sum_i \frac{1}{2} P g_i(a)^2 \right) \tag{3.31}$$

In equation 3.31 contact is imposed by making the gap function act like a stiff spring, where P is the spring coefficient. This means that there will be some non-zero value of the gap function as long as P remains finite. The choice of P is often done by trial and error on the part of the programmer, higher values of P will apply the constraint better, however too high of values will cause the system to become unstable, and more costly to integrate in time. Accepting some slack in the contact constraint keeps the problem in convex form, and does not require additional variables, or data management. In this form the contact force can be recovered by taking the first variation of the constraint potential in terms of g to get:

$$F_c = Pg(a) \tag{3.32}$$

For the beam network model, it was chosen that the contact constrain be applied via a variation of the penalty method. The penalty method has been adapted to include some dampening effects. In this formulation the penalty term contains an 'elastic' part that depends upon the magnitude of the gap function and a 'viscus' component that is linear with the rate of change of the gap function. In order to avoid over dampening the contact $P_v << P_e$.

$$F_c = P_e g + P_v \dot{g} \tag{3.33}$$

The ramifications of equation 3.33 are that contacts are now dissipative in the material, leading to additional energy loss as the material deforms.

In this model, we will limit the modeling of friction to that of sliding friction, where the fictive force is modeled by a coulomb model [29], in the direction opposing the relative motion of the two points in contact:

$$F_f = -\mu |F_c| \vec{n}_{\parallel} \tag{3.34}$$

Where μ is the friction coefficient, $|F_c|$ is the magnitude of the contact force and $\vec{n}_{\parallel}$ is the relative direction of sliding.This model is a lower fidelity model of many friction models, namely the model neglects the effects of static friction. In future work, the differences in behavior between the different friction models and its effect on this type of network model can be studied but is outside the scope of this study.

Beam-Wall Contact The contact incurred between the beams and the wall is dealt with in a manner similar to the contact between beams and other beams. The only notable change in the contact process is how the overlap condition is tested. In this work only flat walls were used. In these walls a frontward facing normal is defined, as well as a point in the plane. If at any time it is detected that the inner product of the distance vector from the wall's point to the element with the normal vector is negative, then the element is considered to be in contact with the wall, and the penalty method from before is applied.

3.3 Rapid Compression Issues

Release of Compressed Columns

In the axial compression of beams, there is a transformation in the mode of deformation that occurs when the amount of deformation reaches a critical value. Before the critical point the beam will deform along its axis in a compressive mode. After the critical point the beam's deformation does not remain along its axial direction, instead the beam deflects out to the sides. This transition is referred to as buckling. Buckling occurs because the the bending mode of deformation contains less internal energy than the pure axial deformation, after a critical value. The pure axial deformation mode becomes an unstable equilibrium, and any imperfections in the alignment of the beam or variations in the internal stress response will serve as sufficient perturbations to cause the transition from axial compression to bending.

In the compression of a beam network there can be ligaments that experience large levels of axial compression. Because of the idealized nature of the models the ligaments can be axially compressed passed their bucking point without deflecting into a buckled state. As the beam continues to be axially compressed the ligament will contain a large amount of stored elastic energy compared to the amount of energy it would contain in the buckled configuration. Eventually, this overloading will eventually be relieved, causing a violent conversion of the elastic energy into kinetic energy. The conversion will cause a rapid acceleration of the nodes leading to simulation crashes.

To improve the stability of the simulation and to gain a better representation of the collapsing behavior of beams, intensional imperfections are made to the alignment of the liagaments. Ferri [21] implements this in their compression of plates. In their work the deformation eigenmodes are found and then a combination of lower order modes and higher order modes are used to induce imperfections in the initial alignment of their plates, allowing them to recreate buckling in their plates.

The eigenmodes of deformation describe the characteristic ways in which the body could deform. These modes be represented as the sum of sine and cosine functions, at different spatial frequencies. The lower frequency terms contain information on the bulk motions of the deformation, while the higher frequency modes contain the information for the more local deflection. The lower frequency modes require less internal energy to materialize than the higher frequency terms. In slower compressions, the energy in the system will only activate the lower energy modes of deformation. But in higher rates of compression, there is more energy input to the system and the higher energy modes of deformation are activated along with the lower modes. These higher modes of deformation can be seen in figure 3.10.

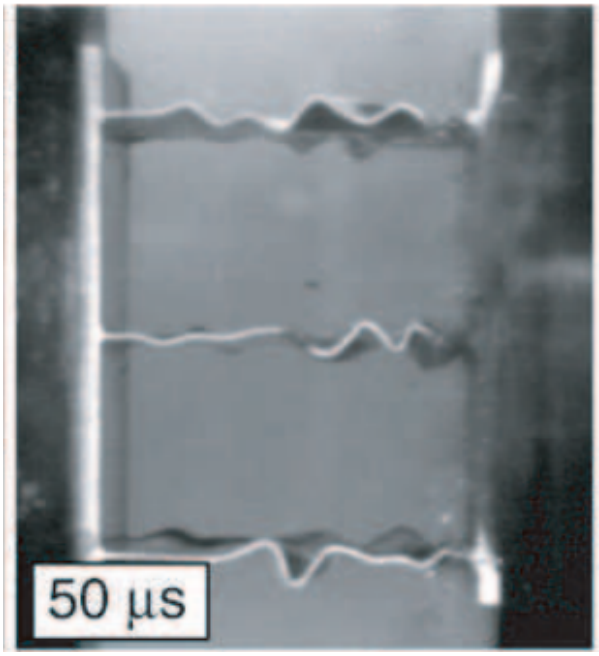

Figure 3.10: Image of initiation of buckling in metal plates, notice the high frequency sinusoidal shape of the buckling mode. Image from Ferri 2006 [21]

Because of the rapid compression of ligaments in the model is necessary to introduce high and low frequency perturbations to the alignment of the ligaments. Neglecting the higher frequency terms will cause the local overloading during rapid compression, and incurring the instabilities that were described before.

In application, the frequency of perturbation that can be induced is limited by the number of elements and the polynomial order of those elements. It is impossible to induce the levels of perturbations as done in [21], without using an excessive number of elements. Because only linear elements are suited for use in rapid compression, the number of eigenmodes in the beam is limited. Thus for this work the lowest frequency will be used in addition to a frequency given by $\omega = n_e - 2$ where n_e is the number of elements used. The magnitude perturbation added to the ligament is given by:

$$\Delta(s) = \Delta_0 \left[\sin\left(\pi \frac{s}{L}\right) + \frac{1}{\omega} \sin\left(\omega\pi \frac{s}{L}\right) \right] \tag{3.35}$$

Where Δ_0 is a perturbation scale, L is the length of the ligament, s is the arc length and ω is the higher order frequency chosen. When the ligament is being created, a random normal vector, orthogonal to the ligament, is created and then the nodes of the ligament are perturbed in this direction by the magnitude given in equation 3.35.

Chapter 4

Geometry Generation

4.1 Geometry Creation

The cellular solid type microstructures have been generated from four basic methods. If a cellular structure is patterned, such as in sandwich paneling, a unit cell can be defined and recreated directly by a researcher. Then only one cell or a small set of these cells can used to ascertain properties about the material. If a larger geometry is required, it can be created by stamping the unit cell over and over again[32, 31]. However most foams do not fit into this classification.

The most direct and accurate method for developing a cellular geometry for a computational mesh is via scanning the cellular structure, performing image segmentation, and then stitching the images together to form a three dimensional geometry. This type of geometry generation is common in medical applications in the generation of trabecular bone meshes[39, 80]. With the scans these methods require a significant amount of image processing to recreate the geometry, and the geometry created is then a full three dimensional geometry with surfaces and volumes. Additional work would be required in order to transform these representations into a form that would be useable in the beam network model.

The next most detailed generation method used by Gaitanaros requires the use of a computational simulation to recreate the basic phenomena of the foam forming process as done in [24]. In their work they create a bubble froth and let the froth settle into a steady state from which they then recreate a beam geometry.

The last method, uses a tessellation in order to generate geometries that serve as facsimiles to the foam microstructure and don't seek to recreate it from a reference geometry. The choice of tessellation is typically Voronoi. Voronoi tessellations take in a set of points in space and then define regions of space that are closest to a particular point (figure 4.1)[10]. While the Voronoi tessellation process does not generate regions though physical reasoning, it develops geometries appropriate enough for study [42, 26, 91].

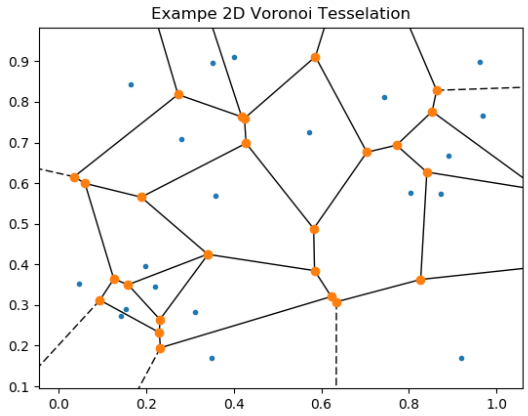

Figure 4.1: An example of a two dimensional Voronoi tessellation made from a random seeding of points. Lines separate the regions of closeness from one another. Solid lines have a finite terminals, while the dashed lines extend to infinity.

In this work the seeding and tessellation method was used to generate the geometries for study. This was done because of the speed at which the geometries could be generated and the ability for the generation of irregular geometries with minimal adjustments. The need to be able to generate different types of geometries is important because of differences in cell formation during the production of foams. See section 1.3 for more details on the formation of foams.

The schematic for generation of the cell geometry is comprised of the following steps:

1. Define a domain on interest
2. Seed volume points inside and outside of the domain
3. Perform tessellation
4. Perturb tessellation
5. Clean tessellation
6. Scale tessellation

Step 1: Define Domain

The general process of generating the geometry involves generating a larger geometric structure and then pairing it down to a size that is appropriate for the use in a numerical experiment. At the periphery of the generated geometry there will be artifacts that are unwanted in the actual geometry, thus it is necessary to define an initial domain of interest that will serve as the framework for later steps. A basic box domain is shown in figure 4.2.

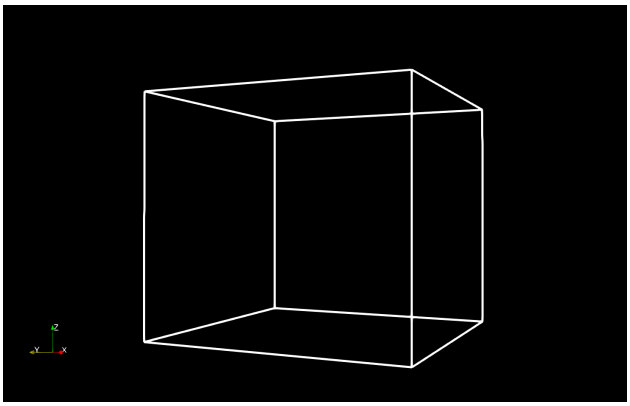

Figure 4.2: Example Three Dimensional Domain

Step 2: Seeding The Space

In this step the seed points that are to be used by the tessellation are generated. This is one of the two stages where irregularities can be introduced in the geometry, the second being in step 4. If the seeds are placed in a pattern then a regular geometry will be created by the tessellation, if the seeding is not patterned then geometries like that produced in figure 4.1 will be created with no clear repeated pattern.

There are several ways to give initial positions for the tessellation centers. Zheng [91] used a weighted placement method, such that seeds are placed based on a probability function in the domain, and that areas near other seeds had a lower probability than more remote areas and by adjusting the probability decay rates more or less regular geometries can be formed. Another method is to place seeds using a stencil with a random perturbation to the location. This method allows for some control over the basic form of the geometry, but not enforcing a regular geometry.

With a seeding method chosen the domain of interest and the space around it is filled with seed points. A satisfactory fill of the space not only seeds the domain the domain of interest, but also a buffer of points outside of the domain. These seeds ensure that the pattern formed in the domain is predominantly an internal pattern, and not one too heavily influenced by the edge effects of the tessellation. Examples of a regular stenciled seeding and a perturbed stencil seeding are shown in figure 4.3

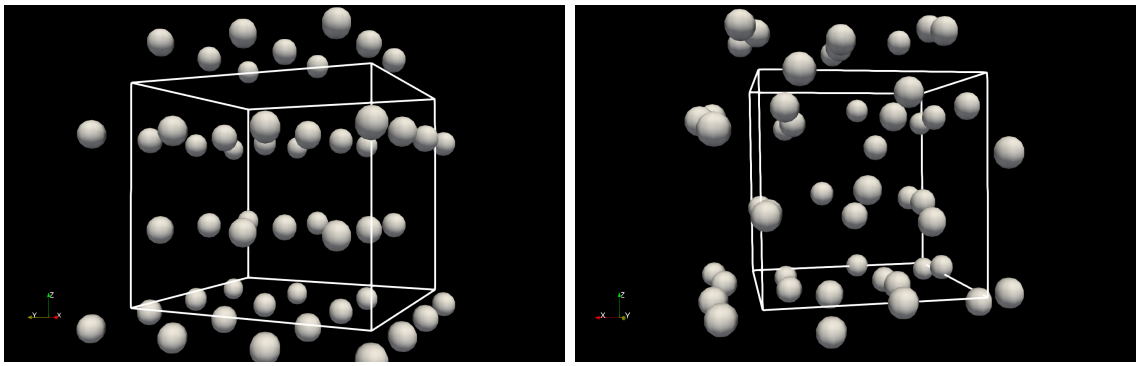

Figure 4.3: Seeding of the geometric domain. (Left) Regular patterning, (Right) Irregular patterning from a perturbation of the regular seeding

Step 3: Tessellation

Tessellation involves creating regions under a particular set of constraints that fill a space. The tessellation chosen for generating the foam geometry is a Voronoi tessellation. Voronoi tessellations form regions of nearest points to a set of prescribed locations, and in doing so form a set of convex regions. This has been an attractive option for formation of cell like geometries in microbiology [79, 12], and in two dimensional generation of foam like structures [91].

In this work a three dimensional Voronoi tessellation is performed on the seeded points. The library used to perform the tessellation is the SciPy spatial library. The spatial library is a python wrapper to the Qhull library [6]. The spatial library produces the Voronoi tessellation as a series of vertices and faces. The faces are an index of the vertex points, that separate the different regions. The face and vertex information is processed to become a series of edges connecting the vertices. The edges and vertices are then used to represent the ligaments of the open-celled foam. The results of the the tessellation and processing are show in figure 4.4.

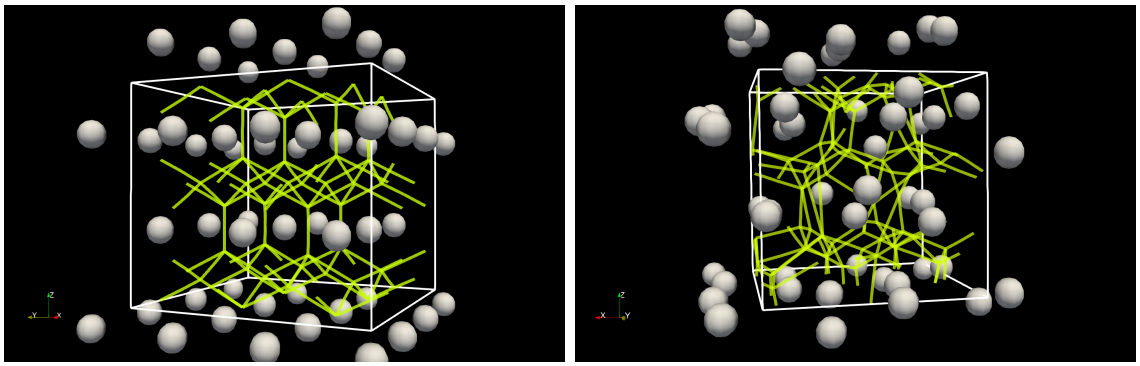

Figure 4.4: Raw tessellations generated by the Voronoi method. (Left) Structure from a patterned seed, (Right) structure from seeds with random variation.

Step 4: Perturbation

After a the tessellation is generated, there is a second opportunity for adding random variation with in the structure. Zheng in addition to their probabilistic seeding method in [91] explored the effects of altering a regularly tessellated structure with random variation in the positions of the ligament vertices. Thus the same connectivity is preserved, but where those connections link is different, as illustrated in figure 4.5.

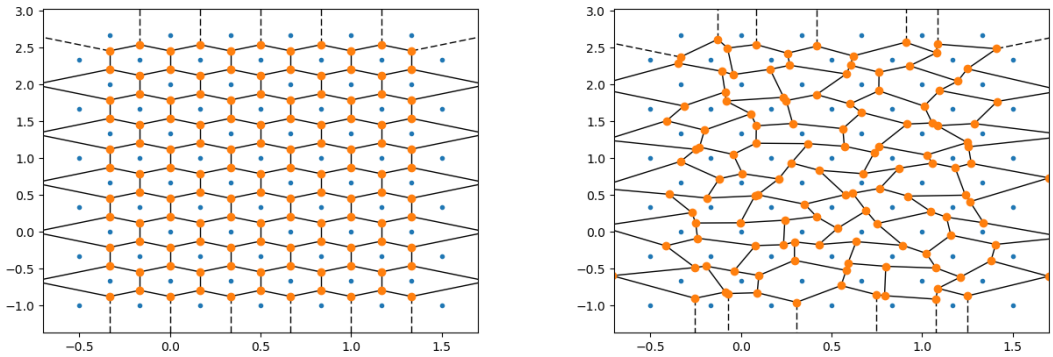

Figure 4.5: Example of the second type of random variation for cellular geometries, where a regular geometry is formed and then randomly perturbed. (Left) Original tessellation (Right) Randomized tessellation, generated from the regular tessellation.

The method used to perturb the vertices is the same used by Zheng, except applied to a three dimensional space. Where the new location a vertex will be located is:

$$\vec{X}_{new} = \vec{X}_{old} + \Delta\vec{n}(\theta,\phi) \qquad \vec{n}(\theta,\phi) = \sin(\phi)\left[\cos(\theta)E_1 + \sin(\theta)E_2\right] + \cos(\phi)E_3 \quad (4.1)$$

Where $\vec{n}$ is a unit vector described in spherical coordinates θ and ϕ. The displacement scale, Δ, is held constant while θ and ϕ are randomly distributed from $[0, 2\pi)$ and $[0, \pi)$ respectively.

With the perturbations, as can be seen in figure 4.5 there will now be a distribution of ligament sizes. The variation in the lengths of ligaments were tested and summarized in figure 4.6. It can be observed that a gaussian distribution centered slightly above the unperturbed length of the ligament fits quite well. Thus if a spread of the ligament lengths can be found and fit to a gaussian curve the spread can be mimicked by scaling the perturbation magnitude. This scaling to magnitude seems to be approximated by:

$$\sigma = .72\Delta \tag{4.2}$$

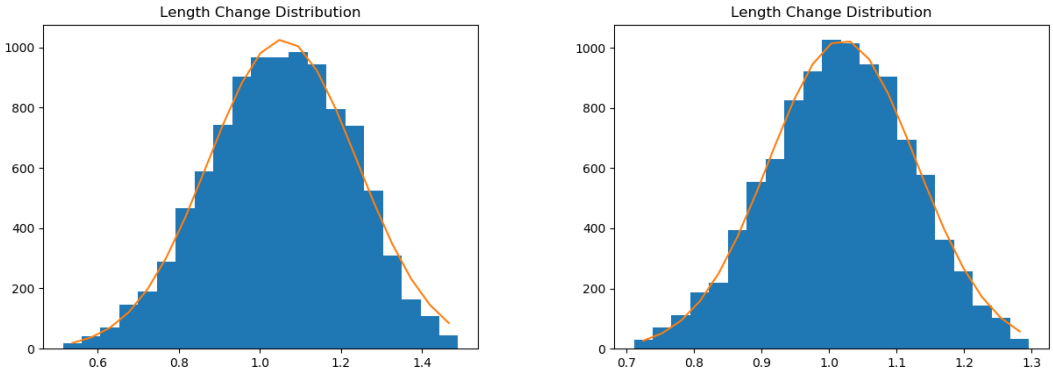

Figure 4.6: Changes in the length of a unit long ligament subject to a random three dimensional spherical perturbation. A fitted gaussian curve has been overlaid, showing good correspondence to the distribution obtained. (Left) .25 perturbation with a standard deviation of .18 (Right) a .15 perturbation with a standard deviation of .11

Step 5: Clean Tessellation

The resulting geometry generated by the tessellation will need to be trimmed to fit into the domain of interest and be cleaned to remove undesirable ligaments.

To trim the generated geometry, all ligaments that join vertices that are outside of the domain of interest are removed. Then any ligaments that join a vertices that is within the domain to a vertex out side of the domain are truncated. The truncation is done by projecting the outer vertex on to the nearest face of the domain of interest, and taking this projected point as the new end vertex of the ligament. In situations where the projection places the new end vertex near a corner of the domain of interest, it can be necessary to do several projections over the relevant surfaces of the domain, in order for the new vertex to be within within the domain of interest.

With a geometry that has been trimmed and/or has been made irregular from random seeding of points or by perturbing vertex locations, ligaments can be formed that are ill-suited for computational studies. This is because there can be a dramatic variation in the lengths of edges/ligaments formed. When there are very small ligaments formed they will be the governing factors in dictating the stability of the problem because of the CFL condition(equation refeq:cfl).

$$\delta t = \alpha \frac{\delta x}{c} \tag{4.3}$$

Where δt is the largest stable time step, δx is the smallest element in the problem, c is the fastest wave speed in the problem, and α is a constant dependent upon the choice of spatial and temporal discretizations [49]. The CFL condition means that the smallest ligaments restrict the time step size. When irregular geometries are created, especially if done by random seeding, the ratios of the largest to the smallest ligament can be on the order of $100:1$ or larger. Ratios of this degree can drive the computational time required to solve the problem to intractable scales.

To alleviate the problems caused by the CFL condition, it was decided that the smallest of ligaments (based on an aspect ratio to the largest ligament) would be removed. When a ligament is removed the end vertices are merged together. In the merger the points' locations are averaged together to form the replacement points location, and all other ligaments that were associated with those endpoints are tied to the replacement point. It was chosen that the limiting ratio for the ligaments be 10:1 such that the smallest ligament could only be a tenth of the longest ligament. This ratio was chosen on the grounds that it preserved feasible compute times with the hardware available, with more computing power it would be possible to increase this ratio.

Step 6: Scale Geometry

Currently the geometry exists in a form that can be used in a simulation.The simulation will take the edge and vertex information, break each ligament in to separate elements and assign appropriate field values to it. Before that though it may be useful to scale the structure. One aspect of foam's microstructure is that they often have a rise direction, see section 1.3. However, it is tricky to seed a geometry to generate the distinct rise direction. Thus, after cleaning it is useful to now stretch a direction of the geometry. This can be done (assuming that one of the corners of the domain of interest is at the origin) by using equation 4.4, where λ is the scaling in rise direction, n_i is the i'th component of the normal vector pointing in the rise direction, x_i is the i'th component of the current vertex position and $\vec{E}_i$ is the component unit vector.

$$\vec{x}_{new} = \sum_{i=1}^{3} ((\lambda - 1)n_i + 1)x_i \vec{E}_i \tag{4.4}$$

4.2 Geometric Parameters

Seed Locations

A stencil for an approximation of the foam structure requires information on the mean size of the cells in the foam and how they are distributed. From [8] it can be stated that the Zorbium foam has an average cell diameter of about $200\mu m$. For the distribution of the cell lengths it was necessary to perform some rough image analysis in order to generate an approximation for the standard deviation of cell lengths. From a collaborator,Dr. Jennifer Sietins, at the Army Research Labs a scan of Zorbium was provided, shown in figure 4.7 .

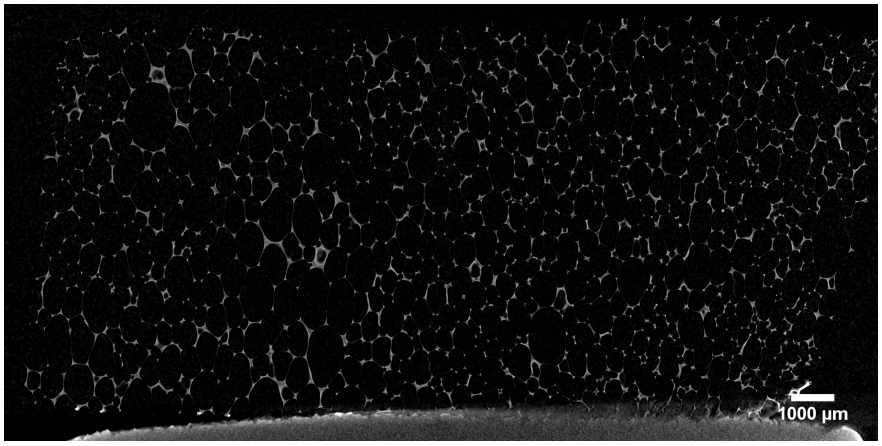

Figure 4.7: Scan of Zorbium foam provided by Dr. Jennifer Sietins.

From the scan it can be seen that there are regions of material and regions of void, as to be expected in a cellular material. To obtain an exact measurement of the distribution of ligament lengths or cell volumes would require the efforts of three dimensional recreation. For this work, an approximation for the different cell sizes will be used based of the centers of voids in the foam. By identifying the centers of the voids and then binning them, the local average areas for the cells can be approximated. Then assuming cells are square, this average area of a bin can be translated into an approximation of the average length of ligament.

To perform this analysis the centers of the void need to be found. While the use of watershead algorithms and the like are useful in finding the center of objects, they are difficult to use because the amount of material present in the scan is so sparse. Thus the centers of the voids were manually identified and marked with white circles, shown in figure 4.8. To identify the centers of the marking circles the python extension for OpenCV was used[13].

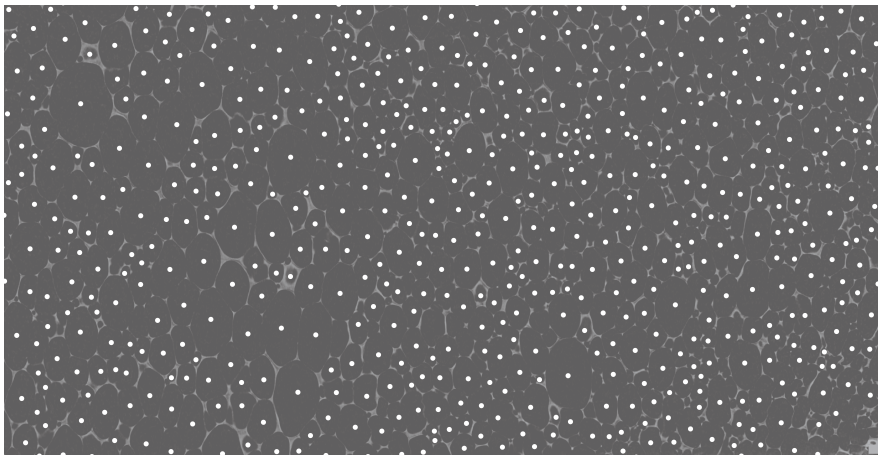

Figure 4.8: Scan after being cropped and the void centers labeled with white circles.

The centers of the circles were grouped into regions by the use of a two dimensional histogram. With this clustering a variation in the amount of centers in region was apparent, as seen in figure 4.9. The average area of each void region was determined by dividing the area of each bin of the histogram by the number of centers it contains. From using the average area the corresponding average length of the cells could be determined. From the distribution of average lengths found a gaussian was fit in order for the standard deviation to be used in equation 4.2 of step 4 of geometry generation. From the test it was observed that there is an approximate standard deviation of the ligament lengths of about 19 percent of the mean length.

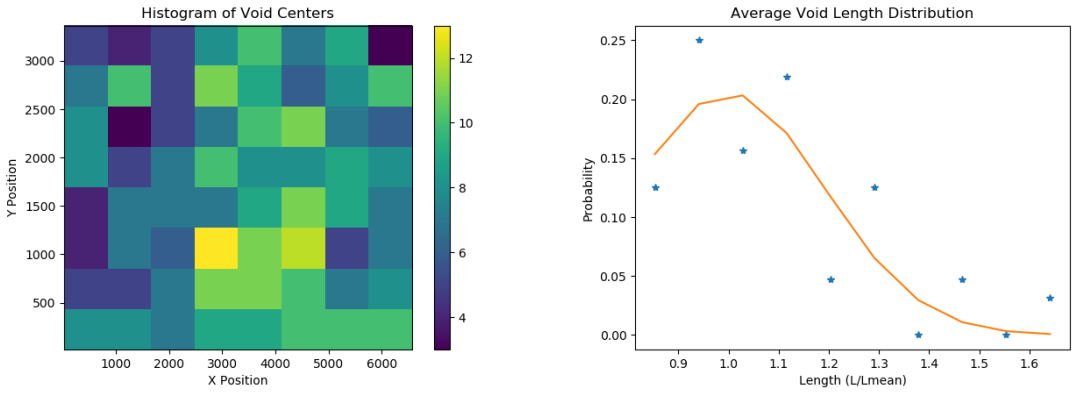

Figure 4.9: Results of center binning and the distribution of approximate ligament lengths.

Looking at the results of the figure 4.9 it is apparent that it does not match the distribution obtained in figure 4.6. The main reason this discrepancy may exist is because figure 4.9 is using a two dimensional scan to approximate a complicated three dimensional

structure. By only looking a one slice of the structure, there will be various parts of each cell represented by the structure. A more detailed analysis of the distributions is outside of the scope of this work. The goal was to provide a rough approximation to be used later.

Density

Relative density (equation 4.5) of foams play a significant roll in the determination of the behaviors of the foam. Relative densities higher than 10-15 percent show significant reduction in the plateau region of the loading curve, thus leading into more rapid transition from the elastic region to to the densification region [28]. Thus in order to replicate the physics of the protective liners it is important to perform the study with a similar density to that of the actual foam.

$$\rho_{rel} = \frac{\rho_{foam}}{\rho_{solid}} \tag{4.5}$$

Zorbium is a polyurethane based foam [23], while the the author is unaware of the solid density of Zorbium, the solid density of polyurethane is known. Using the density from [28] for polyurethane and the density of the Zorbium foam from [23] we can get an approximate figure for the density of the foam.

Polyurethane density [28]	$1.2Mg/m^3$
Zorbium density [23]	$54Kg/m^3$
relative density	.045

Table 4.1: Density information used for the approximation of the Zorbium foam.

Chapter 5

Experiments

In tis chapter two experiments were run using using the Green-Naghdi beam network model for open celled foams. The first experiment observes the changes in behavior of a beam network as the rate of loading changes. The second experiment preforms an impact test with regular and irregular networks and observes the changes in shock propagation within them. The material properties used were based off of data on bulk polyurethane, the following values for the parameters were used in each model.

- Density: $1.2 \times 10^{3 kg/m^3}$
- Drag: $.45 kPa \cdot s$
- Poisson ratio: 0.4
- Shear Modulus: $47 MPa$
- Contact Penalty: $4500^{MN/m}$
- Friction Coefficient:0.2

5.1 Unit Crush Experiments

The first test was performed to observe the changes in the cells behavior due to changes in the compression rate. As the speed of compression becomes closer and closer to the elastic wave speeds of the beams, the structure becomes less capable of responding to compression as a complete structure, instead the response becomes more localized in regions near the initial compression. The inability for the structure to respond as a whole, would lead to deviations from the linear-plateau-densification curve as detailed in section 1.3 would be expected.

The test is run by placing a foam geometry between two parallel walls, as shown in the schematic in figure 5.1. One wall is fixed in place while the other wall is given a fixed velocity

at which to approach the other wall. In doing so the network cell in between them is forced to deform. The geometry used in the study was a cell of the structure formed from a staggered square placement of seed points, producing a cell of approximately $200\mu m$ in diameter.The cells generated have a combination of hexagonal and rhomboidal sides, similar to the Kelvin cells.

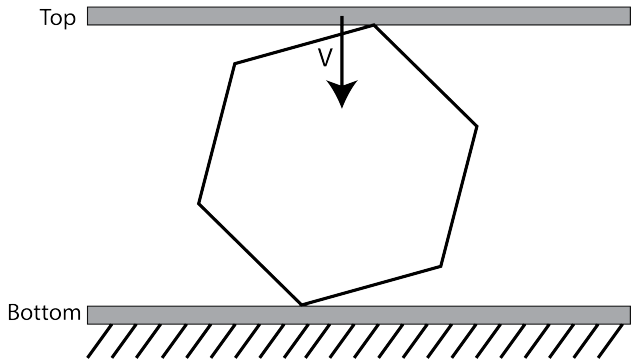

Figure 5.1: Schematic of the the unit crush test. The unit cell is placed between two rigid plates, the bottom, held fixed and the top moves downward at a speed V.

For the material parameters used the linear compressive wave speed is about $470^{m}/_{s}$. To get a range of structural responses a range of crushing speeds were selected: 5, 10, 50 , 100, 250 and $500^{m}/_{s}$. The lowest speed, $5^{m}/_{s}$, is in the quasi-static loading domain, to observe the linear-plateau-densification response. The highest speed, $500^{m}/_{s}$ was chosen to observe the response of the model at speeds greater than that of the compressive wave speed. The speeds chosen in between were to chosen to observe the transitionary behaviors between the quasi-static to extremely rapid deformation rates. Time lapses of the crush tests at $5, 50, 100,$ and $500^{m}/_{s}$ are plotted in figures 5.2, 5.3, 5.4, and 5.5, respectively. The reaction stresses upon the wall though the tests are reported in figures 5.6, 5.7, and 5.6.

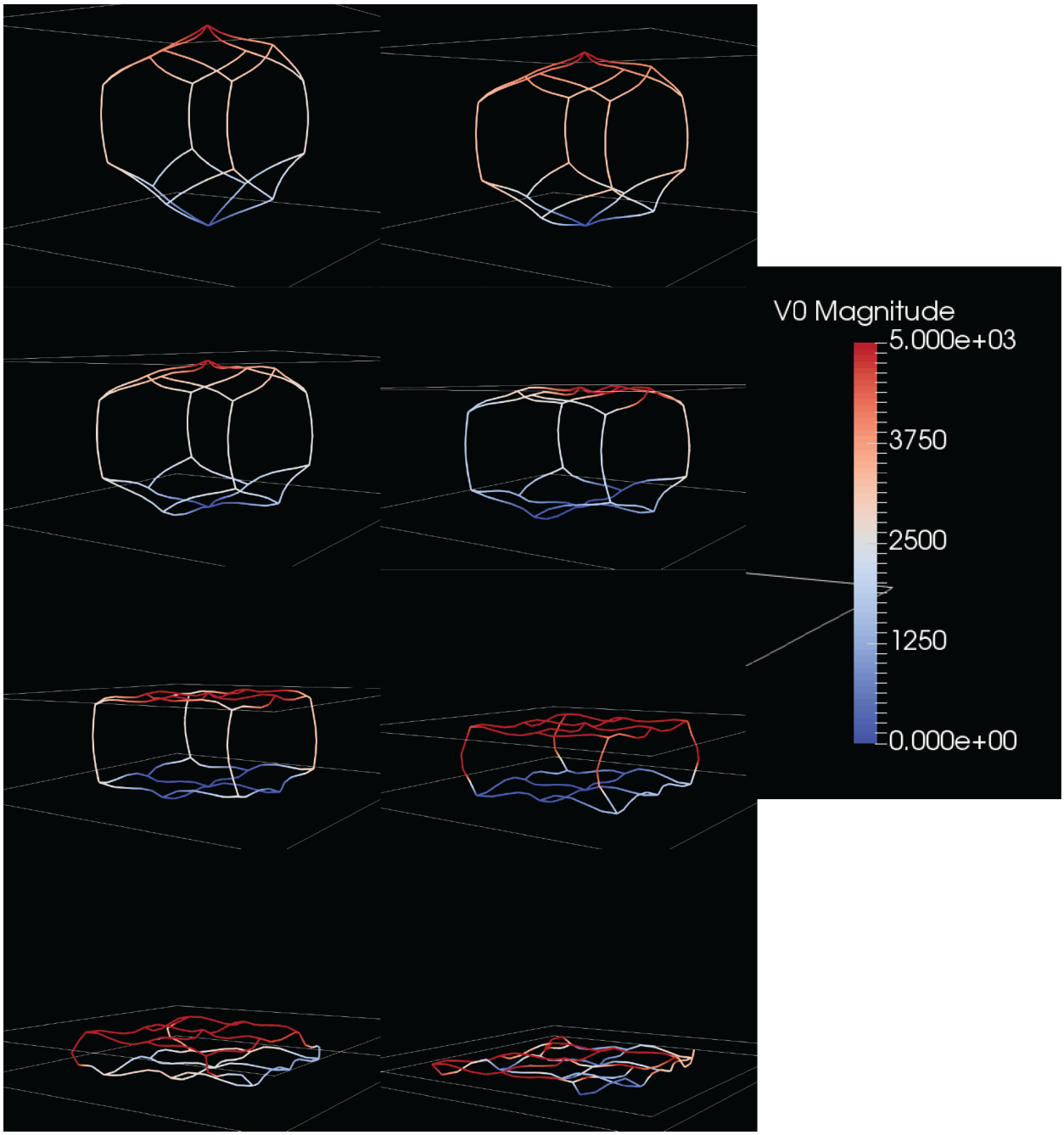

Figure 5.2: Deformation progress of a simple cell by a wall at $5^{m}/_{s}$, velocity scale in $^{mm}/_{s}$

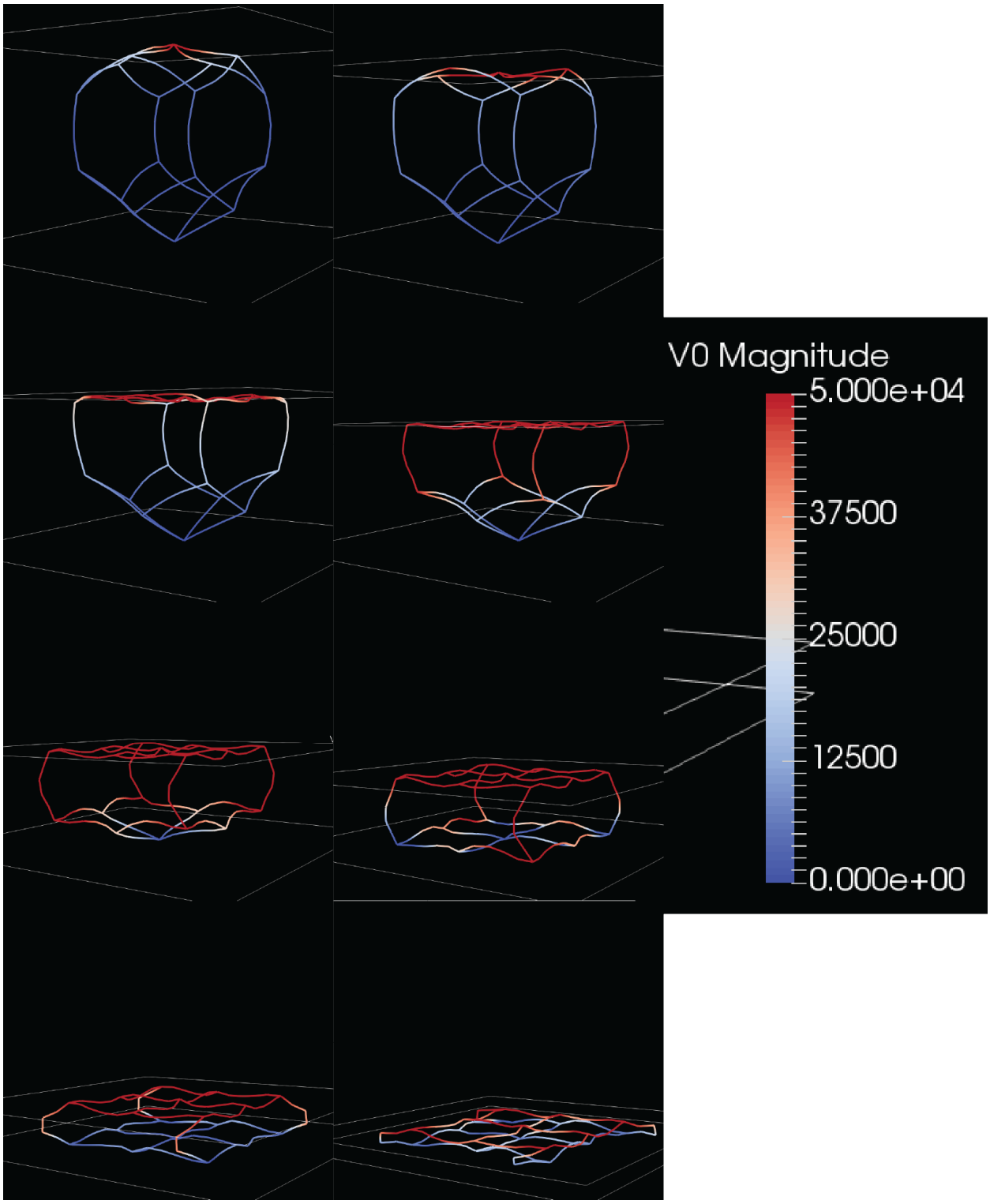

Figure 5.3: Deformation progress of a simple cell by a wall at $50^{m}/_{s}$, velocity scale in $^{mm}/_{s}$

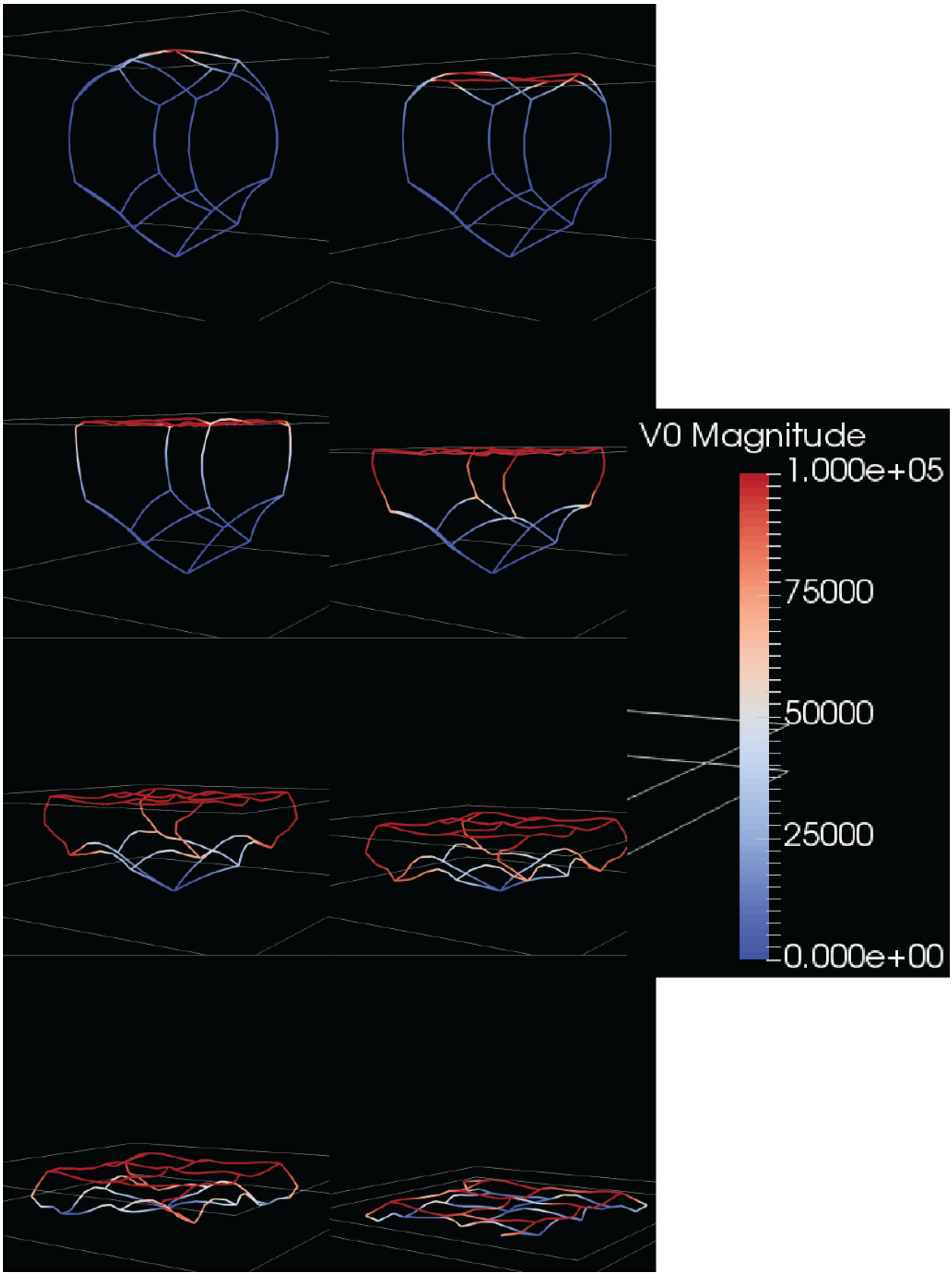

Figure 5.4: Deformation progress of a simple cell by a wall at $100^{m}/_{s}$, velocity scale in $^{mm}/_{s}$

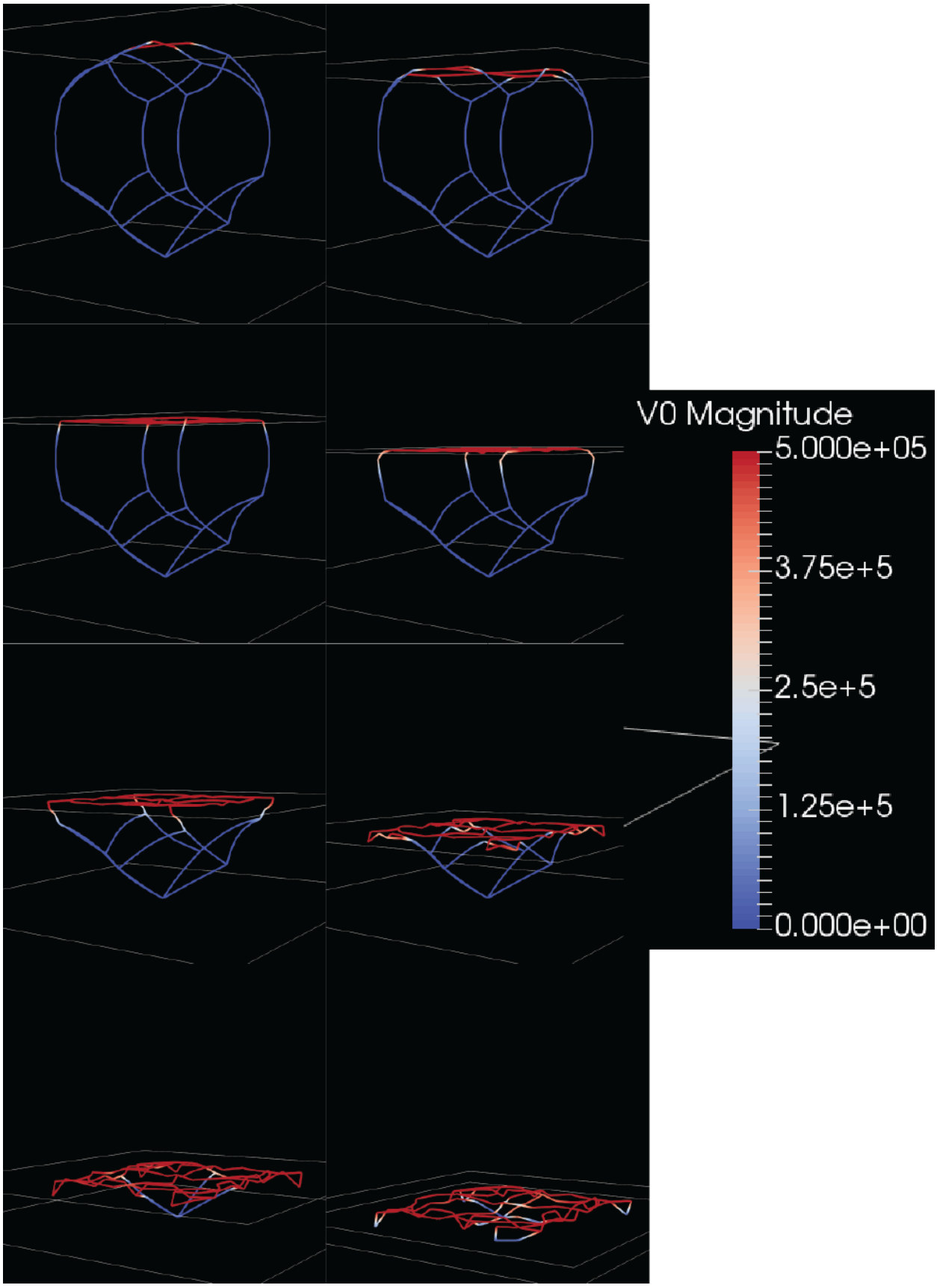

Figure 5.5: Deformation progress of a simple cell by a wall at $500^{m}/_{s}$, velocity scale in $^{mm}/_{s}$

From the observations of the different deformations of the cell it can be seen that there is a change in the manner of deformation as expected. At a $5^m/_s$ It can be observed that at the structure responds globally to the reduction in the vertical height (figure 5.2), while at $100^m/_s$ and $500^m/_s$ (figures 5.4 and 5.5) all of the deformation is localized closely with to the moving wall.

Examining the deformation patterns in the $5^m/_s$ crush case, the bending of the upper and lower ligaments bending being the primary mode of deformation present in the beginning. While these ligaments are bending, the vertical ligaments do not deform very much at all, but displace themselves rather rigidly downwards.

Bending of the top and bottom ligaments continues to be the dominant deformation mode until the distance between the walls is approximately the height of the vertical ligaments. At this point, further bending of the top and bottom ligaments does not move the structure further out of the way of the walls, the vertical members start to become compressed. The onset of this compression causes a massive spike in the reaction forces in the wall's, figure 5.6.

Eventually the compression progresses to buckling as the vertical ligaments no longer can supply a vertical force. Reducing the walls' reaction forces. This continues until the compression is great enough that the ligaments begin to come in contact with one another, at which the forces felt at the walls begin to increase dramatically again.

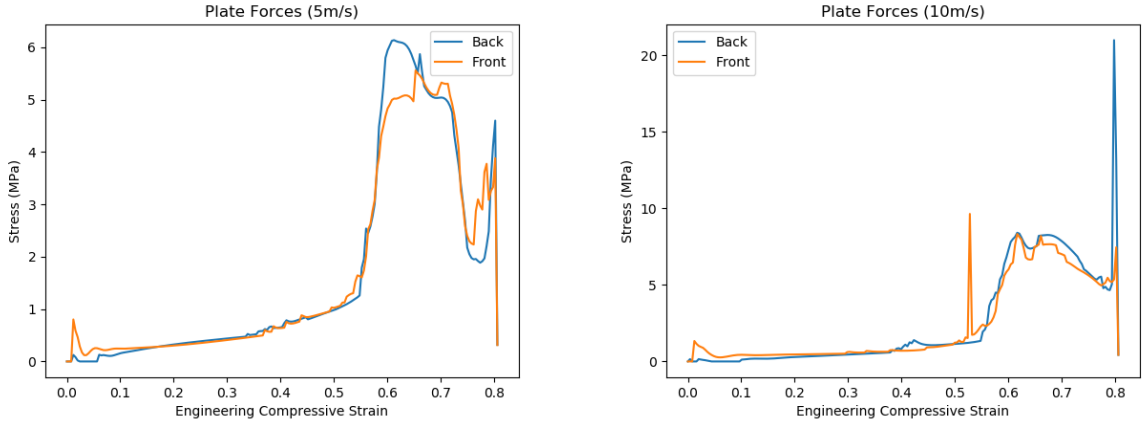

Figure 5.6: Reaction stresses on the top and bottom walls during the crush test, done at $5^m/_s$ and $10^m/_s$. Spikes in the plot indicate impact events along the walls.

In figure 5.3 where the crushing is done at $50^m/_s$ it can observed that in the deformation of the cell there is not nearly as global of a response to the imposed deformation as in the $5^m/_s$ case. This change is to be somewhat expected as the rate of deformation relative to the compressive wave speed has increased from about1 : 100 to about 1 : 10. In the deformation of the $50^m/_s$ case it acts like the $5^m/_s$ case where the initial bending of the top and bottom ligaments happens in a staggered fashion, while in the $5^m/_s$ case they bent simultaneously. In

the $50^{m}/_{s}$ case initially only the top ligaments as they bend. It is only when the bending of the top ligaments reaches the point where the vertical ligaments are pushed by the wall that the lower ligaments begin to bend. The bending of the lower ligaments is the only mode of deformation until the vertical ligaments become in contact with the bottom wall, at which point the compressive, buckling and densification behaviors mimic that of the $5^{m}/_{s}$ case.

In the the crush tests at $100^{m}/_{s}$ and $500^{m}/_{s}$ (figures 5.4 and 5.5). The deformation patterns become extremely local as the crush rates to compression wave speed ratio go to approximately $1:5$ and $11:10$. In the $500^{m}/_{s}$ crush case there is not noticeable deformation occurring away from the impacting wall, and only very late in the crushing simulation is there any apparent deformation in the cell off of the wall as the ligaments pressed against the wall the ligaments ahead of them in the crush direction. The $100^{m}/_{s}$ case is very similar except later on in the crush test a leading elastic deformation can be noticed before the region of complete collapse catches up. In these cases, and for the $250^{m}/_{s}$ case the impact spikes present in the reaction stresses in figures 5.7 and 5.8 indicate that the external response felt by the walls is more dominated by impact events of the structure against the walls and itself than the internal response of the ligaments.

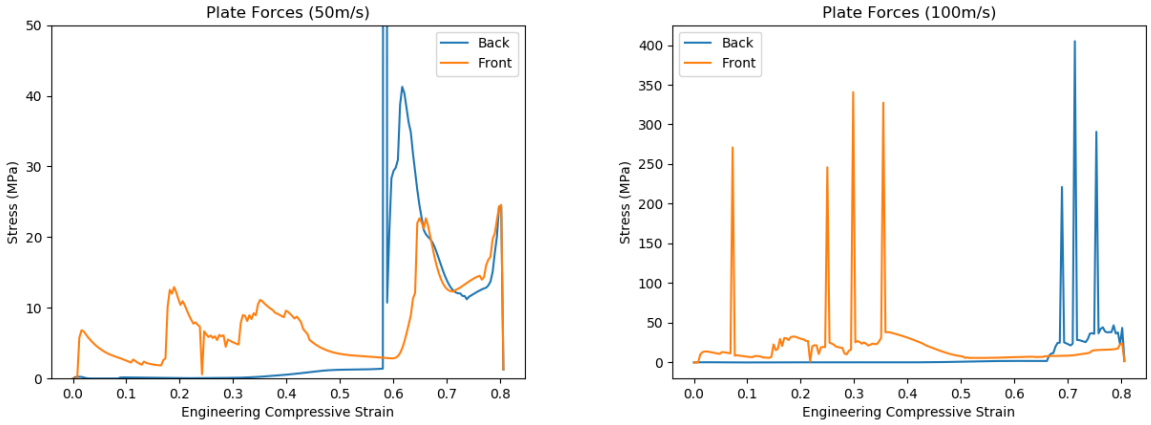

Figure 5.7: Reaction stresses on the top and bottom walls during the crush test, done at $50^{m}/_{s}$ and $100^{m}/_{s}$ Spikes in the plot indicate impact events along the walls.

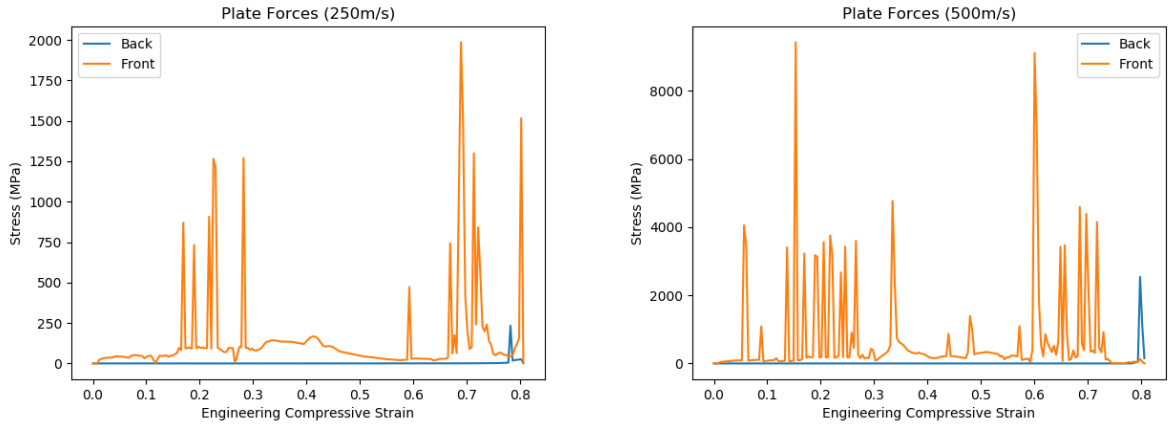

Figure 5.8: Reaction stresses on the top and bottom walls during the crush test, done at $250^{m}/_{s}$ and $500^{m}/_{s}$ Spikes in the plot indicate impact events along the walls.

These changes in deformation patterns and the changes in reactions against the walls (figures 5.6, 5.7, 5.8). Indicate a transition of behavior that that is mentioned by Gibson [28]. In [28], Gibson describes that in dynamic impact problems at low rates the foam will absorb the energy in the patterns described in section 1.3 where the characteristic elastic-plateau-densification pattern is followed. However at higher rates of impact the main resistive effects arise less from the actual bending and compression of the foam ligaments but from the repeated impacts and collapsing events that occur in the deformation process.

It can be seen in the results that at low rates of crushing the reaction stresses follow a rather smooth curve, and as the rates of deformation increase the reactions become dominated by high stress spikes which are the result of impacts of the wall against the structure, suggesting a change in loading mode as proposed by Gibson.

5.2 Shock Experiment

In this numerical experiment, several foam geometries are run in a numerical crush experiment at dynamic velocities. At these velocities, a densified region of foam material forms in front of the impactor and propagates froward though the material. Using the microstructural model, the relationship between the shock front speed and the impact speed can be used to identified for the foam. The rigid-perfectly-plastic-locking (RPPL) model can be used to translate the shock front speed information into a locking strain which can be used in one dimensional macro-scale models and to compare the results of the model to expected values.

Summarizing from section 1.3, when there is rapid local deformation in material, discontinuous changes in material state can occur. Using the RPPL assumption a linear relationship is expected to arise from comparing the shock speed and speed of the impactor:

$$C_s = c_1 U_{imp}. \tag{5.1}$$

The constant of proportionality, c_1, is related to the locking strain, ϵ_L, of the RPPL model by equation 5.2. The locking strain is the maximum strain the foam will undergo before it locks and becomes effectively rigid.

$$\epsilon_L = \frac{1}{c_1} \tag{5.2}$$

When the material locks, the state of stress the material enters,σ^*, is determined by:

$$\sigma^* = \sigma_c + \frac{\rho_0 U_{imp}^2}{\epsilon_L}. \tag{5.3}$$

Set Up

The numerical experiment run is based off gun impact tests. Where the sample of interest is placed on a track in front of an effectively rigid backer and then at the far end of the track another effectively rigid object is fired at the sample. Then various measurements of the stress and strain response of the sample and its impactors are recorded. See figure 5.9

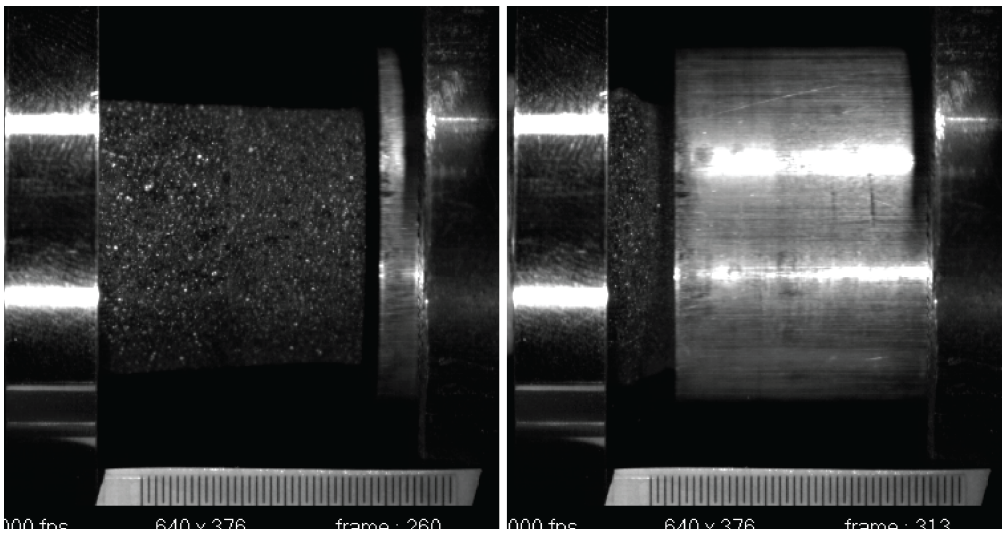

Figure 5.9: Start and end of an impact test of a cored Zorbium foam sample. Images courtesy of Dr. Chris Meredith Army Research Labs.

A similar experimental set up is implemented for the numerical experiment. The numerical foam samples are placed between a backing and impacting wall, illustrated in figure 5.10. The impacting wall will be set with a constant impacting velocity. As the impact event occurs the shock front within the sample will be recorded by observing which nodes exceed a threshold velocity. It was determined that the shock front could be reliably be identified when looking for nodal velocities greater than $100^m/_s$. By recording the position of the nodes

which exceed the threshold, a map of the shock front's positions can be created. From the shock fronts positions, a line is fitted to the path of the front and the slope of this line will be the shock speed in the lab frame.

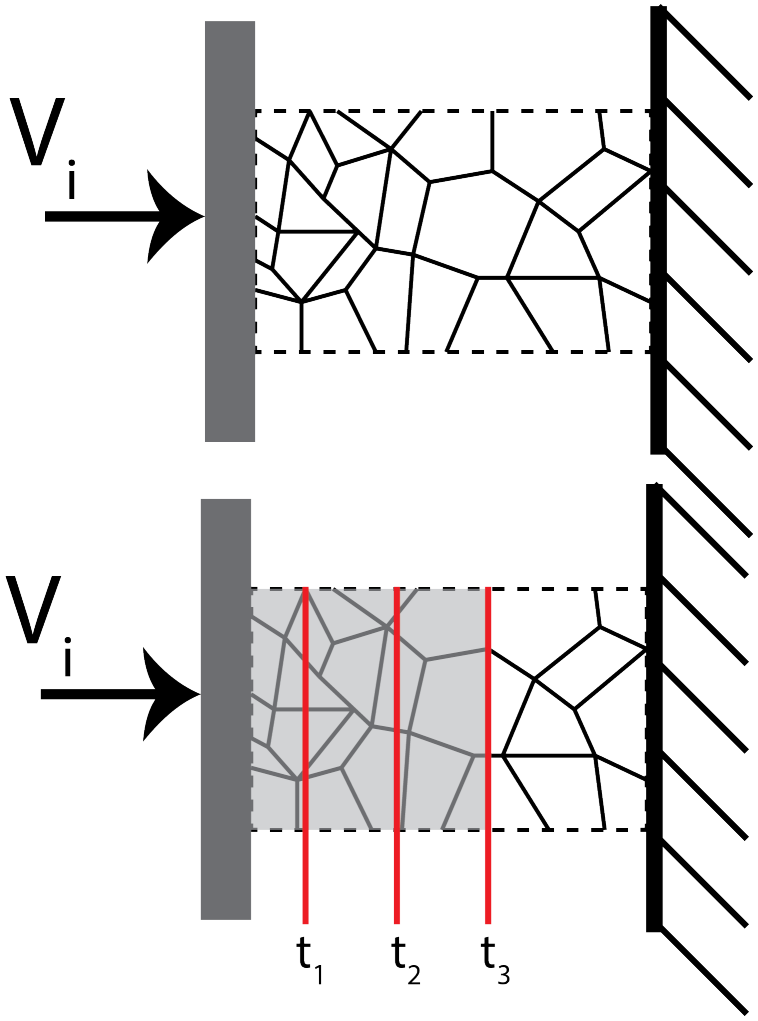

Figure 5.10: Setup and method used to determine the shock speed for a particular impact test.

Several of these experiments will be run for a particular geometry, in which the impactor velocity will be varied. In the RPPL model it is assumed that the material speed of material behind the shock is the speed of the impactor. Thus, by fitting another line to the plot of the impactor speeds to the shock speeds it its possible to obtain a value for c_1 in equation 5.1, and thus find the related model parameters.

Regular Patterned Geometry Tests

An initial set of crush tests were run on a regular patterned geometry of 3x3x8 unit cells being approximately $200\mu m$ in diameter, as seen in figure 5.11. More cells would be desirable in the cross section in order to reduce the edge effects, however due to computational limitations this was the largest geometry that could be simulated. The radius of the beams were scaled in order match a specific relative density for the structure. the test was carried over relative densities of .02, .045 and .10. These densities were chosen to include the approximate density of Zorbium and then to see the changes incurred by altering the densities. Then the crush tests were run at speeds of $150^m/_s$,$250^m/_s$,$350^m/_s$, and $450^m/_s$.

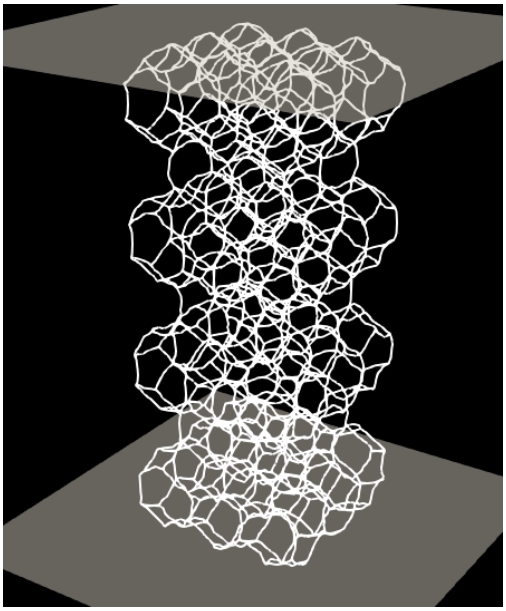

Figure 5.11: Set up geometry for regularly patterned density tests.

In figures 5.12 and 5.13 the position of the shock fronts for the 0.045 relative density foams are shown. The shock front plots for the other densities are in Appendix C. In these plots show nice alignment between the linear fit and the front's progression.

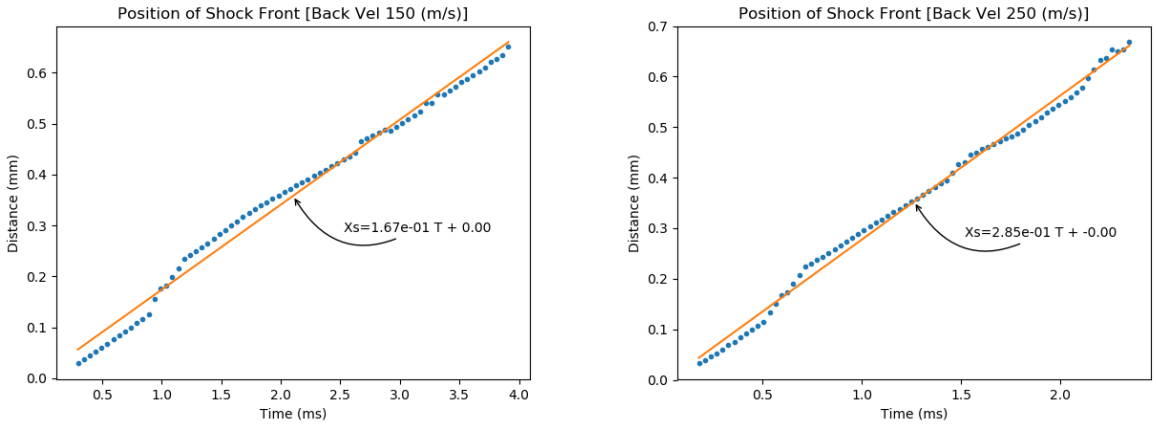

Figure 5.12: Shock Front position over time and linear approximation to position of shock front for regular patterned geometry with a relative density of .045 at impact speeds of $150^{m}/_{s}$ and $250^{m}/_{s}$

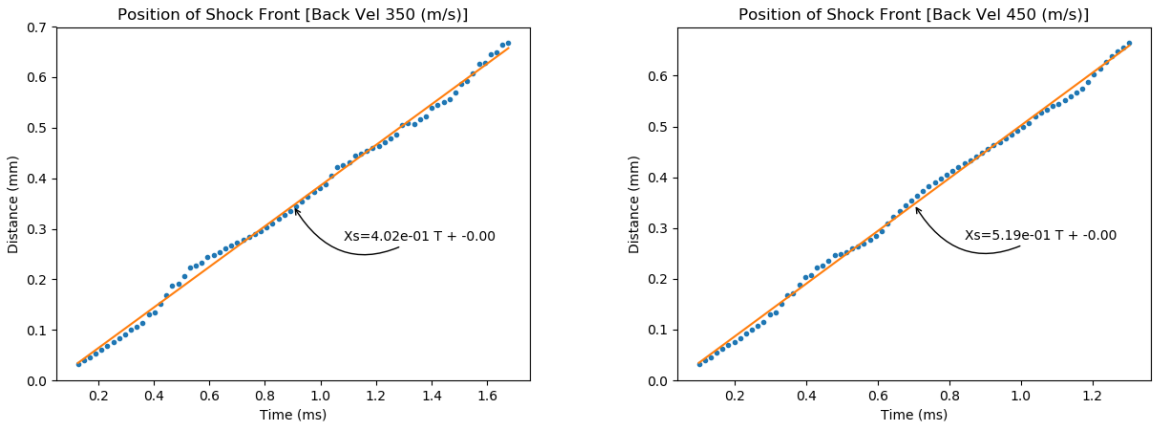

Figure 5.13: Shock Front position over time and linear approximation to position of shock front for regular patterned geometry with a relative density of .045 at impact speeds of $350^{m}/_{s}$ and $450^{m}/_{s}$

The various shock speeds for the given density of foam are plotted in figures 5.14, 5.15, and 5.16. From the figures, it can be seen that increasing the density of the structure causes an increase in the shock speed relative to the impacting back velocity. This type of behavior would be expected as the increase in density, deceases the free space between ligaments. With less free space between ligaments, contact between ligaments occurs with less relative deformation between the ligaments. With less deformation required for contact the rate at which the ligaments come into contact occurs sooner, resulting in a more rapidly advancing

shock front. The c_1 constants and their corresponding locking strains are reported in table 5.1. With less free space in the more dense materials a lower locking strain is obtained.

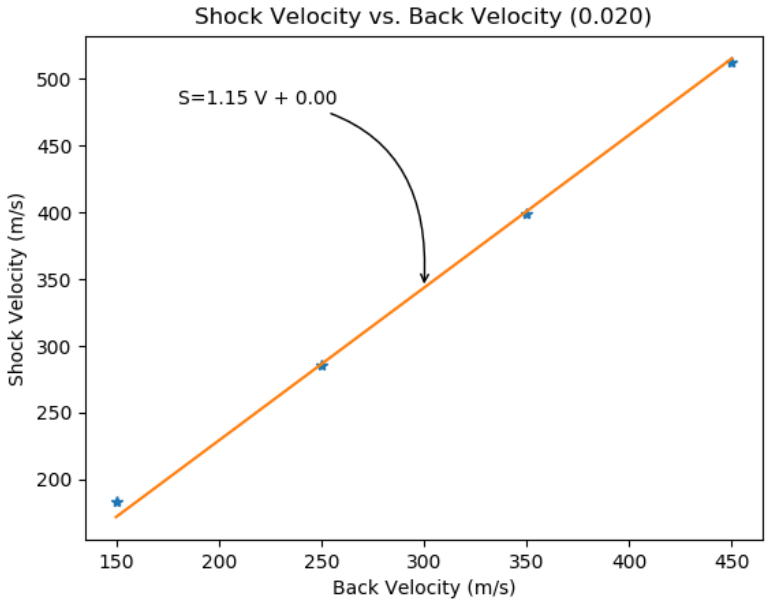

Figure 5.14: Sock speeds plotted against the impacting back velocity for .02 relative density material.

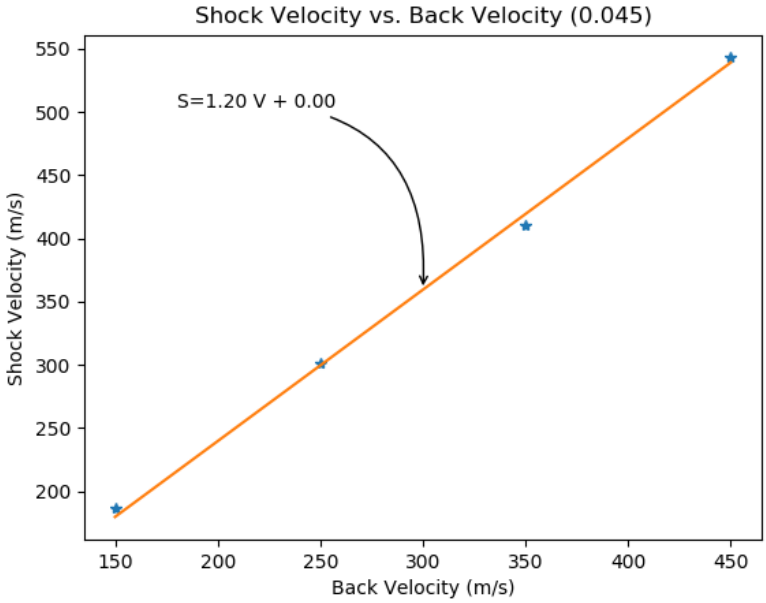

Figure 5.15: Sock speeds plotted against the impacting back velocity for .045 relative density material.

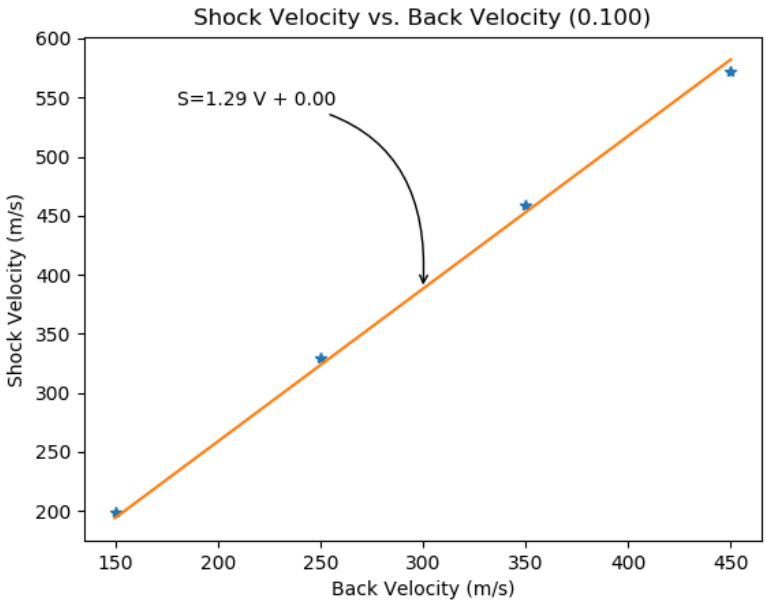

Figure 5.16: Sock speeds plotted against the impacting back velocity for .10 relative density material.

Relative Density	c_1 Constant	Locking Strain
.02	1.15	.86
.045	1.20	.83
.1	1.29	.77

Table 5.1: Velocity proportionality constants and their corresponding locking strains for various densities.

Irregular Geometries

In the tests run on regular geometries it was shown that changes in the relative density, by increasing the volume of solid material induces an increase in the speed of the shock and the corresponding decrease in the locking strain of the foam. These tests were performed on one particular geometry that is regular in patterning. In order to observe these changes in a more representative foam model the same test that was run in the previous section must be run on a series of irregular geometries in order to observe response patterns more akin to a real foam.

To generate the irregular foams a regular patterned geometry was generated in the same fashion as section 5.2. Then as detailed in chapter 4 the vertex points were perturbed to generate variations in the geometric form. Four Geometries were generated in this fashion and run under the same impact velocities as done in section 5.2 at a relative density of .045.

Because of the amount of data in this test the results are summarized in figure 5.17 and table 5.2.

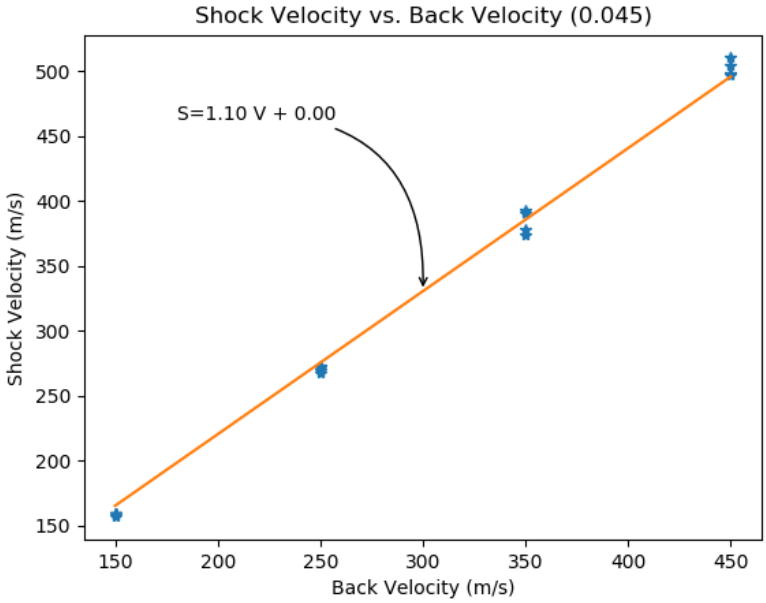

Figure 5.17: Plot of resulting shock speeds against backing velocities. Larger spreads in the the shock speeds appear at higher impact velocities.

Relative Density	c_1 Constant	Locking Strain
.045	1.10	.91

Table 5.2: Velocity proportionality constant and their corresponding locking strain for the average response of the irregular foam geometries.

From the results in figure 5.17 and table 5.2 it can be seen that at the same relative density from the regular compression tests the resulting shock speeds are slower and the locking strain is much higher. This is likely due to the loss of alignment in the geometry structures. Where in the regular structure the ligaments are aligned in such a fashion that allows them to more likely come in contact with one anohter, thereby pushing the front of the shock wave out further than in the irregular case where the ligaments are not necessarily predisposed to aligning in contact with one anohter.

Comparing these results in table 5.2 to that found in Gibson [28] the prediction for where the foam would behave in locking manner aligns well as demonstrated in figure 5.18. When designating the locking strain for the RPPL model, the stain at which the stress-strain tangent becomes nearly vertical is chosen. In the plot it can be seen that the $54^{Kg}/_{m^3}$ density foam that was simulated predicts a locking strain that aligns closely to the steepening of the $51.7^{Kg}/_{m^3}$ density foam plotted. Thus the model shows some capability in producing macro-scale parameters.

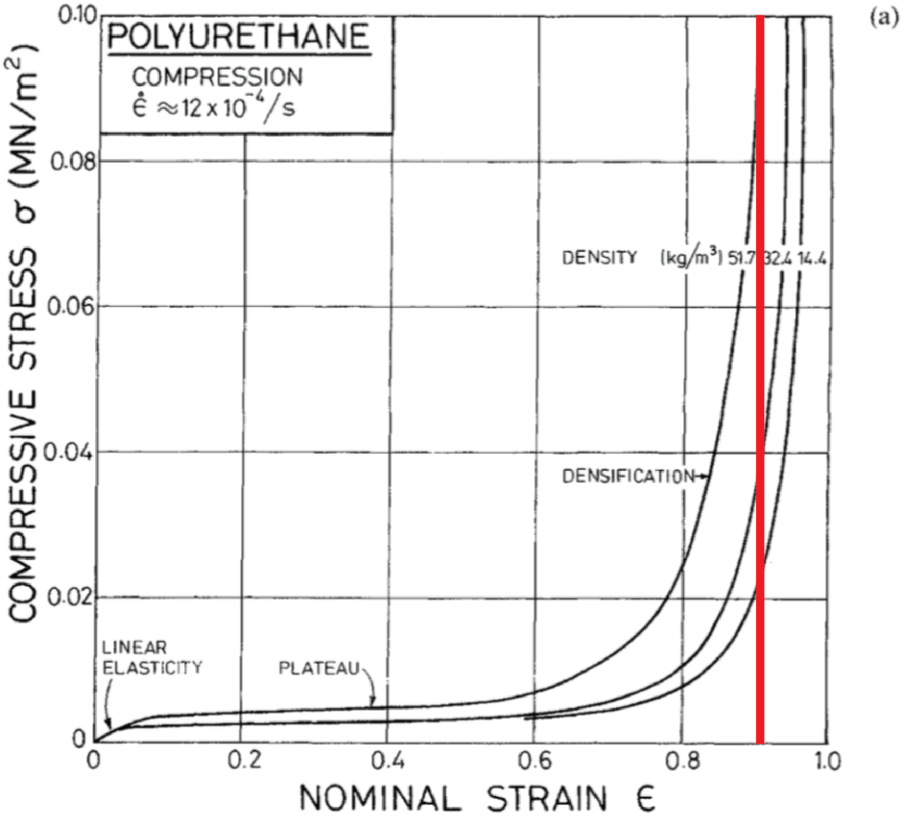

Figure 5.18: General plot of the stress strain relationships for polyurethane foams from Gibson [28], with the densification prediction overlaid in the red line.

Chapter 6

Summary & Future Work

In this work a computational model was developed for the use in modeling the large deformation and rapid compression of open-celled foam microstructures. The work used a non-linear beam network approximation to the foam geometry and the responses of the foam microstructure. The goal of the work was to present a micro-structural framework that could guide the design of foams for protection at high rates of compression.

This work builds on the work done to determine linear elastic material parameters for foam microstructures and the dynamic compression of metal foams. With this work dynamic compression testes were performed on foam microstructures at rates greater than reported in other tests. In order to accomplish these rates of compression, this work overcame the challenges of dealing with overloading of buckling ligaments, by inducing imperfections in the alignments of foam ligaments.

In the numerical rapid compression tests, the changes in shock speed of a simulated microstructure due to different impact speeds we obtained. Using these observations and the rigid-perfectly-plastic-locking(RPPL) macro-scale material model, a locking strain was able to be obtained for the foam microstructures. The locking strain predicted from the tests aligns with the locking strains from macro-scale models, providing evidence that this model can be used to help design foam microstructures.

6.1 Future Work

Thermo-Mechancial

The ZAP liners used in combat helmets are polyurethane based, other pads used in head protection are often polymers. Polymers materials are arrangements of long chains of repeated chemical patterns. These chains are either chemically bonded to each other and/or physically entangled with each other. Polymers can be very sensitive to changes in temperature, especially around a polymers glass transition temperature(T_g). The glass transition temperature is the temperature where the internal kinetic energy of the chains exceed a local

configurational energy barrier and the polymers gain a much greater degree of flexibility. As a polymer goes from below to above its T_g there is a rapid decrease in the elastic stiffness of the material as well as momentary rise in the viscous behavior of the material peaking at the T_g [22]. While many polymers have their T_g, below room temperature blends of polymers can have multiple transition temperatures where there is this reduction in elastic constants and a momentary spike in viscosity.

Micro-scale models taking into considerations generation of thermal energy within the structure as the foam deforms could be used to study how implanting a transition temperature in the relevant range of temperatures may be able to take advantage in this elastic softening and dramatic rise in viscous behavior. Thus possibly allowing for the design of foams where early in the impact event the foam is very stiff, to absorb as much energy as possible, but then at the end of the event the foam is softer, leading to less transmission of stress to the objects protected by the foam.

To implement the changes that occur around the glass transition temperature for a polymer the conservation of energy must be introduced:

$$\int_\Omega \rho\psi dv = \int_\Omega \rho c\tau dv = \int_\Omega \rho z dv - \int_{\partial\Omega} \vec{q}\cdot\vec{n} da + \int_\Omega \mathbb{D} dv \tag{6.1}$$

where ψ is the internal energy per unit mass,τ is the temperature at a point in the body, c is the heat capacity of the material , z is body sources/sinks of energy, $\vec{q}$ is the thermal heat flux, and $\mathbb{D}$ is the mechanical energy dissipated.

By capturing the dissipation of mechanical energy in the microstructure, a change in the temperature in the ligaments could be found and then using models like the Williams-Landel-Ferry(WLF) equation changes in the the viscosity and stiffness of the material can be found and used to update the parameters in the model.

Fluid Modeling

In the model used in this work the effects of the air surrounding the microstructure was ignored. However at high rates of compression there likely will be effects of the rapid compression because the speed of sound in dry air is around $350_{m/s}$[85]. There may be fluid compression and flow of the fluid through the porous foam. These effects can add it the heating of the foam structures and effect the mechanical response of the foams (section 6.1) and provided additional resistance to the impactor.

To implement the fluid model along with the solid model would require adding in an additional domain to the model. Currently, the model only observes changes in the solid body of the foam microstructure. The model does represent any of the empty space between the foam ligaments explicitly. Modeling the fluid would require explicitly modeling the 'void' space in between the ligaments. With the thermo-mechanics of the fluid modeled in this region and appropriate interactions prescribed between the deforming beam structure and the flowing/compressing fluid. To the author's knowledge a fluid-solid model for the rapid compression of foams has not been done. The author is aware of the use of creeping fluid

flows to include the effects of fluid flow with in macro-scale models of foams, and simulations to model fluid flow in cellular structures without deformation of the structure.

Models to capture the fluid behavior in the deforming structure could include:

- Directly modeling the fluid and solid domain together. Deformation of the solid structure will lead to a change in the shape of the fluid domain. This approach many most directly capture the behaviors, it will be expensive to preform.
- Separating the fluid and solid models. In this approach the solid model will be solved in a similar fashion as it is now, but with additional forcing terms obtained from the fluid model. The fluid model will be solved independently but with forcing and boundary conditions supplied to it from the current state of the solid model. This approach will likely be easier to implement, and be less expensive to run, however ensuring that the interactions between the solid and fluid models appropriately capture the correct behavior will be more difficult.

Parallelization

Currently, the model is implemented using PETSc but is limited to running in serial. The transition to parallel would allow for the use of additional computing cores, thus speeding up the computation time required to run the experiments. With faster computation times, larger models could be run. Transition from serial to parallel is not trivial however, while PETSc can manage most of the parallelization of the foam collapse problem, the contact between elements poses a problem. Contact potentially couples all elements' behavior to one another, while when PETSc distributes the problem, it silos information within each processor making it more difficult for an element on one processor to access information on an element on an other processor. Techniques exist to work around this siloing problem, however implementation in code muse be done carefully, or otherwise the code may spend a large amount of time communicating information between processors, greatly slowing down the code.

Bibliography

[1] William Wyatt Anderson. *Introduction to Shock Waves and Shock Wave Research*. 2017. DOI: 10.2172/1342845. URL: http://www.osti.gov/scitech/servlets/purl/1342845.

[2] Satish Balay et al. *PETSc Users Manual*. Tech. rep. ANL-95/11 - Revision 3.7. Argonne National Laboratory, 2016. URL: http://www.mcs.anl.gov/petsc.

[3] Satish Balay et al. *PETSc Web page*. http://www.mcs.anl.gov/petsc. 2016. URL: http://www.mcs.anl.gov/petsc.

[4] F.A. Bandak et al. "Chapter 6 - Injury biomechanics, neuropathology, and simplified physics of explosive blast and impact mild traumatic brain injury". In: *Traumatic Brain Injury, Part I*. Ed. by Jordan Grafman and Andres M. Salazar. Vol. 127. Handbook of Clinical Neurology. Elsevier, 2015, pp. 89 –104. DOI: http://dx.doi.org/10.1016/B978-0-444-52892-6.00006-4. URL: http://www.sciencedirect.com/science/article/pii/B9780444528926000064.

[5] Eyal Bar-Kochba et al. "Strain and rate-dependent neuronal injury in a 3D in vitro compression model of traumatic brain injury". In: *Scientific Reports* 6 (Aug. 2016), 30550 EP –. URL: http://dx.doi.org/10.1038/srep30550.

[6] C. Bradford Barber, David P. Dobkin, and Hannu Huhdanpaa. "The Quickhull Algorithm for Convex Hulls". In: *ACM Trans. Math. Softw.* 22.4 (Dec. 1996), pp. 469–483. ISSN: 0098-3500. DOI: 10.1145/235815.235821. URL: http://doi.acm.org/10.1145/235815.235821.

[7] A.T. Barnes et al. "Dynamic crushing of aluminum foams: Part I - Experiments". In: *International Journal of Solids and Structures* 51.9 (2014), pp. 1631 –1645. ISSN: 0020-7683. DOI: http://dx.doi.org/10.1016/j.ijsolstr.2013.11.019. URL: http://www.sciencedirect.com/science/article/pii/S0020768313004629.

[8] R.G.S. Barsoum. *Elastomeric Polymers with High Rate Sensitivity: Applications in Blast, Shockwave, and Penetration Mechanics*. Plastics Design Library. Elsevier Science, 2015. ISBN: 9780323354349. URL: https://books.google.com/books?id=V_ucBAAAQBAJ.

[9] Ted Belytschko, W.K. Liu, and B. Moran. *Nonlinear finite elements for continua and structures*. Wiley, 2000. ISBN: 9780471987734. URL: https://books.google.com/books?id=C6goAQAAMAAJ.

[10] M. Bernaschi, M. Lulli, and M. Sbragaglia. "GPU based detection of topological changes in Voronoi diagrams". In: *Computer Physics Communications* 213 (2017), pp. 19 –28. ISSN: 0010-4655. DOI: http://dx.doi.org/10.1016/j.cpc.2016.11.005. URL: http://www.sciencedirect.com/science/article/pii/S0010465516303599.

[11] E.G. Blackman. *Improving Traumatic Brain Injury Protection Measures and Standards for Helmets*. Defense Science Study Group Paper. University of Rochester, 2008.

[12] Martin Bock et al. "Generalized Voronoi Tessellation as a Model ofTwo-dimensional Cell Tissue Dynamics". In: *Bulletin of Mathematical Biology* 72.7 (2010), pp. 1696–1731. ISSN: 1522-9602. DOI: 10.1007/s11538-009-9498-3. URL: http://dx.doi.org/10.1007/s11538-009-9498-3.

[13] G. Bradski. "OpenCV". In: *Dr. Dobb's Journal of Software Tools* (2000).

[14] L Cannon. "Behind Armour Blunt Trauma - an emerging problem". In: *Journal of the Royal Army Medical Corps* 147.1 (2001), pp. 87–96. DOI: 10.1136/jramc-147-01-09. eprint: http://jramc.bmj.com/content/147/1/87.full.pdf+html. URL: http://jramc.bmj.com/content/147/1/87.abstract.

[15] P. Chadwick. *Continuum Mechanics: Concise Theory and Problems*. Dover books on physics. Dover Publications, 1999. ISBN: 9780486401805. URL: https://books.google.com/books?id=QSXIHQsus6UC.

[16] Howard R. Champion. "Abbreviated Injury Scale". In: *Encyclopedia of Intensive Care Medicine*. Ed. by Jean-Louis Vincent and Jesse B. Hall. Berlin, Heidelberg: Springer Berlin Heidelberg, 2012, pp. 1–5. ISBN: 978-3-642-00418-6. DOI: 10.1007/978-3-642-00418-6_355. URL: http://dx.doi.org/10.1007/978-3-642-00418-6_355.

[17] National Research Council. *Review of Department of Defense Test Protocols for Combat Helmets*. Washington, DC: The National Academies Press, 2014. ISBN: 978-0-309-29866-7. DOI: 10.17226/18621. URL: https://www.nap.edu/catalog/18621/review-of-department-of-defense-test-protocols-for-combat-helmets.

[18] L. Cui, M.A. Forero Rueda, and M.D. Gilchrist. "Optimization of energy absorbing liner for equestrian helmets. Part II: Functionally graded foam liner". In: *Materials and Design* 30.9 (2009), pp. 3414 –3419. ISSN: 0261-3069. DOI: http://dx.doi.org/10.1016/j.matdes.2009.03.044. URL: http://www.sciencedirect.com/science/article/pii/S0261306909001344.

[19] J. Demmel. *Applied Numerical Linear Algebra*. Society for Industrial and Applied Mathematics, 1997. DOI: 10.1137/1.9781611971446. eprint: http://epubs.siam.org/doi/pdf/10.1137/1.9781611971446. URL: http://epubs.siam.org/doi/abs/10.1137/1.9781611971446.

[20] H. Blackburn D.Niclasen. "A Comparison of Mass Lumping Techniques for the Two-Dimensional Navier-Stokes Equations". In: *Twelfth Australasian Fluid Mechanics Conference*. 1995.

[21] et al. ENRICO FERRI EMILIO ANTINUCCI. "DYNAMIC BUCKLING OF IMPULSIVELY LOADED PRISMATIC CORES". In: *JOURNAL OF MECHANICS OF MATERIALS AND STRUCTURES* 1.8 (2006), 1345?1365. DOI: 10.2140/jomms.2006.1.1345.

[22] J.D. Ferry. 2nd. Wiley and Sons, 1970.

[23] John Fitek. *Shock Tube Test for Energy Absorbing Materials*. Tech. rep. ARMY NATICK SOLDIER RESEARCH DEVELOPMENT and ENGINEERING CENTER MA, 2013.

[24] S. Gaitanaros and S. Kyriakides. "Dynamic crushing of aluminum foams: Part II - Analysis". In: *International Journal of Solids and Structures* 51.9 (2014), pp. 1646 – 1661. ISSN: 0020-7683. DOI: http://dx.doi.org/10.1016/j.ijsolstr.2013.11.020. URL: http://www.sciencedirect.com/science/article/pii/S0020768313004630.

[25] Stavros Gaitanaros and Stelios Kyriakides. "On the effect of relative density on the crushing and energy absorption of open-cell foams under impact". In: *International Journal of Impact Engineering* 82 (2015). Metallic Foams under Dynamic Loading, pp. 3 –13. ISSN: 0734-743X. DOI: https://doi.org/10.1016/j.ijimpeng.2015.03.011. URL: http://www.sciencedirect.com/science/article/pii/S0734743X15000536.

[26] Y.X. Gan, C. Chen, and Y.P. Shen. "Three-dimensional modeling of the mechanical property of linearly elastic open cell foams". In: *International Journal of Solids and Structures* 42.26 (2005), pp. 6628 –6642. ISSN: 0020-7683. DOI: http://dx.doi.org/10.1016/j.ijsolstr.2005.03.002. URL: http://www.sciencedirect.com/science/article/pii/S0020768305001137.

[27] A. Geißler and W. Schmitt. "Investigations of a Closed-Cell Foam with Scanning Electron Microscopy". In: *Third European Rheology Conference and Golden Jubilee Meeting of the British Society of Rheology*. Ed. by D. R. Oliver. Dordrecht: Springer Netherlands, 1990, pp. 555–557. ISBN: 978-94-009-0781-2. DOI: 10.1007/978-94-009-0781-2_189. URL: http://dx.doi.org/10.1007/978-94-009-0781-2_189.

[28] Lorna J. Gibson and Michael F. Ashby. *Cellular Solids: Structure and Properties*. 2nd ed. Cambridge Solid State Science Series. Cambridge University Press, 1997. ISBN: 9781139878326. DOI: 10.1017/CBO9781139878326. URL: https://www.cambridge.org/core/books/cellular-solids/BC25789552BAA8E3CAD5E1D105612AB5.

[29] J.H. Ginsberg. *Mechanical and Structural Vibrations: Theory and Applications*. Wiley, 2001. ISBN: 9780471370840. URL: https://books.google.com/books?id=xo9RAAAAMAAJ.

[30] S. Gogineni et al. "Ballistic Impact of Twaron CT709 Plain Weave Fabrics". In: *Mechanics of Advanced Materials and Structures* 19.6 (2012), pp. 441–452. DOI: 10.1080/15376494.2011.575532.

[31] L. Gong and S. Kyriakides. "Compressive response of open cell foams Part II: Initiation and evolution of crushing". In: *International Journal of Solids and Structures* 42.5 (2005), pp. 1381 –1399. ISSN: 0020-7683. DOI: http://dx.doi.org/10.1016/j.ijsolstr.2004.07.024. URL: http://www.sciencedirect.com/science/article/pii/S0020768304004317.

[32] L. Gong, S. Kyriakides, and W.-Y. Jang. "Compressive response of open-cell foams. Part I: Morphology and elastic properties". In: *International Journal of Solids and Structures* 42.5 (2005), pp. 1355 –1379. ISSN: 0020-7683. DOI: http://dx.doi.org/10.1016/j.ijsolstr.2004.07.023. URL: http://www.sciencedirect.com/science/article/pii/S0020768304004305.

[33] F.A. Govan et al. *Thermal Insulation, Materials, and Systems for Energy Conservation in the '80s: A Conference*. ASTM STP 789 no. 789. American Society for Testing and Materials, 1983. ISBN: 9780803102309. URL: https://books.google.com/books?id=p-vsLBXS0FAC.

[34] K.F. Graff. *Wave Motion in Elastic Solids*. Dover Books on Physics Series. Dover Publications, 1975. ISBN: 9780486667454. URL: https://books.google.com/books?id=5cZFRwLuhdQC.

[35] A.E. Green and P.M. Naghdi. "Non-isothermal theory of rods, plates and shells". In: *International Journal of Solids and Structures* 6.2 (1970), pp. 209 –244. ISSN: 0020-7683. DOI: http://dx.doi.org/10.1016/0020-7683(70)90021-1. URL: http://www.sciencedirect.com/science/article/pii/0020768370900211.

[36] L. Greengard and V. Rokhlin. "A Fast Algorithm for Particle Simulations". In: *J. Comput. Phys.* 73.2 (Dec. 1987), pp. 325–348. ISSN: 0021-9991. DOI: 10.1016/0021-9991(87)90140-9. URL: http://dx.doi.org/10.1016/0021-9991(87)90140-9.

[37] Peter Hansbo. "Aspects of conservation in finite element flow computations". In: *Computer Methods in Applied Mechanics and Engineering* 117.3 (1994), pp. 423 –437. ISSN: 0045-7825. DOI: http://dx.doi.org/10.1016/0045-7825(94)90127-9. URL: http://www.sciencedirect.com/science/article/pii/0045782594901279.

[38] Mariusz Ziejewski and Ghodrat Karami Hesam Sarvghad-Moghaddam Asghar Rezaei. "CFD modeling of the underwash effect of military helmets as a possible mechanism for blast-induced traumatic brain injury". In: *Computer Methods in Biomechanics and Biomedical Engineering* 20.1 (2017). PMID: 27269066, pp. 16–26. DOI: 10.1080/10255842.2016.1193597. eprint: http://dx.doi.org/10.1080/10255842.2016.1193597. URL: http://dx.doi.org/10.1080/10255842.2016.1193597.

[39] Hadi S. Hosseini, Ghislain Maquer, and Philippe K. Zysset. "micro CT-based trabecular anisotropy can be reproducibly computed from HR-pQCT scans using the triangulated bone surface". In: *Bone* 97 (2017), pp. 114 –120. ISSN: 8756-3282. DOI: http://dx.doi.org/10.1016/j.bone.2017.01.016. URL: http://www.sciencedirect.com/science/article/pii/S8756328217300169.

[40] John Hutchinson, Mark J. Kaiser, and Hamid M. Lankarani. "The Head Injury Criterion (HIC) functional". In: *Applied Mathematics and Computation* 96.1 (1998), pp. 1 –16. ISSN: 0096-3003. DOI: http://dx.doi.org/10.1016/S0096-3003(97)10106-0. URL: http://www.sciencedirect.com/science/article/pii/S0096300397101060.

[41] Oana M. Istrateab and Biqiong Chen. "Relative modulus relative density relationships in low density polymer clay nanocomposite foams". In: *Soft Matter* 7 (2011), p. 1840.

[42] Wen-Yea Jang, Stelios Kyriakides, and Andrew M. Kraynik. "On the compressive strength of open-cell metal foams with Kelvin and random cell structures". In: *International Journal of Solids and Structures* 47.21 (2010), pp. 2872 –2883. ISSN: 0020-7683. DOI: http://dx.doi.org/10.1016/j.ijsolstr.2010.06.014. URL: http://www.sciencedirect.com/science/article/pii/S0020768310002271.

[43] E.Meyer J.Fitek. *DESIGN OF A HELMET LINER FOR IMPROVED LOW VELOCITY IMPACT PROTECTION*. TECHNICAL REPORT. U.S. Army Natick Soldier Research, Development and Engineering Center, 2013.

[44] Mike Kamermans. *Gaussian Quadrature Weights and Abscissae*. [Online; accessed 2017-03-27]. 2011. URL: \url{https://pomax.github.io/bezierinfo/legendre-gauss.html}.

[45] Alireza Karimi et al. "Dynamic finite element simulation of the gunshot injury to the human forehead protected by polyvinyl alcohol sponge". In: *Journal of Materials Science: Materials in Medicine* 27.4 (2016), p. 74. ISSN: 1573-4838. DOI: 10.1007/s10856-016-5686-5. URL: https://doi.org/10.1007/s10856-016-5686-5.

[46] E. Kreyszig. *Differential Geometry*. Differential Geometry. University of Toronto Press, 1959. ISBN: 9780486667218. URL: https://books.google.com/books?id=P73DrhE9F0QC.

[47] S.G. Kulkarni et al. "Ballistic helmets Their design, materials, and performance against traumatic brain injury". In: *Composite Structures* 101 (2013), pp. 313 –331. ISSN: 0263-8223. DOI: http://dx.doi.org/10.1016/j.compstruct.2013.02.014. URL: http://www.sciencedirect.com/science/article/pii/S0263822313000950.

[48] B.J. Lazan. *Damping of Materials and Members in Structural Mechanics*. Pergamon, 1968. URL: https://books.google.com/books?id=5sV0nQEACAAJ.

[49] R.J. LeVeque. *Finite Difference Methods for Ordinary and Partial Differential Equations: Steady-State and Time-Dependent Problems*. Society for Industrial and Applied Mathematics, 2007. ISBN: 9780898716290. URL: https://books.google.com/books?id=qsvmsXe8Ug4C.

[50] X.G. Li, X.-L. Gao, and S. Kleiven. "Behind helmet blunt trauma induced by ballistic impact: A computational model". In: *International Journal of Impact Engineering* 91 (2016), pp. 56 –67. ISSN: 0734-743X. DOI: http://dx.doi.org/10.1016/j.ijimpeng.2015.12.010. URL: http://www.sciencedirect.com/science/article/pii/S0734743X15300282.

[51] Minzu Liang et al. "Theoretical and numerical investigation of blast responses of continuous-density graded cellular materials". In: *Composite Structures* 164 (2017), pp. 170 –179. ISSN: 0263-8223. DOI: https://doi.org/10.1016/j.compstruct.2016.12.065. URL: http://www.sciencedirect.com/science/article/pii/S0263822316307516.

[52] P. Litewka. *Finite Element Analysis of Beam-to-Beam Contact*. Springer-Verlag Berlin Heidelberg, 2010. ISBN: 978-3-642-12940-7.

[53] Qunli Liu and Ghatu Subhash. "A phenomenological constitutive model for foams under large deformations". In: *Polymer Engineering and Science* 44.3 (2004), pp. 463–473. ISSN: 1548-2634. DOI: 10.1002/pen.20041. URL: http://dx.doi.org/10.1002/pen.20041.

[54] Murray Mackay. "The increasing importance of the biomechanics of impact trauma". In: *Sadhana* 32.4 (2007), pp. 397–408. ISSN: 0973-7677. DOI: 10.1007/s12046-007-0031-9. URL: http://dx.doi.org/10.1007/s12046-007-0031-9.

[55] Phillip McEntire B. J. ; Whitley. *Blunt Impact Performance Characteristics of the Advanced Combat Helmet and the Paratrooper and Infantry Personnel Armor System for Ground Troops Helmet*. TECHNICAL REPORT. ARMY AEROMEDICAL RESEARCH LAB FORT RUCKER AL, 2005.

[56] Melissa J. McGinn and John T. Povlishock. "Chapter 5 - Cellular and molecular mechanisms of injury and spontaneous recovery". In: *Traumatic Brain Injury, Part I*. Ed. by Jordan Grafman and Andres M. Salazar. Vol. 127. Handbook of Clinical Neurology. Elsevier, 2015, pp. 67 –87. DOI: http://dx.doi.org/10.1016/B978-0-444-52892-6.00005-2. URL: http://www.sciencedirect.com/science/article/pii/B9780444528926000052.

[57] Donald Meagher. "Geometric modeling using octree encoding". In: *Computer Graphics and Image Processing* 19.2 (1982), pp. 129 –147. ISSN: 0146-664X. DOI: http://dx.doi.org/10.1016/0146-664X(82)90104-6. URL: http://www.sciencedirect.com/science/article/pii/0146664X82901046.

[58] David F. Meaney and Douglas H. Smith. "Chapter 7 - Cellular biomechanics of central nervous system injury". In: *Traumatic Brain Injury, Part I*. Ed. by Jordan Grafman and Andres M. Salazar. Vol. 127. Handbook of Clinical Neurology. Elsevier, 2015, pp. 105 –114. DOI: http://dx.doi.org/10.1016/B978-0-444-52892-6.00007-6. URL: http://www.sciencedirect.com/science/article/pii/B9780444528926000076.

[59] N.J. Mills. "The high strain mechanical response of the wet Kelvin model for open-cell foams". In: *International Journal of Solids and Structures* 44.1 (2007), pp. 51 –65. ISSN: 0020-7683. DOI: http://dx.doi.org/10.1016/j.ijsolstr.2006.04.014. URL: http://www.sciencedirect.com/science/article/pii/S0020768306001235.

[60] William C. Moss and Michael J. King. *Impact response of US Army and National Football League helmet pad systems*. Tech. rep. Lawrence Livermore National Laboratory, 2011.

[61] N.K. Naik and P. Shrirao. "Composite structures under ballistic impact". In: *Composite Structures* 66.14 (2004). Twelfth International Conference on Composite Structures, pp. 579 –590. ISSN: 0263-8223. DOI: http://dx.doi.org/10.1016/j.compstruct.2004.05.006. URL: http://www.sciencedirect.com/science/article/pii/S0263822304001825.

[62] V.-D. Nguyen and L. Noels. "Computational homogenization of cellular materials". In: *International Journal of Solids and Structures* 51.11 (2014), pp. 2183 –2203. ISSN: 0020-7683. DOI: http://dx.doi.org/10.1016/j.ijsolstr.2014.02.029. URL: http://www.sciencedirect.com/science/article/pii/S0020768314000778.

[63] O.M. O'Reilly. *Modeling Nonlinear Problems in the Mechanics of Strings and Rods: The Role of the Balance Laws*. Interaction of Mechanics and Mathematics. Springer International Publishing, 2017. ISBN: 9783319505985. URL: https://books.google.com/books?id=yDxRDgAAQBAJ.

[64] O.M. O'Reilly. "On constitutive relations for elastic rods". In: *International Journal of Solids and Structures* 35.11 (1998), pp. 1009 –1024. ISSN: 0020-7683. DOI: http://dx.doi.org/10.1016/S0020-7683(97)00100-5. URL: //www.sciencedirect.com/science/article/pii/S0020768397001005.

[65] Kofi Osei-Bonsu, Paul Grassia, and Nima Shokri. "Investigation of foam flow in a 3D printed porous medium in the presence of oil". In: *Journal of Colloid and Interface Science* 490 (2017), pp. 850 –858. ISSN: 0021-9797. DOI: https://doi.org/10.1016/j.jcis.2016.12.015. URL: http://www.sciencedirect.com/science/article/pii/S0021979716310086.

[66] Bhavesh Patel and Tarek I. Zohdi. "Numerical estimation of effective electromagnetic properties for design of particulate composites". In: *Materials and Design* 94 (2016), pp. 546 –553. ISSN: 0264-1275. DOI: http://dx.doi.org/10.1016/j.matdes.2016.01.015. URL: http://www.sciencedirect.com/science/article/pii/S0264127516300156.

[67] Alejandro Francisco Queiruga. "Microscale Simulation of the Mechanical and Electromagnetic Properties of Textiles". PhD thesis. University of California, Berkeley, 2015.

[68] Mayank Singh Rajput, Manish Kumar Bhuarya, and Arpan Gupta. "Finite Element Simulation of Impact on PASGT Army Helmet". In: *Procedia Engineering* 173 (2017). Plasticity and Impact Mechanics, pp. 251 –258. ISSN: 1877-7058. DOI: http://dx.doi.org/10.1016/j.proeng.2016.12.007. URL: http://www.sciencedirect.com/science/article/pii/S1877705816343983.

[69] S.R. Reid and C. Peng. "Dynamic uniaxial crushing of wood". In: *International Journal of Impact Engineering* 19.5 (1997), pp. 531 –570. ISSN: 0734-743X. DOI: http://dx.doi.org/10.1016/S0734-743X(97)00016-X. URL: http://www.sciencedirect.com/science/article/pii/S0734743X9700016X.

[70] M. Rodrguez-Milln et al. "Effect of full helmet systems on human head responses under blast loading". In: *Materials and Design* 117 (2017), pp. 58 –71. ISSN: 0264-1275. DOI: http://dx.doi.org/10.1016/j.matdes.2016.12.081. URL: http://www.sciencedirect.com/science/article/pii/S0264127516316070.

[71] D Ruan et al. "In-plane dynamic crushing of honeycomb's a finite element study". In: *International Journal of Impact Engineering* 28.2 (2003), pp. 161 –182. ISSN: 0734-743X. DOI: http://dx.doi.org/10.1016/S0734-743X(02)00056-8. URL: http://www.sciencedirect.com/science/article/pii/S0734743X02000568.

[72] M. B. Rubin. "Restrictions on nonlinear constitutive equations for elastic rods". In: *Journal of Elasticity* 44.1 (1996), pp. 9–36. ISSN: 1573-2681. DOI: 10.1007/BF00042190. URL: http://dx.doi.org/10.1007/BF00042190.

[73] M.B. Rubin. *Cosserat Theories: Shells, Rods and Points*. Dordrecht, The Netherlands: Kluwer Academic Publishers, 2000.

[74] M.B. Rubin. *Cosserat Theories: Shells, Rods and Points*. Solid Mechanics and Its Applications. Springer Netherlands, 2013. ISBN: 9789401593793. URL: https://books.google.com/books?id=kMHxCAAAQBAJ.

[75] M.A. Forero Rueda, L. Cui, and M.D. Gilchrist. "Optimization of energy absorbing liner for equestrian helmets. Part I: Layered foam liner". In: *Materials and Design* 30.9 (2009), pp. 3405 –3413. ISSN: 0261-3069. DOI: http://dx.doi.org/10.1016/j.matdes.2009.03.037. URL: http://www.sciencedirect.com/science/article/pii/S0261306909001356.

[76] J.W. Hutchinson H.D. Espinosa S. Lee F. Barthelat. "Dynamic failure of metallic pyramidal truss core materials ? Experiments and modeling". In: *International Journal of Plasticity* 22.1 (2006), pp. 2118 –2145. ISSN: 0749-6419. DOI: 10.1016/j.ijplas.2006.02.006.

[77] F. SCARPA and G. TOMLINSON. "THEORETICAL CHARACTERISTICS OF THE VIBRATION OF SANDWICH PLATES WITH IN-PLANE NEGATIVE POISSON'S RATIO VALUES". In: *Journal of Sound and Vibration* 230.1 (2000), pp. 45 –67. ISSN: 0022-460X. DOI: http://dx.doi.org/10.1006/jsvi.1999.2600. URL: http://www.sciencedirect.com/science/article/pii/S0022460X99926007.

[78] Yoshikatsu Shinoda and Akihiro Matsuda. "Homogenization Analysis of Porous Polymer Considering Microscopic Structure". In: *Procedia Engineering* 60 (2013). 6th Asia-Pacific Congress on Sports Technology (APCST), pp. 343 –348. ISSN: 1877-7058. DOI: http://dx.doi.org/10.1016/j.proeng.2013.07.027. URL: http://www.sciencedirect.com/science/article/pii/S1877705813010783.

[79] Daniela M. Ushizima, Andrea G. C. Bianchi, and Claudia M. Carneiro. "Segmentation of subcellular compartments combining superpixel representation with Voronoi diagrams". In: 2015. URL: http://www.osti.gov/scitech/servlets/purl/1167389.

[80] E. Verhulp et al. "Micro-finite element simulation of trabecular-bone post-yield behaviour effects of material model, element size and type". In: *Computer Methods in Biomechanics and Biomedical Engineering* 11.4 (2008). PMID: 18568833, pp. 389–395. DOI: 10.1080/10255840701848756. eprint: http://dx.doi.org/10.1080/10255840701848756. URL: http://dx.doi.org/10.1080/10255840701848756.

[81] John Versace. "A Review of the Severity Index". In: *SAE Technical Paper*. SAE International, Feb. 1971. DOI: 10.4271/710881. URL: http://dx.doi.org/10.4271/710881.

[82] Andrea Vigliotti and Damiano Pasini. "Stiffness and strength of tridimensional periodic lattices". In: *Computer Methods in Applied Mechanics and Engineering* 229 (2012), pp. 27 –43. ISSN: 0045-7825. DOI: http://dx.doi.org/10.1016/j.cma.2012.03.018. URL: http://www.sciencedirect.com/science/article/pii/S0045782512000941.

[83] J.C. Wallach and L.J. Gibson. "Mechanical behavior of a three-dimensional truss material". In: *International Journal of Solids and Structures* 38.40 (2001), pp. 7181 –7196. ISSN: 0020-7683. DOI: http://dx.doi.org/10.1016/S0020-7683(00)00400-5. URL: http://www.sciencedirect.com/science/article/pii/S0020768300004005.

[84] J. R. Williams and R. O'Connor. "Discrete element simulation and the contact problem". In: *Archives of Computational Methods in Engineering* 6.4 (1999), pp. 279–304. ISSN: 1886-1784. DOI: 10.1007/BF02818917. URL: http://dx.doi.org/10.1007/BF02818917.

[85] George S. K. Wong. "Speed of sound in standard air". In: *The Journal of the Acoustical Society of America* 79.5 (1986), pp. 1359–1366. DOI: 10.1121/1.393664. eprint: http://dx.doi.org/10.1121/1.393664. URL: http://dx.doi.org/10.1121/1.393664.

[86] P. Wriggers. "Finite element algorithms for contact problems". In: *Archives of Computational Methods in Engineering* 2.4 (1995), pp. 1–49. ISSN: 1886-1784. DOI: 10.1007/BF02736195. URL: http://dx.doi.org/10.1007/BF02736195.

[87] P. Wriggers, T. Vu Van, and E. Stein. "Finite element formulation of large deformation impact-contact problems with friction". In: *Computers and Structures* 37.3 (1990), pp. 319 –331. ISSN: 0045-7949. DOI: http://dx.doi.org/10.1016/0045-7949(90)90324-U. URL: http://www.sciencedirect.com/science/article/pii/004579499090324U.

[88] Liying Zhang, Rahul Makwana, and Sumit Sharma. "Brain Response to Primary Blast Wave Using Validated Finite Element Models of Human Head and Advanced Combat Helmet". In: *Frontiers in Neurology* 4 (2013), p. 88. DOI: 10.3389/fneur.2013.00088. URL: http://www.ncbi.nlm.nih.gov/pmc/articles/PMC3731672/.

[89] Timothy Zhang and Sikhanda Satapathy. *Effect of Helmet Pads on the Load Transfer to Head under Blast Loadings*. Tech. rep. ARL, June 2015.

[90] Yan Zhao and Zheng-Guo Wang. "Blast-induced traumatic brain injury: a new trend of blast injury research". In: *Chinese Journal of Traumatology* 18.4 (2015), pp. 201 –203. ISSN: 1008-1275. DOI: http://dx.doi.org/10.1016/j.cjtee.2015.10.002. URL: http://www.sciencedirect.com/science/article/pii/S1008127515000954.

[91] Zhijun Zheng, Jilin Yu, and Jianrong Li. "Dynamic crushing of 2D cellular structures: A finite element study". In: *International Journal of Impact Engineering* 32.14 (2005). Fifth International Symposium on Impact Engineering, pp. 650 –664. ISSN: 0734-743X. DOI: https://doi.org/10.1016/j.ijimpeng.2005.05.007. URL: http://www.sciencedirect.com/science/article/pii/S0734743X05000795.

[92] Zhijun Zheng et al. "Dynamic crushing of cellular materials: A unified framework of plastic shock wave models". In: *International Journal of Impact Engineering* 53 (2013). Special issue based on contributions at the 3rd International Conference on Impact Loading of Lightweight Structures, pp. 29 –43. ISSN: 0734-743X. DOI: http://dx.doi.org/10.1016/j.ijimpeng.2012.06.012. URL: http://www.sciencedirect.com/science/article/pii/S0734743X12001674.

[93] H.X. Zhu, N.J. Mills, and J.F. Knott. "Analysis of the high strain compression of open-cell foams". In: *Journal of the Mechanics and Physics of Solids* 45.11 (1997), pp. 1875 – 1904. ISSN: 0022-5096. DOI: http://dx.doi.org/10.1016/S0022-5096(97)00027-6. URL: http://www.sciencedirect.com/science/article/pii/S0022509697000276.

[94] O.C. Zienkiewicz, R.L. Taylor, and J.Z. Zhu. *The Finite Element Method: Its Basis and Fundamentals*. Elsevier Science, 2005. ISBN: 9780080472775. URL: https://books.google.com/books?id=YocoaH8lnx8C.

[95] T.I. Zohdi. *A Finite Element Primer for Beginners: The Basics*. SpringerBriefs in Applied Sciences and Technology. Springer International Publishing, 2014. ISBN: 9783319090368. URL: https://books.google.com/books?id=XfhEBAAAQBAJ.

[96] *ZORBIUM ACTION PAD (ZAP?) 7-PAD NSN SYSTEM Product Page*. 2017. URL: https://www.teamwendy.com/products/aftermarket-systems/liner-systems/zap-zorbium-action-pad-systems/zorbium-action-pad-zap-7-pad-nsn-system.

Appendix A

Non-Rigid Angle Evidence

Between two vectors there is an angle cosine that can be defined by:

$$\vec{a} \cdot \vec{b} = |\vec{a}||\vec{b}| \cos(\theta_0) \tag{A.1}$$

if a vector is added on to both $\vec{a}$ and $\vec{b}$ equation A.1 becomes:

$$(\vec{a} + \vec{\delta}) \cdot (\vec{b} + \vec{\delta}) = |(\vec{a} + \vec{\delta})||(\vec{b} + \vec{\delta})| \cos(\theta_1) \tag{A.2}$$

If the angle between the vectors $\vec{a}$ and $\vec{b}$ does not change after the addition of vector $\vec{\delta}$ then the cosines should not change. Thus one would assume that $\cos(\theta_1) - \cos(\theta_0) = 0$, if this is not true then the two angles can not be equal. Several random sets of vectors $\vec{a}, \vec{b}$,and $\vec{\delta}$ were generated and tested. The results of the differences in their cosines are plotted in figure A.1, as can be observed the differences in the cosines are far from zero, thus the two statements A.1 and A.2 can not be equal.

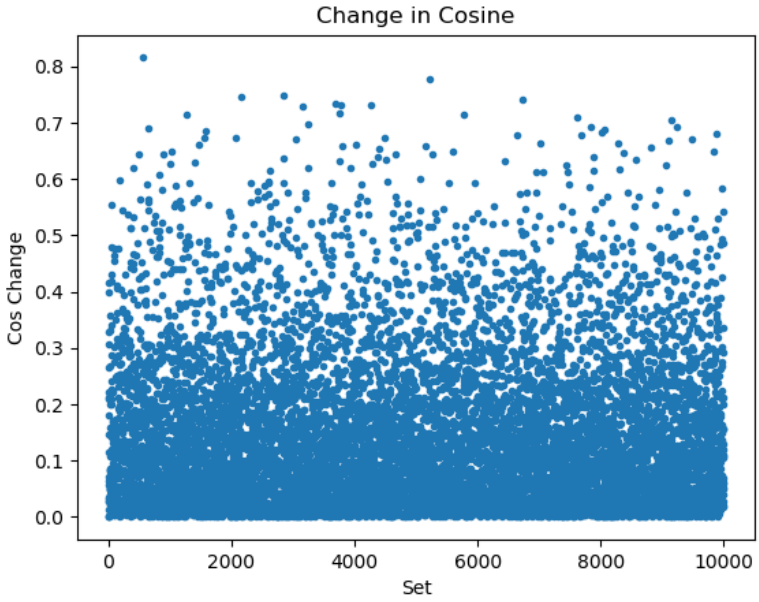

Figure A.1: Plot of the difference in cosines before and after the addition of a vector to a set pair of vectors.

Appendix B

Spacing For Contact Detection

In order for the discrete contact detection to achieve acceptable contact performance, the distances separating the gauss points and the nodal points must be under some limit as a function of the ligament radius. To get an approximation to this limit the following assumptions are used:

1. The ligaments are approximated as straight cylinders, with equal radii.
2. The ligaments are of equal length, and have the same number of elements.
3. The elements are the same size.
4. The most risk prone configuration for failure of contact detection is the orthogonal crossing of ligaments.

Initial variables for this problem are as follows:

- R: The radius of the ligamens
- d: The largest distance between gauss points, and or a gauss point and a node
- L: Length of a ligament
- N: Number of elements per ligament
- h: The actual minimum distance between ligaments
- g: The gap function as measured

With the assumptions, the arrangement of ligaments that will cause the worst contact performance is if their contact point would lie in the middle of the largest distance between the detection points Thus out gap function becomes:

$$g = \sqrt{\left(\frac{d}{2}\right)^2 + \left(\frac{d}{2}\right)^2 + h^2} - 2R = \sqrt{\frac{d^2}{2} + h^2} - 2R \tag{B.1}$$

When $g \leq 0$ then there is contact, thus if $d = 0$ then contact would occur when $h = 2R$ as it would be expected. But when d is nonzero this causes contact detection at $h < 2R$, and if d is so large then it is possible that the gap function never reaches zero. Thus, let $h = \alpha 2R$, where α is the fraction that is determined to be an acceptable loss of detection $(0 < \alpha \leq 1)$. Thus setting equation B.1 to zero and substituting:

$$0 = \sqrt{\frac{d^2}{2} + 4\alpha^2 R^2} - 2R \qquad 4R^2 = \frac{d^2}{2} + 4\alpha^2 R^2 \tag{B.2}$$

d is related to the length of the ligament by:

$$d = \gamma \frac{L}{N} \tag{B.3}$$

Where γ is the fraction of the element length that separates the detection points.

$$4R^2 = \frac{1}{2}\gamma^2 \frac{L^2}{N^2} + 4\alpha^2 R^2 \tag{B.4}$$

$$2 = \left(\frac{\gamma}{2N}\right)^2 \left(\frac{L}{R}\right)^2 + 2\alpha^2 \tag{B.5}$$

Letting $a = \frac{L}{R}$ such that the 'fixed' pars of the problem are simplified out to an aspect ratio. The relation among all of our design variables exist:

$$2 = a^2 \left(\frac{\gamma}{2N}\right)^2 + 2\alpha^2 \tag{B.6}$$

For a three point gauss scheme the largest gap size is $\gamma_3 \approx .387$ and for a four point scheme we have $\gamma_4 \approx .261$ [44]. Now the number of elements required to achieve a desired level of contact fidelity can be written:

$$N_i = \frac{1}{2}\sqrt{\frac{a^2}{2}\gamma_i^2 + \alpha^2} \tag{B.7}$$

When the aspect ratio is large enough, the error term becomes insignifigant and equation B.7 becomes:

$$N_i = \frac{a}{2\sqrt{2}}\gamma_i \tag{B.8}$$

Appendix C

Shock Front Plots

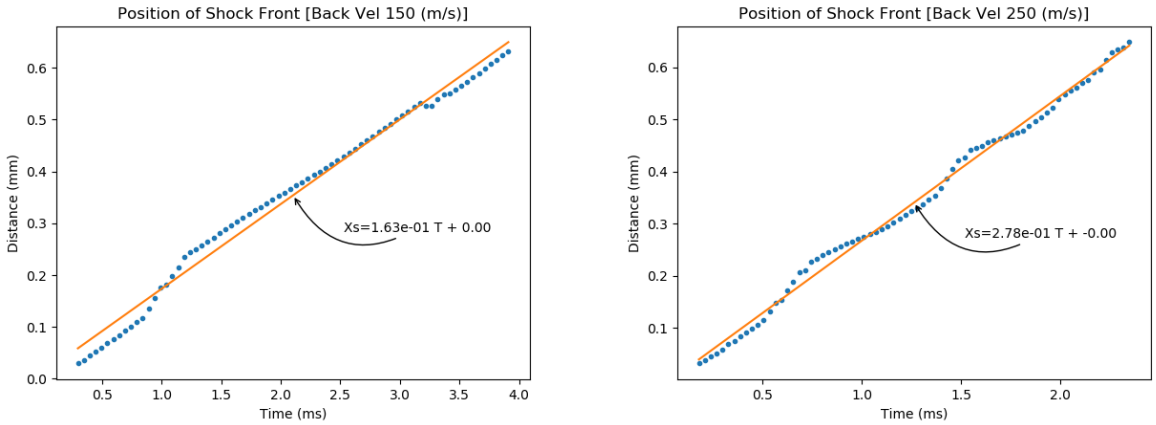

Figure C.1: Shock Front position over time and linear approximation to position of shock front for regular patterned geometry with a relative density of .02 at impact speeds of $150^{m}/_{s}$ and $250^{m}/_{s}$

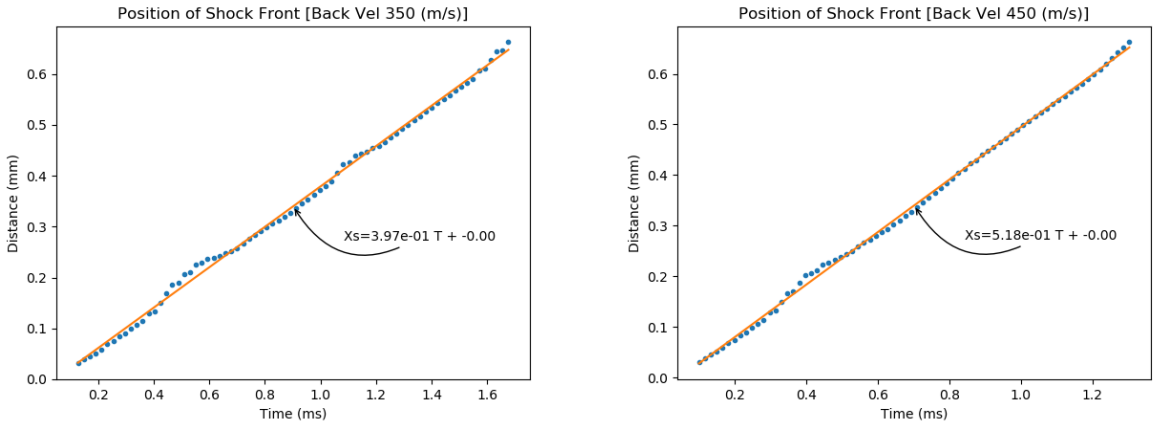

Figure C.2: Shock Front position over time and linear approximation to position of shock front for regular patterned geometry with a relative density of .02 at impact speeds of $350^{m}/_{s}$ and $450^{m}/_{s}$

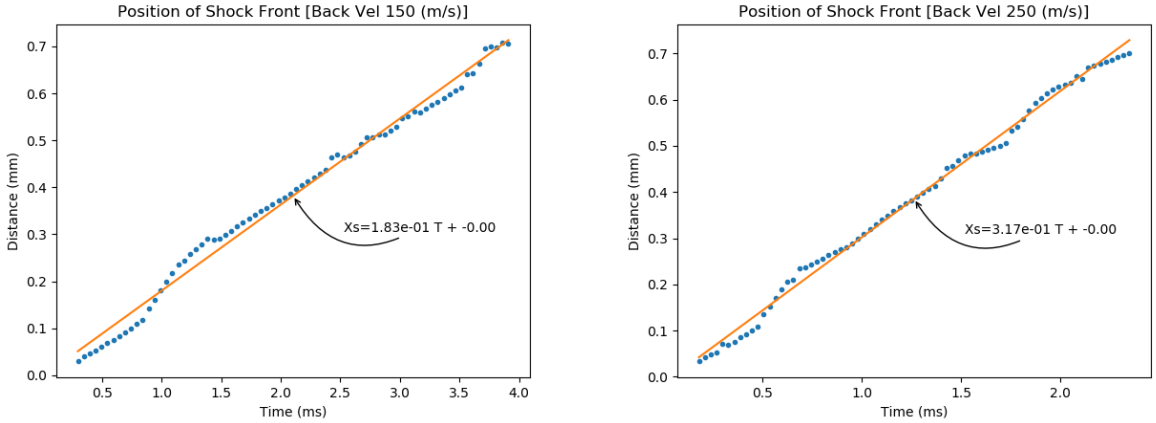

Figure C.3: Shock Front position over time and linear approximation to position of shock front for regular patterned geometry with a relative density of .10 at impact speeds of $150^{m}/_{s}$ and $250^{m}/_{s}$

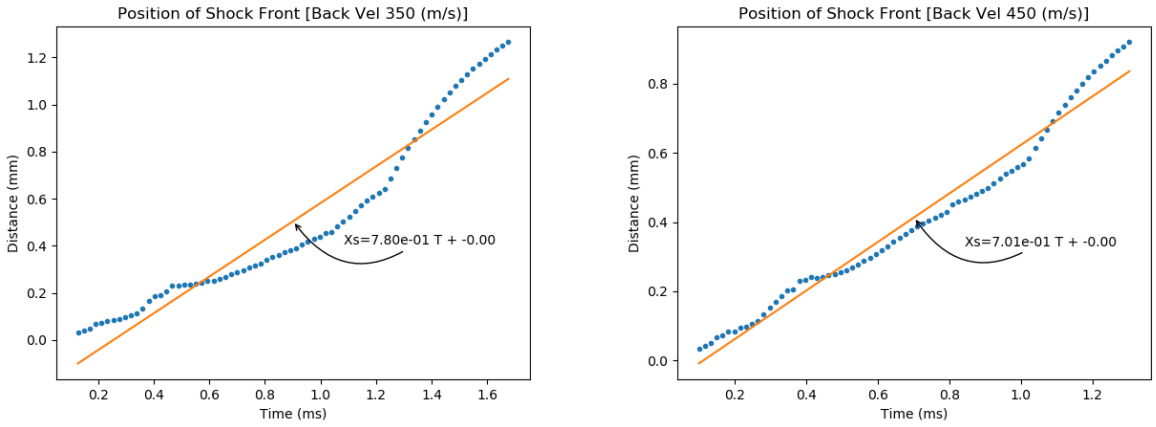

Figure C.4: Shock Front position over time and linear approximation to position of shock front for regular patterned geometry with a relative density of .10 at impact speeds of $350^{m}/_{s}$ and $450^{m}/_{s}$